UNIVERSITY OF COPENHAGEN

Master of Science - Nanoscience

Improving Segmentation for Medical Tomography with Spatially Adapted Probability Distributions

Mads Alexander Pedersen

JNC582@alumni.ku.dk

Supervisor: James Emil Avery

Co-Supervisor: Aleksandar Topic

2. October 2020

ACKNOWLEDGEMENTS

I would personally like to thanks my supervisor James Emil Avery for giving me the opportunity to be involved in such an interesting project. You are always full of ideas what to do next.

A personal thanks to my co-supervisor Aleksandar Topic for always being available to help, discuss, evaluate and analyse all the crazy results i would have never made it without your assistance.

Thanks to the group of e-science for having me in and permitting access to office space and super computer My gratitude goes to Carl for helping with to use the super computer

Many thanks to Else Pinholt for providing The Computer Tomographies, the project would never have existed with out you.

Many thanks to Buster and Simon for mental support in the final weeks before deadline.

High praises for Troels Ynddal, Villads Roskjær and Henrik Pinholt for taking time out of their schedule to help and discuss matters of my thesis.

Huge gratitude to Jacob, Freja and Josephine, without your support in the beginning of university, i would have never come this far.

A personal thanks to Sina Borgi. Through many stressful times we supported each other and made it through to the end, together.

Love to my family and girlfriend Clara for the support during university and especially during the thesis.

Endless praise to the close friends from nanoscience Jacob, Henrik, Lasse, Villads, Søren, Rasmus, Adam, Nikolaj, Putte, Mikkel H, Sina and Tommas. You guys kept me sane during university with endless escapades of bad ideas.

To all my remaining friends, my dorm and all of nanoscience, Thanks, stay classy.

ABSTRACT

Modern synchrotron radiation sources have shown enormous potential in the research area of Computer Tomographies (CT). Increasing the resolution to assess spatial information at a microscopic level, making CT a promising candidate to acquire information about cellular components within mineralized bone-matrix.

New advances in Synchrotron Radiation increased brilliance much fold, producing 3d tomographies of unprecedented quality but increasing brilliance still leaves systematic errors caused by well-known X-ray phenomena. Beam hardening effect makes it difficult to obtain a uniform view of data. Reflection in high contrast areas where material changes greatly in density causes bleeding effects, making it difficult to correctly distinguish voxels representing different types of matter at the proximity of their interface, often high interest regions such as implants.

An imaging tool for fast and automatic micro-structural analysis of bones could provide an insight to assist diagnostics of bone-related diseases such osteoporosis or bone infection. Samples made from healthy goat bones and scanned at the European Synchrotron Radiation Facility (ESRF) builds the data foundation for analysis. This thesis provides a framework for the development of an automatic and probabilistic segmentation tool for bone-tissue classification with language `Python` as a development platform. The model includes solutions for modern-day systematic errors for X-rays science such as beam-hardening- and internal refraction effects, which cause difficulties for X-ray Tomography in general, not just for the current setting.

The segmentation model utilizes a combination of Generalized Gaussian distributions and non-linear optimization function for mathematical modelling. A series of bit-masks were developed through an iterative approach to obtain progressively better probabilistic descriptions of the data. The model

successfully managed to classify and extract internal cavities with geometries similar to blood vessels, capillaries and even Lacunae containing osteocytes. This model could provide an important basis for fast classification of different types of bone tissue, contributing to fast diagnostics of fatal diseases such as bone cancer or discover hidden mechanism within the interior bone-tissue.

CONTENTS

LIST OF FIGURES

Part I

INTRODUCTION

1

MOTIVATION

Synchrotron radiation has made great leaps in brilliance hence increasing the resolution of measured samples. In modern medicine it is still common to manually characterize histology. This is done by professionals highly trained in recognizing such tissue. The fact is histology is in 3d and even for the highly trained it is still difficult to conceive a pattern throughout layers. Another alternative is using machine learning. The difficulty is that for machine learning to work properly, vast quantities of already classified tissue data is needed. Either way, it falls back to classification by hand and this process is time consuming. High resolution micro-CT provides high quality data. Data can be analysed using different spatial dependencies creating both short and long range patterns across spatial structures. Patterns which can provide the basis for statistical modelling, and assist to estimate tissue segmentation from these patterns.

This thesis aims to develop an automatic analysis tool for spatial bone-tomographies and estimate the distinct types of tissue incorporated in μ-CT samples. Utilizing multiple Generalized Gaussian distribution depending on voxel intensities and four different spatial dimensions as statistical basis for achieving a proper segmentation in a more interpretive framework with minimized ambiguity between classified voxels. This model would accelerate the process by multiple magnitudes, only taking a few minutes compared to several days.

2

THESIS OUTLINE

Bone tomographies have been scanned with most recent technologies in synchrotron radiation, that yields micro-scale resolution with a single ”volume cell” (voxels) being the mere size of $1.85\mu m$. This resolution yields high quality data that can give a deeper understanding of the bone-matrix. The microscopic structure of bones hides information about the physical condition of bone. The scope of the thesis are to separate the hardened bone-matrix from interior blood vessels, capillaries and cells by using a probabilistic model on voxels intensities in the tomography (CT) to estimate type of tissue. Recent discoveries revealed common bone cells, the osteocytes acts as an endocrine cell[28][1][12] further highlighting the interest in the bone cells.

The theory sections focuses on two pillars which support the field of research, osteology and X-ray physics. First we start with a top down approach to the biological system of bones, starting from bone being build by two different types of bone matrix: Cortical- and trabecular bone. These types will be explained including other macroscopic tissue i.e. bone marrow and how varying ratios of the two types constitutes all bone in organisms. The bone CT's provided are made of cortical bone, so an in depth explanation of the microscopic components of cortical bone will be provided. The main component in cortical bone, osteons and their internal components and functions are evaluated. Lastly the different bone cells will be explained and their individual role in bone remodelling.

X-rays physics will work through the basic elements of absorption, scattering, refraction, coherence and X-ray generation. This build a foundation for how specific machinery utilizes these phenomena.

Then, features of the spinning anode and synchrotrons will be explained how these technologies incorporate the basics, allowing for measurement. Wrapping up the theory section we go through an in depth explanation of how CT's are made and how a variety of calibrations may improve or affect the resulting CT.

The methodology section clarifies the iterative approach taken to create an automatic segmentation function. Every step and thought will be elaborated during each evaluation. Each step in the iterative approach will have an individual section. Samples are made from healthy goat bones and scanned at the European Synchrotron Radiation Facility (ESRF). The basis of analysis is made by the assumptions that distinct peaks in histograms of voxels intensities, represents a type of tissue within the CT i.e. a class. To estimated a class, a probability distribution will describe how probable, given the data, that a specific voxel belongs to at certain class. To evaluate probabilities the model chosen are Generalized Gaussian Distribution (GGD), a type of Gaussian, but with more prominent peaks and heavier tails. A distribution used in multiple image analysis studies[5][14]. Matching the GGDs with raw data was a least squares method[4] with an optimization function made by texttttScipy, a python library for data analysis. Four GGD models were made all depending on voxels intensity and their individual respective dimension, radial, Z, Y and X. Multiple segmentation approaches were tested with masks applied continuously, until a segmentation product was finished.

The results and discussion section are beam hardening effects are discussed from effects visible in radial- and Y-histograms. It turns out this information can be extremely useful to correct the beam hardening effects, yielding a more uniform signal.

Before creating the CT's were the bone specimens prepared to with a screw implant inserted in to the bone, to act as support and allow for tracking the vertical bone-growth. Bone mass density (BMD) is calculated to estimate vertical growth along the implant, showing that BMD can be estimated with micrometer precision.

3d visualizations peers into the spatial components of tomographies and evaluates internal morphology briefly and their possible origin. This done to assess how the processed data can represent the

internal components as blood vessels, capillaries and osteocytes. These 3d visualizations may allow for further analysis and understanding of microscopic event inside the bone.

2.1 SOURCE CODE

All the code used:

https://sid.erda.dk/sharelink/fpfpq69U7V

https://www.scipy.org/

http://numpy.org/

https://docs.scipy.org/doc/scipy/reference/ndimage.html

https://www.h5py.org/

Part II

BACKGROUND

3

BACKGROUND

3.1 BONES - BIOLOGICAL SYSTEM

3.1.1 *General facts*

Bones are the supporting structure of the entire body, protecting fragile tissue, largest mineral storage unit, production of cells essential for homeostasis. In mammals there are two types of bone tissue. Cortical bone (compact bone) and trabecular bone (spongy bone) and all bones are a mix of both, depending on the function of the specific bone, the ratios of cortical- and trabecular bone varies for different bones of the body[26]. Interconnecting bones are the skeletal cartilage. Cartilage (Cartilago in latin) are gel like substance which are made up of connective tissue and extra cellular tissue. In infant stages of life, the majority of mammal bones are made up of cartilage, later hardening into denser bones. This allows for the bones to grow bigger more easily[9]. Later in life the majority of remaining cartilage are articular cartilage that resides in joints in e.g. knees, rib and vertebrae.

Common bone tissue are effectively made up of $\frac{1}{3}$ collagen and $\frac{2}{3}$ mineral. The mineral adds strength and stability to the bone, while the collagen adds to the flexibility and tensile resistance to the skeleton. Besides physical stability benefits, are bones also the epicenter of many types of blood cells, with white- and red blood cells are most common. Blood cells are made in red bone marrow. The

red blood cells distributes oxygen and removes carbon-dioxide from the body[17]. White blood cells are an essential component of the organism immune system. White blood cells exterminate intruding pathogens, which emphasizing the importance of healthy bones to the homeostasis [8]. Excess energy are stored in form of yellow bone marrow located in the center of the elongated part of long bones[9]. The total bone mass contains 99% of the organisms calcium deposits[9]. Studies have shown lactating females can harvest minerals from the bone deposits to produced breast milk for infants, experiencing temporary osteoporosis [27].

3.1.2 *Macroscopic bone*

On the macroscopic scale the bone consist different types of bone, making up all bone matter. Cortical bone and trabecular bone.

3.1.2.1 *Cortical Bone*

Cortical bone(compact bone) are the more dense and less porous and makes up to 80% of the total dry bone-mass [26]. Cortical bones are usually located on outermost layer of the bones acting as a protective layer for the hollow inner bone, adding stability to the organism [26]. The highest fractions of cortical bone-matrix are found in long bones, which are situated in the extremities of the organism.

3.1.2.2 *Trabecular bone*

Trabecular bone(Latin: substantia spongiosa) also known as spongy bone are the lesser dense part of the combined bone matrix, though being more flexible [26]. Spongy bone structure are made up of beams and plates known as trabeculae. These trabeculae are orientated in seemingly random directions, but mostly in the supporting direction of the bone [9]. The collective cavities of the trabeculae are filled with either red- or yellow bone marrow [26]. The bones with the highest fraction of trabecular bone are the vertebrae.

In long bones the elongated part of the bone, the diaphysis are mainly cortical bone with trabecular bone in the center. The edges of the long bone, known as epiphysies. These are mostly trabecular with only a thin layer of cortical bone enveloping the trabeculae. The transition between the epiphysis and the diaphysis are called the metaphysis. The periosteum and endosteum are a thin sheet of connective tissue surrounding the outer- and innermost layer of the bone respectively as seen in Figure 1.

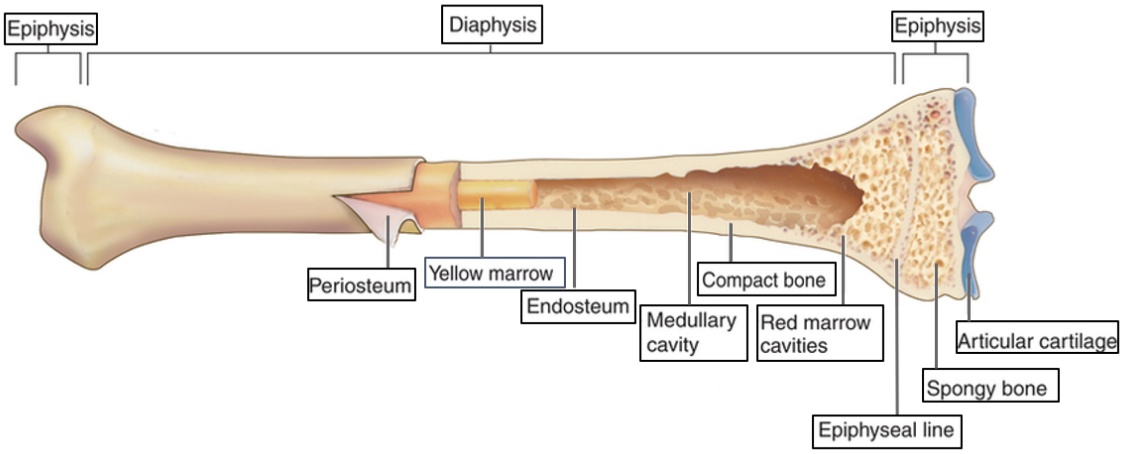

Figure 1: A partial cut through of a long bone, illustrating combination of Cortical- and trabecular-bone included with internal cites for the different type of marrow and the periosteum and endosteum.Figure are from[18]

3.1.2.3 *General bone-matrix*

This section will stroll over the general bulk components of making up the the bone-matrix. The extra cellular bone-matrix consist of both organic and inorganic components. In adults, 90% of the organic components are collagen, while the remaining is made of proteoglycans and cytokines[9]. The proteoglycans are long chains of hydrophilic proteins, allowing more efficient diffusion within the bone matrix[9]. The inorganic part consist of calcium salts known as hydroxy-apatite crystals with the condensed chemical formula $Ca_{10}(PO_4)_6(OH)_2$ [9]. Crystals are plate- and rod-shaped with thickness of $3nm$ and height of $60nm$, these are attached to the ends and inside of the collagen-

filaments adding strength to the structure. The synergy between organic and inorganic components add sturdiness and flexibility to the combined bone-matrix, making the bone resistant to torsion.

3.1.3 *Microscopic Bone*

Lamellar layers in alternating direction for each layer resistance torsion.

Zooming in on cortical bones we find haversian systems within the structure, also called osteons. Osteons are tightly packed cylindrical shaped systems, running parallel along direction of the cortical bone-matrix [9]. A single osteon consist of multiple constituents. Centering the osteon is the haversian canal with an average diameter of $150\mu m$ and a length of $3mm$. Theses canals acts as pathways for blood vessel and nerve, delivering nutrients and receiving signals from the the bone cells[19]. Encapsulating the haversian canal are typically 15 concentric lamellar layers with a thickness of $3\mu m$ each. These lamellar are made of the connective tissue collagen I[9]. The Lamellar layers alternate in the the spirals around the haversian canals adding resistance to torsion, this are illustrated in Figure 2. Circulating around the haversian canal are small oval cavities known as lacunae. Inside lacunae are common bone cells residing, the osteocyte. Intertwining lacunae with the haversian canal, are the delicate network of thin canals, known as canaliculi[20]. This delicate network of the canaliculi allows the osteocytes to communicate with each other and transport nutrients throughout the bone[7]. Wrapping up the entire osteon is the cement line, that is made of heavily calcified minerals[9]. Osteons get the flow of blood from the outside the bone and osteons sometimes have blood vessels going perpendicular to the direction of the osteons, these are called Volkmanns-canals as depicted in Figure 2. They interconnect osteons and blood vessels outside the bone, where the main supply of nutrients imported. Bloodflow inside the bone are not affected by high blood preassure[21]. The collective gathering of osteons in layers and along the bone wrapped up in the periosteum and endosteum creating the framework of cortical bones. If cortical bone is damaged, how does the organism respond to maintain homeostasis?

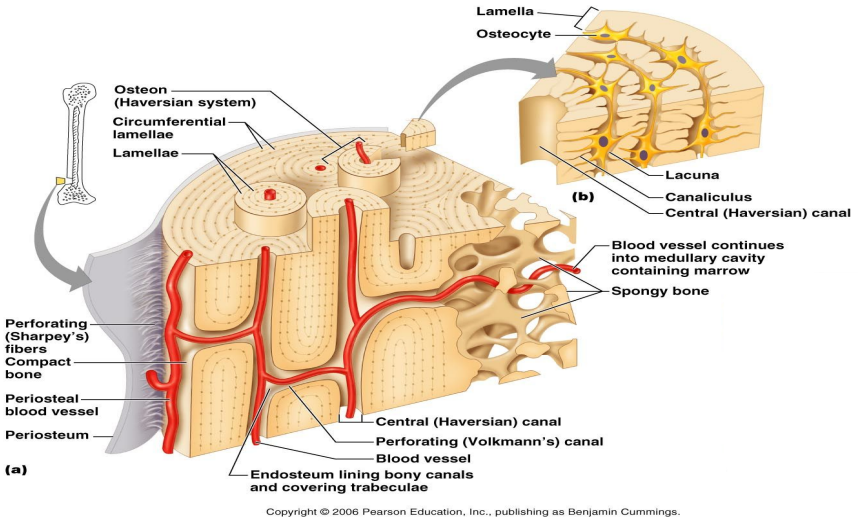

Figure 2: Figure 2a depicts chunk of cortical bone bordering to trabecular-bone within the cortical bone are a delicate system consisting of multiple osteons clumbed together. Cut through of osteons reveal the haversian canals traversing the osteons with Volkmanns canal interconnecting outside blood vessels and inner trabecular system. Figure 2b illlustrates osteocytes radiating in layers around the haversian canals with canaliculi perculating in all direction interconnecting Lacunae. mad prob to pearson, remember to write them

3.1.3.1 *Bone cells*

Osteogenic progenitor cells are a type of cell lying on the periosteum and endeosteum as pre bone-cells that differentiate into other bone-cells when they are needed.

Osteocytes, the osteocyte is the most abundant cell in the bone matrix and is known as the common bone cell. It resides inside the lacunae where it is wired the surrounding cells via the canaliculi. The osteocyte network act as a three-dimensional sensor, detecting micro fractures and communicating to systems in bone [6]. When a microfracture is registered, the osteocyte signals initiate the process of bone remodelling, where old bone matrix are broken down, reabsorbed and replaced by new bone-matrix[13]. The lacunae have an average size of $500\mu m^3$[22]. Osteoclasts are huge multi-nuclear cells responsible for the dissolving old bone-matrix and reabsorbing it into the system[13]. When a

micro fracture is detected by an osteocyte, they signals for osteoclasts to assemble at the site of the micro fracture. This first step is known as activation. Thereafter the osteoclasts dissolve and reabsorb the old bone-matrix into the system. The second step of bone remodelling: Resorption. This process allow for recycling of old bone matrix and clear out space for osteoblasts to initiate the rebuilding of bone-matrix. Osteoblasts, The osteoblast is the bone-building cell, controlling organic- and mineral deposition[20]. They arrive at the area cleared by the osteoclasts, then deposits osteoid, a collagen derived matrix in to the cleared cavity. The osteoid acts as support for crystals to mineralized around. When the osteoblast is done depositing, it goes into differentiation, turning into one of two other types of bone cell. They either differentiate into an osteocyte by fusing into the osteoid creating a cavity with dendrite arms percolating in all directions creating canaliculi and connects with proximity lacunae[7]. Only 10% of osteoblasts turn into osteocytes[9]. The rest become embedded into the surrounding matrix as lining cells staked and shaped like pancakes. This ends the process of of bone remodelling, resulting in new better bone. This step is known as Formation: Last step before returning to quiescence, the resting state of the bone[25].

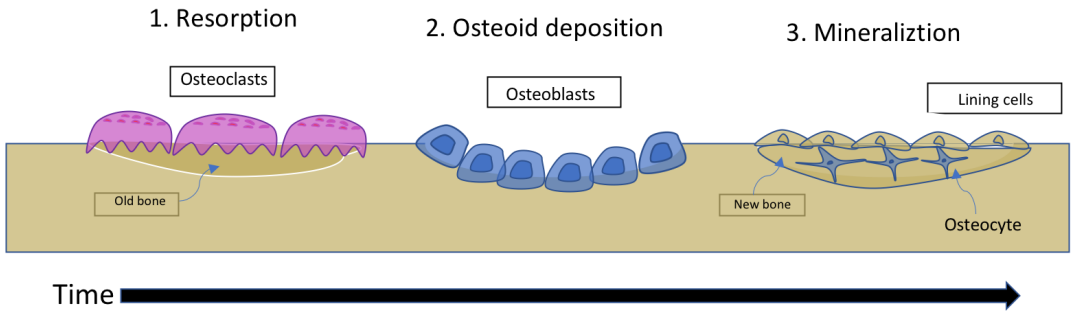

Figure 3: Bone remodelling process: 1) Osteoclasts arrive at area signalled by osteocytes and begins to dissolve old bone matter and reabsorbing the dissolved bone again. 2) Shortly after osteoblasts arrive and begin depositing osteoid into the cavity left by the osteoclasts, the osteoid is the organic part of the bone-matrix and act as support hydroxi-appatite crystals. 3) Mineralization and osteoblast differentiation. Osteoblast either merge with the surrounding bone tissue becoming lining-cells or embeds into the osteoid turning into osteocytes, after the osteocytes is embedded the new bone tissue starts to mineralize, becoming the known bone-matrix

3.1.4 *Analysis of bone material*

Numerous methods for bone analysis are available for the investigating the bone matrix. Some are Optic microscopy(LM), Transmission electron microscopy (TEM), Scanning electron microscopy and many more. But all of the previously mentioned techniques are tools for bone-analysis of bones extracted from an organism. with that TEM and SEM are also harmful to the sample, degrading the bone material while measuring. Other non harmful techniques for investigating bones inside the organism are ”computer tomography” or more formally, CAT- or CT-scan. This method applied by emitting a thin beam of X-rays, rotating around the bone, creating slices or 2D images of the cross sections exposed[10]. These images are the combined by sophisticated computer software, creating a 3D image of the tissue. The first time bones were examining from within the body was back in 1895 where William Röntgen discovered a new type of photons, calling them X-rays, due to them being

unknown prior to this[29]. Röntgen managed to capture an image of the bone inside of his wife hand, where all finger- and wrist-bones, as well the wedding ring was visible, while all other soft tissue was absent as seen in Figure 4.

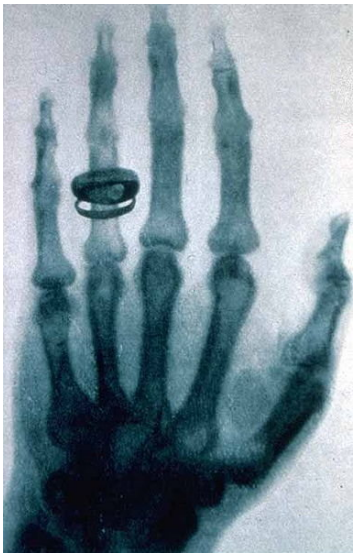

Figure 4: First X-ray image ever taken by William Röntgen of his wifes' left hand. All soft tissue are gone only showing the more dense components as bone and rings

Providing an unprecedented imaging tool at the time, paving the way for the modern CT-scan. But how are images made with X-rays? And how does X-rays interact with matter? And how are x-rays made? All these question and more will be answered in the following section, X-rays.

3.2 X-RAYS

X-rays are electromagnetic waves, typically residing in wavelengths(λ) of several Ångstrom($10^{-10}m$) typically $10^{-8} - 10^{-12}m$. When dealing with photons, energy is inversely proportional with wavelength. The relation is given i Eq. 1.

$$\lambda = \frac{hc}{E} \tag{1}$$

h: Plancks' constant, c: The speed of light in a vacuum and E: The energy in KeV.

The interesting property of x-rays are that they interact with electrons around atoms. When interacting, one of three things occur, photons are scattered, absorbed or simply transmits through without interacting with the medium. The interchangeable play between these outcomes yield interesting information about the internal structure of the atom or molecules being investigated. The latter two will primarily be discussed, due to the scope of computer tomographies being generate solely from the relationship between absorption and transmittance a density can be estimated of the material[2].

3.2.1 *Scattering*

Scattering are phenomena occurring when photons strike an atom by collision. This collision can result in a redirection, changing the course of photons in new random directions. When a photon is scattered two types of scattering can occur, elastic- and inelastic scattering. The latter is when the photon energy is changed after interaction often referred as Compton scattering. Compton scattering occurs when the charged particle interacting with the photon are able absorb a percentage of energy as vibrational energy, leaving the photons will less energy when scattered. This can also occur vice versa, a vibrational agitation electron transfers energy to the photon leaving the scattered photon with

more energy. This is called inverse Compton scattering. More common are elastic scattering also referred to as Rayleigh scattering. Energy are preserved, changing only direction. Scattering effects are utilized in material-sciences to map the interior bonds between atoms e.g. in X-ray diffraction (XRD). Small angle X-rays scattering(SAXS),the scattering effects can explain the morphology of particles by backtracking scattering patterns extracted from scanning of specific samples[2].

3.2.2 *Absorption*

A free electron exposed to a photon, will it absorb the photon and start to oscillate in spherical patterns. The more energy added the greater the amplitude of the electrons oscillations will be. After a brief moment of excitation are the photon remitted as Thomson scattering, which is elastic scattering from free particles. The same is evident for electrons around a single atom, the electron will transition to a higher energy shell before the remitting the photon. Molecules exposed X-rays experience slightly different effects, when an electron absorbs an X-rays, an electron from the inner shell are ejected into the continuum of the molecule, leaving the atom partially ionized locally in the molecule. The effect of X-rays ejecting electron from the atom are called the Photo-electric effect. The atom in responds fills the vacancy with another electron from a higher energy band, emitting a new photon with the same energy as the difference between the two bands. This process is called Fluorescent X-ray emission. The atom may emit an additional electron instead of an X-ray, when a neighboring electron fills the vacancy the excess energy is transferred to the other electron. These electrons are referred as Auger electrons[2].

These collective absorption phenomena can deduce the absorption coefficient μ of the exposed material. The absorption coefficient how much absorption occurs pr unit depth as Eq. 2 explains.

$$\frac{dI}{I(z)} = -\mu dz \tag{2}$$

Where $I(z)$ can be found with Eq. 3.

$$I(z) = I_0 e^{-\mu z} \tag{3}$$

I_0 is the initial intensity of the beam, $I(z)$ is the intensity at depth z. A proportionality factor σ_a defines the atomic absorption cross section. The atomic cross section describes the area of the surface affected by the flux of photons. The absorption coefficient μ is related to the cross section by:

$$\mu = \rho_a \sigma a = (\frac{\rho_m N_A}{M})\sigma_a \tag{4}$$

N_A, ρ_m and M being Avogadro's constant, mass density of the element and molar mass. Samples containing multiple elements, are the combined absorption factor estimated with Eq. 5.

$$\mu = \sum_i \rho_{a,i} \sigma_{a,i} \tag{5}$$

Analysing multiple elements, the atomic absorption cross section was empirically found to be $\sigma_a \propto \frac{1}{E^3}$. The photoelectric absorption cross-section varies with the atomic number Z, approximately as Z^4 [2].

3.2.3 *Refraction*

All types electromagnetic radiation exhibit refraction when interacting with a medium. Visible light are very prone to refraction as its the individual wavelength can be separated due to different refractive indices, with Newtons prism experiment being a of the more famous. X-rays also refracts, though to a lesser extend. The refractive index is a scale of describing the angular shift in path compared to the incident angle. Snell's law describes the relation between surfaces:

$$cos\alpha = ncos\alpha' \tag{6}$$

n is the refractive index, describing the offset angle induced by a material. α and α' are the incident angle and refracted angle respectively. X-rays interacts weakly with matter, with an absorption length of millimeters. Compared to visible light with absorption length of nanometers $"Refs"$. A factor 10^6 difference in absorption length. X-rays refractive index are slightly smaller than 1[16]. This relation are described below in Eq. 7.

$$n = 1 - \delta - i\beta \tag{7}$$

δ are typically in the order $10^{-4} - 10^6$ and only 10^{-8} in air[16]. β the imaginary part are magnitudes smaller than δ, typically leads to neglecting β. With the relation of Snell's law in Eq. 6 the critical angle α_c can be estimated, the angle where X-rays undergo total external reflection. Combining Eq. 6 and 7 the critical angle can be derived as so:

$$\alpha_c = \sqrt{2\delta} \tag{8}$$

Since the refractive index $n/approx1$, the critical angle is comparatively small. But depending on energy and material the critical angle α_c may vary, but typically at a few milli-radians.

3.2.4 *Coherence*

Coherence is the holy grail in X-ray imaging and play crucial role in quality of measurements. The word coherence mean "the quality of forming a unified whole". Dealing with light, coherence is the collective amplification between photons with identical properties[3]. Electromagnetic waves has quite a few factors affecting the coherence and in reality perfect coherence are nearly impossible to achieve. Characteristics of a single photon is wavelength, the distance between each wave-front λ, amplitude, the relative height of the wave tops and valleys. Phase Φ is the relative translation and direction of the propagating direction. These 3 key features of photons are illustrated in Figure 5a.

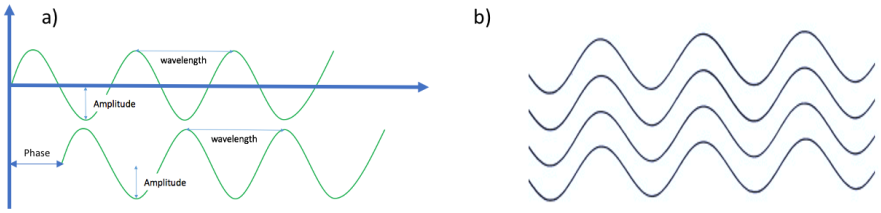

Figure 5: Illustration of simple wave properties. Figure 5a showcases two waves and their respective amplitude, wavelength and relative phase difference. Figure 5b illustrates perfect coherence with identical wavelength, phase and direction.

Other parameters also characterize photon properties e.g. polarization, but for the sake of simplicity will be neglected.

Coherence arise when collective properties of photons match, but on the trail towards perfect coherence, do many problems arise. Some are, light sources that emits one wavelength without deviation in wavelength. This is in time impossible due to Heisenberg's uncertainty's principle, disallowing photons created without uncertainty[23]. Another problem is the divergence of conjured beam, no matter how well focused a beam is, some sort of beam divergence will occur[23]. The concept of perfect coherence are illustrated in the Figure 5b.

Coherence are important, the increasingly coherent a beam are, thus easier it is to explain internal effects of measurement.

The following section will cover some of the many solutions trying to counteract the effects of incoherence.

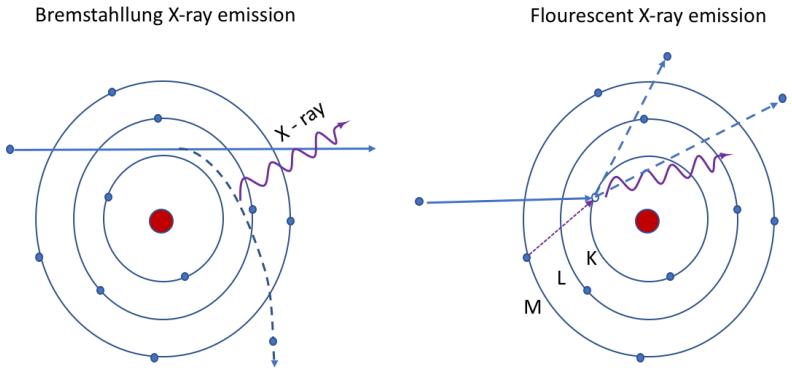

Figure 6: To the left are the Bremstrahlung effect, while on the right are the Flourescent x-ray emission illustrated.

3.2.5 *X-ray generation*

The are two commonly utilized mechanism for generating X-rays. The first is deceleration of charged particles at high velocities, the loss of velocity emits X-rays with same energy lost in velocity. This is called the Bremsstrahlung effect from German, meaning ”Braking radiation”. This effect is utilized by bending an electron at high velocity by either collision with a metal anode or applying a rapid changing magnetic field. The energy spectrum of Bremstrahlung X-rays are very broad due to the electrons are bend to various degrees especially when colliding with a metal anode. The other method generates X-rays through discrete atomic transition. Electrons are accelerated by an electric field towards a piece of metal. The electron colliding with the electron of the metal anode eject another electron from inner shell of the atom out into the continuum. The atom compensates by filling the vacancy in with an electron from the L or M shell. The discrete shell energy difference are emitted as an X-ray. Depending on the which shell the electron jumps from determines if it’s K_α- or K_β emission.

These being methods utilizing for X-ray generation for analysing purposes. The following section goes over how these concepts are utilized for specific measurements.

3.2.5.1 *Brilliance*

Before diving into the intricate machinery, making measurements, the term brilliance presented and walked through given these apparati try to enhance brilliance. Brilliance is a quality measure of the X-ray beam produced by equipment. Brilliance are broken down into four components. Intensity: The number of photons pr unit time through a cross section i.e. flux. Angular beam divergence given in milli-radians squared, to account for the cross section area of the beam. Collimation, the area of the beam source. How well the beam are focused upon the sample. It's given in mm^2. Band Width (BW) is the spectral range, the monochromator crystal emits when filtering wavelengths the beam. BW in third generation synchrotrons are 0.1%. The reasoning of this interval, are to more easily compare different measurement. These four components adds to brilliance, shown in Eq. 9.

$$Brilliance = \frac{Intensity[I]}{beam - div[mrad^2] * source - area[mm^2] * (0.1\%BW)} \tag{9}$$

The denominator states a smaller area with narrow range of photon energies yield higher resolution and lesser deviation in output. While the numerator constitute, higher counts of photons amplifies probability of interacting with all components in the sample, especially elements with lower atomic number. Next section focus on how common apparati utilize brilliance to yield high quality measurement

3.2.6 *Spinning anode setup*

One of most common tools in small scale laboratories are the spinning anode setup. This setup utilizes a mix of the Bremsstrahlung and Fluorescent X-ray emission. A current is placed upon a system with wolfram filament and rotating plate of copper(copper is the most common) are coupled. The

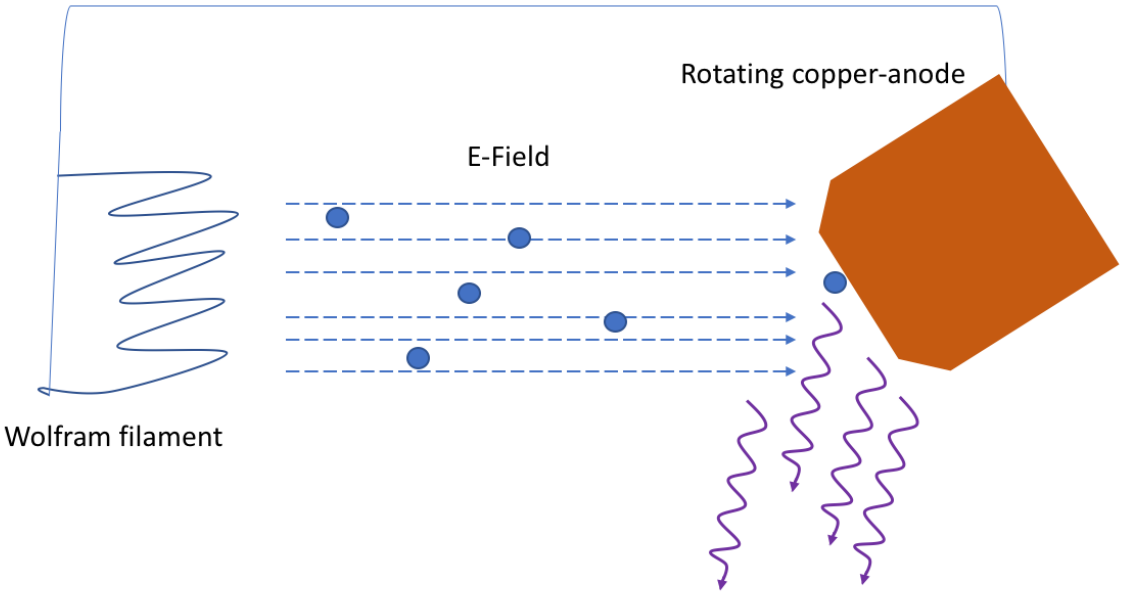

Figure 7: Rotating anode setup: Electrons emitted from the filament are accelerated towards the copper anode. When electrons collide with the anode it creating X-rays through Bremsstrahlung or X-ray fluorescence

Current charges the wolfram negatively and the copper positively creating an electric field between the two metals. The copper-top rotates to expose more surface area allowing for more durable anode. This negative charge stack electrons on the wolfram cathode. When the force reached a critical point, ejecting electrons from the cathode, accelerating towards the copper anode. The electrons collide into the anode, x-rays are created from the two previously mention effects, scattering in all directions. Figure 7 shows how the setup generates X-rays. A place in the lead covered case, a filter sorts photons allowing high energy X-rays to pass, while lower energy photons are reflected. The escaped X-rays are filtered through a multi layered mirror extracting only the desired wavelengths. The X-rays are redirected towards the sample. Towards the sample, the beam are reshaped by multiple layers of minimal scattering slits, shaping the beam to fit the sample. The setup has a low brilliance due to the beam only consisting a fraction of the photons generated. The energies are dictated by the anode in use(typically copper). The advantages are availability and measurement can run for hours, to improve the quality marginally. Disadvantages are the lower number of photons i.e. lower brilliance.

3.2.7 *Synchrotron radiation*

Synchrotrons are huge ring shaped installations with in build mechanism applied strong magnetic field on packs particles to travel at relativistic speeds in along curved paths creating synchrotron radiation a form of Bremstrahlung X-rays.

The first synchrotron was made in 1970s and upgrades have been coming continuously since. Now at third generation synchrotron technology the brilliance have increased with approx 10^{12}, delivering 1-500 KeV (wavelength: λ 12Å - 0.0248Å). The rapid advancements in brilliance over the year are illustrated in Figure 8.

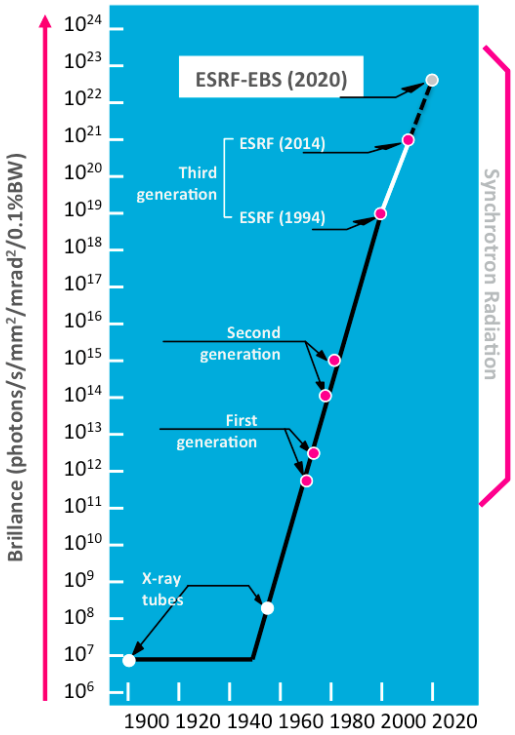

Figure 8: Improvements of Brilliance in X-ray devices over the years. ESRF being a front runner since 1994 and intend to stay the course with Extremely Brilliant Source (EBS) project which goal is to improve the storage ring even further[15]

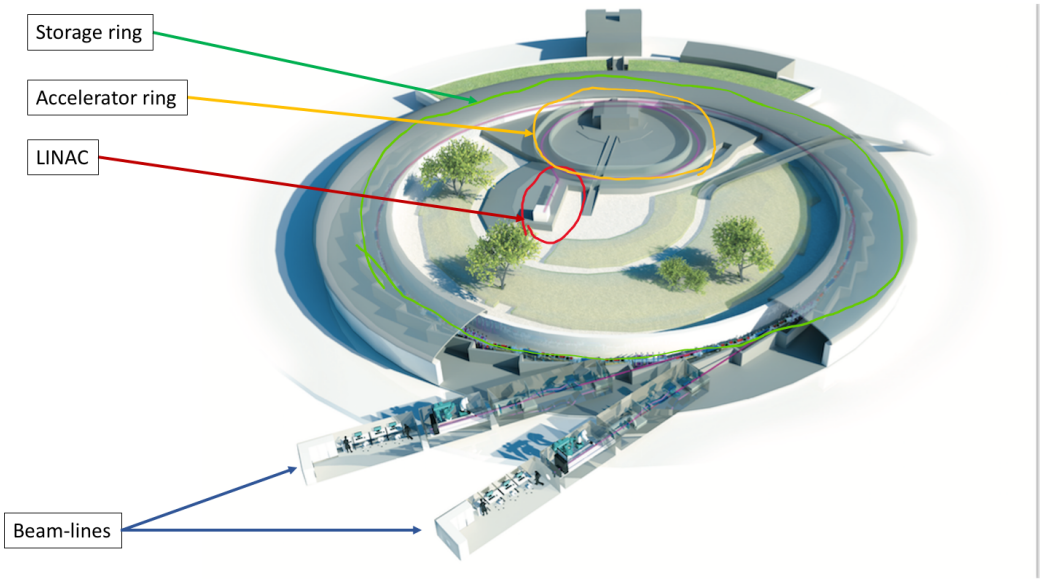

Figure 9: The three major structures in the ESRF synchrotron. The red area is the LINAC, Linear accelerator, responsible for generating electron and initial boost. The yellow segment is the booster ring which accelerates the electron to relatisvistic speeds before injecting them in the the storage ring. In green, the storage ring that keeps the electrons going and houses all the insertion devices, focusing magnets and beam-lines[15]

3.2.7.1 *Rings of the Synchrotron*

A synchrotron consist of three large scale compartments: The storage ring, the booster ring and LINAC. LINAC are an acronym for linear accelerator, the LINAC create electron bunches from a wolfram plate, thereafter subjugating them to an initial speed boost before injecting them into the booster ring. The booster ring is situated inside the area of the storage ring. In the booster ring are the electrons accelerated to further energies levels, up to several GeV. Finally injecting them into the storage ring. Near vacuum conditions are induced in all rings before injecting electrons.

Breaking down individual components of the storage ring. It is not an actual ring but a pseudo ring comprising of straight and curved compartments. Curved segments contain two dipole bending magnets both situated at their respective ends the compartment. Preservation of speed and forces electron bunches to change direction following the ring. Midst the dipole bending magnets are

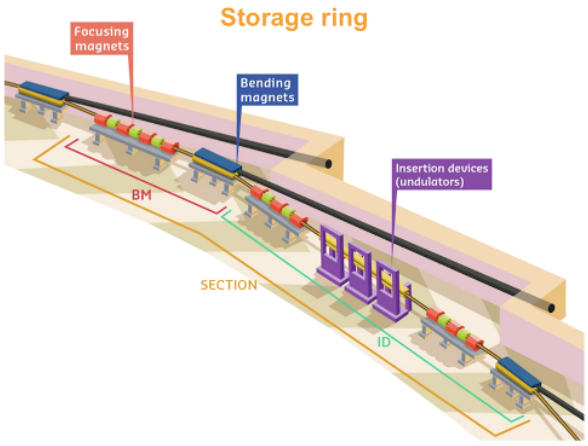

Figure 10: The red part is the curved part of a section with bending magnets(BM) that applies force so electrons follows the path correctly. The green section is the straight part which has an insertions device(ID) which generate X-rays for the respective beam-lines. All sections have focusing magnets installed to avoid electron repulsion, maintaining the high brilliance

alternating sets of quadro-, sextu- and octopoles magnets, maintaining tightly packed electrons, inhibiting repulsion. Also referred to as focusing magnets. The straight compartments are composed focusing magnets as well with insertions devices in between. A straight and curved segment are shown in Figure 10. Insertions devices have alternating dipole magnets forcing electrons to oscillate up and down. These oscillations creates multitudes of X-rays rapid changes of velocity. Two types of insertion device are used within a synchrotron: Undulators and wigglers.

3.2.7.2 *Insertions devices*

Undulators forces electrons to execute small oscillation in the horizontal plane as it traverses through straight section within the storage ring. Along the path an array of dipole magnets alternating up to down causes the electrons to oscillate thus to radiate energy. The produced radiation is very intense and concentrated in narrow energy bands in the spectrum, called coherent radiation.

Wigglers on the other hand, the amplitude of the oscillations is larger, resulting in an enhancement in the intensity, called incoherent radiation. It is spread out over a wide horizontal fan. These effects are illustrated in Figure 11.

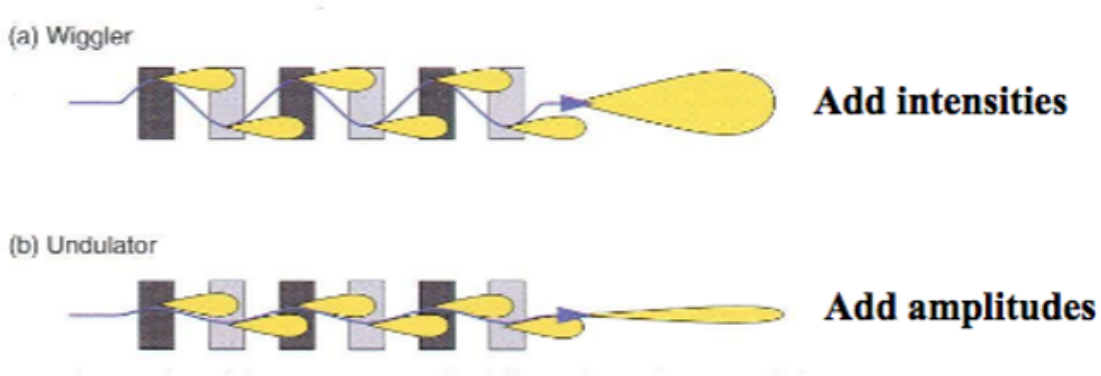

Figure 11: Wiggler oscillates the electrons with high amplitudes increasing the number of X-rays generated. While the undulators creates rapid oscillations adding coherence

3.2.7.3 *Beam lines*

Aligned with the insertion devices, a tangent like appendage to the storage ring are the beam-lines. Beam lines are where the science happens. Beam-lines can be situated at each straight compartment, making it possible to design many different beam-line depending on what kind of measurement desired. Most beam-lines do have a monochromator crystal. Monochromator crystals allow the selection of an energy from the continuous spectrum extracting the desired wavelengths. A focusing device that shapes the beam emitted from the monochromator and focuses it on the sample. At last type of sample-holder, which function is implied. Coupled with spectrometer made from an array of light sensitive semiconductor cells, that registers X-rays as voltage inputs convert it into intensities.[2] This setup can be modifying to fit for any desired sample. Usually resulting in different beam-lines connected to bigger storage rings are funded by external contributors to create different beam-lines for different purposes.

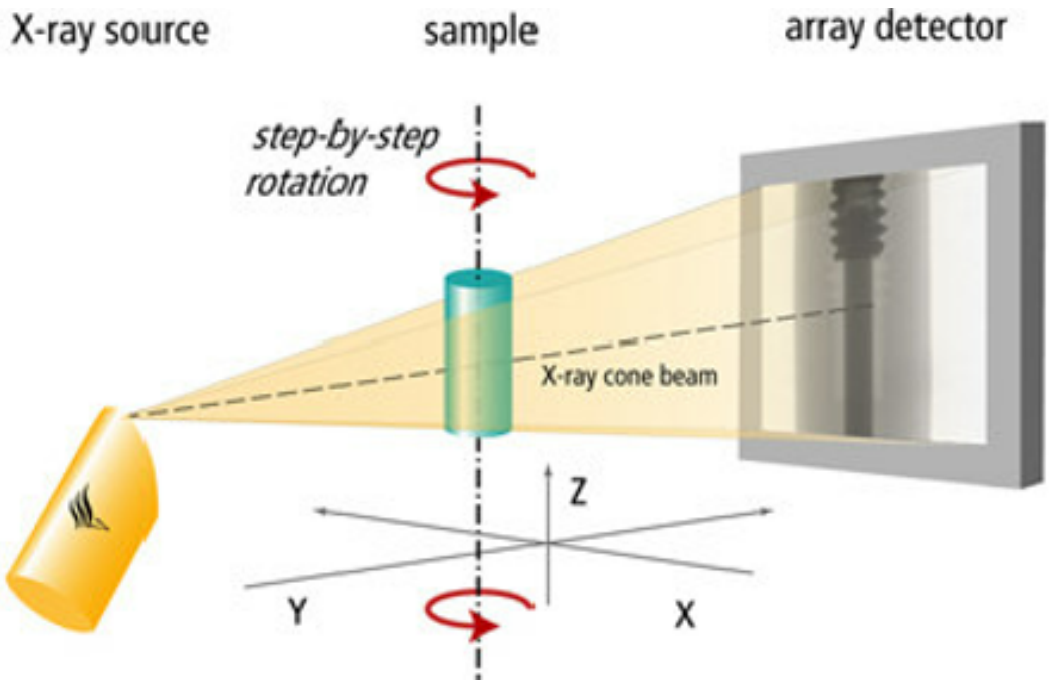

Figure 12: One of two sets up for creating tomographies, emitter and detector are locked in place while the sample is rotating with incremental radians. Each increment stores an image. The number of incremental measure images are extrapolated to 3d image.Image[30]

3.2.8 *Creating tomographies*

Common to all beam lines are the measuring stations, where transmission or scattering signals are obtained. Transmission signals are converted into a 2d image. These types of images are the data containing information about the sample. Some beam-lines offers the option of scanning samples while continuously rotating it. This creates an array of cross section images from the sample at different angles. The process for obtaining the array of 2d images are shown in Figure 12. These 2d images can be extrapolated with sophisticated computer algorithms, producing combined 3d image of the sample, granting an inside look into the sample.

To ensure quality measurement of tomographies are a variety of calibrations can be made. Source information about beam size and energy spectrum are essential, as previously mentioned are beam size important for detailed measurement, but too small beam may heat a region slightly changing density and structure. The energy spectrum are important to compare photon energies with the material for

the best attenuation. A polychromatic source containing many soft X-rays, can be negated with a filter, absorbing the lower energy photons. Rotational steps of the measurement can ensure high quality, more incremental steps can ensure highly resolution of measurement. Disadvantages, it results in a prolonged measurement and exposure time, maybe affecting the sample. Sample material composition plays a crucial role of the measurent and knowledge of refraction indices between internal material surfaces might allow for greater correction. Geometry are crucial since different surface shapes induce noise and uneven reflection effects. Systematic errors from geometry and beam source can be corrected if a reference samples of same shape made of a homogeneous material are measure to trace possible edges- and attenuation factors. Higher symmetries and smooth surfaces counteract these effects. Detector relevant calibrations like pre-processing of detector to known energy sensitivity from transmission pattern. A reconstruction of these calibrations can give a far better edges detection of the samples individual voxels. Incorporating these calibration may enhance the final measured result allowing more effective data analysis [30].

This wraps up the method known as CAT-scan, an acronym for Computer Axial Tomograhpy or Computer Aided Tomography or Computer Tomography (CT). These scans are well utilized in medicinal imaging[10][11], but can in principle be included for sample scanning by synchrotron radiation. The advantages of CT-scan at synchrotron facilities are specifically tailored beam-lines to produce μm resolution pr. pixels and even nm resolution with high brilliance. These CT scans are extrapolated to grids of gray-scale values. These grids are interpreted as matrices, making them apt for vector analysis and create custom-made software for processing specific types of tomography data quickly and effectively.

Part III

METHODOLOGY

4

EXPERIMENTS

4.1 SAMPLE PREPARATION

7 healthy female goats at age 4 was chosen due to having similar metabolism and bone formation as humans. The goats were sedated and operated A $25mm$ long and $4mm$ deep defect was made in the mandibular base(jaw bone) of the goats. Within the defect was 5 titanium dental screw implant of diameter $3,5mm$ and length $8mm$ was spiraled $3,5mm$ into the defect of the jawbone exposing $4,5mm$ of screw. Placed over the implant was a titanium membrane acting as a support together with the screw-implant for new bone-material to grow on. The goats were then released and 20 days later they were euthanized and the bone-specimens were extracted[24]. The specimens were encased in poly-(methyl methacrylate) a type of resin, into cylinders of length $12mm$ and $7,5mm$ in diameter with the implant covering $3,5mm$ of them. The resin-bone cylinders were coursed and grinded to have identical dimensions. The bone-specimens were transported to the European Synchrotron Radiation Facility(ESRF). The samples was scanned in the beam line $ID19$ with a $67,4KeV$ ($0,183Angstrom$) energy source, sufficient enough to attenuate through titanium. The detector was a 2048x2048 pixel scintillator detector with pixel size of $1,85\mu m$. Samples were bigger than the detector, so each sample was scanned multiple times to include the full array of the sample in 4 sub volumes. At last a computer algorithm at ESRF computed the bone-tomographies from the ensemble of images acquired through

scanning, returning 3d gray-scale images of the scanned samples. A format fit for multidimensional image processing.

5

METHODOLOGY

5.1 OVERVIEW

This methodology section will act as a walk-through of multiple section where each sections follow the same structure, to create an overview for what to come: 1. Where are we, what is the plan? 2. Detailed walk-through of applying proposed plan 3. Evaluate intermediate results and point towards new approach based on results. Begging the process as the sample data are relatively new and very little is known. Then each step acquire new information which affect the following argumentation and new addition in methods. Coding experience was very limited and most ”trivial” coding problems at first took hours even days to solve. Knowledge of memory and computing power were closed to zero, so advancements in computing will also play a minor role in the choices made in correcting mistakes and optimize certain processes.

5.2 HYPOTHESIS

Bones from goats were measured at ESRF with Synchrotron radiation. Bones were scanned while continuously being rotated while measured. This yields a Computer tomography(CT) of the bone specimen. The CT contains voxels values which are derived from the intensities i.e. the number of

photons registered by the detector. A voxel is a 3-dimensional pixel and stands for ”volume cell”. The measured CT contains over 3 billions voxels, each with an intensity. If these intensities are plotted as histogram, with the y-axis as the frequency of the voxels intensity and the x axis as the intensity. This yields a histogram with 5 distinct peaks. Here the idea is, each peak represent a type of tissue within the bone CT, so if each peak can be described with a probability function i.e. the fraction of all voxels belonging to this class. Then voxels can be described as a probability of belonging to a certain class. This approach will allow for an analysis that estimates a class from a pure probabilistic stand point. This will be the assumption and foundation for analysis going forward in this thesis.

5.3 PREVIEW

The scope of this thesis is development and foundation of a quality segmentation method to classify bone-matrix and belonging internal components. A foundation which allow morphological analysis of the internal components, deducing if morphological geometries can be classified as bone-cavities, blood vessels, capillaries or osteocytes.

The main obstacle for achieving this goal are systematic errors induced by the effects caused by X-rays interacting with matter, especially when with attenuation i.e. beam-hardening effects related to depth. Interfaces between material different density cause bleaching/bleeding effects, resulting in improper contrasts. So dealing with these problems on an idea base, then implementing them afterwards.

The following subsections gives an overview of all steps taken to arrive at the final product, so all steps are introduced before explaining further. Flow-charts outline ideologies, thoughts, reasoning, explanations, implementations and other factors involved solving rising problem. Each bubble represent a subsequent section explaining and briefly evaluate each step, concluding a product of the final code.

5.3.1 *Sample correction*

The data obtained from cylindrical shaped samples scanned at ESRF were delivered in multiple files for each sample, so before initiating data processing, the data has to been multi-scaled to have different resolutions to process, different files had to be combined into one with correct overlap and excess voxels around sample to be removed as Figure 13 illustrates.

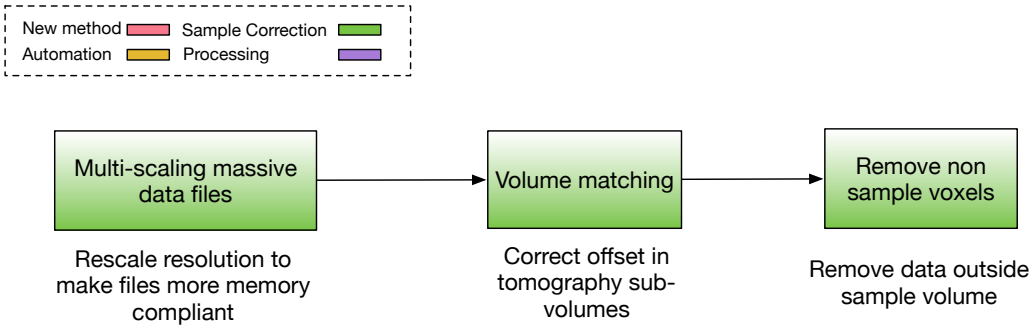

Figure 13: Illustrations of interventions taken to correct samples before the data processing could proceed.

5.3.2 *Initial analysis*

Figure 14 reviews getting acquainted with the multidimensional CT data and analysing the immediate features i.e. voxels intensities, geometry and visual representation of CT-slicing i.e. examining individual layers of the Z-, Y-, X-axis of the CT, a 2d image. A Generalized Gaussian distribution (GGD) were chosen to describe histogram of voxels intensities. GGDs have become more common in the field of image analysis, with prominent peaks and heavy tails to include signal multiple σ away. To describe data most effectively with the GGD was optimization function from Scipy implemented to minimize the difference between data and distributions. The minimized distributions were the used to classify voxels of the tomography.

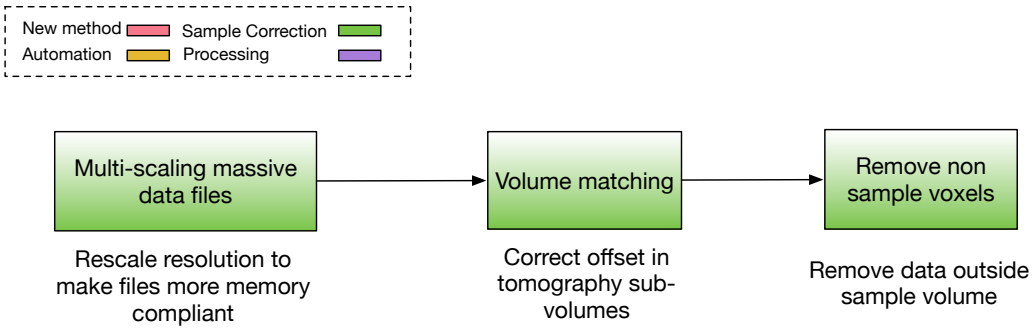

Figure 14: Initial steps of data processing

5.3.3 *Utilizing the spatial dimensions*

The initial classification test of CT-data, pointing towards more intricate methods to explain data more effectively, so a new approach was adapted as shown in Figure 15. More complex computation are introduced in attempt to access information through a layer-wise approach in the Y-direction. Histograms were generated from subsets of data instead of collapsing into one histogram, a histogram was made for each layer in the Y-direction. The rapid increase in histograms needed to be minimized called a function to automatise this, due to the sheer time it would take to do this manually. The functions was thoroughly tested and then the minimized histogram were used to classify the sample.

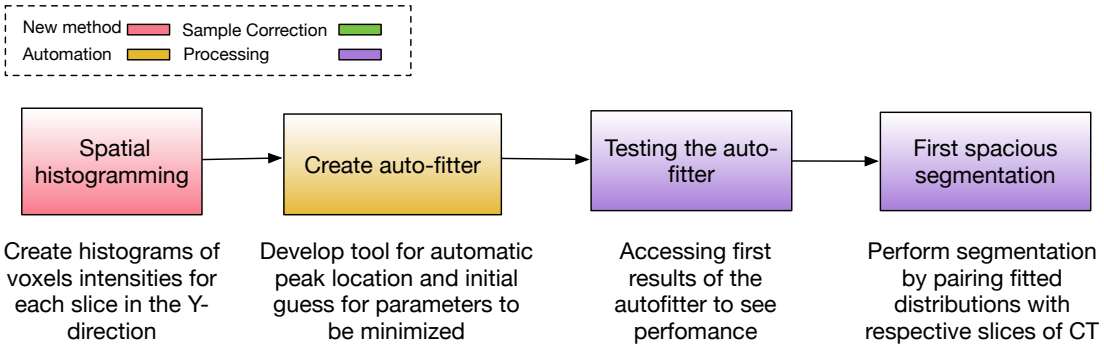

Figure 15: Expanding probability function to spatial dimensions

5.3.4 *Moving on from recent frontiers*

Figure 16 maps which initiatives are introduced to hopefully enhance specific regions and remove others entirely. The spatial procedure was expanded to additional dimension to check how bleaching affected their spatial sub-sets of voxels. Unnecessary data were removed from CT's to remove some of the bleached voxels and to avoid repeating calculations were the unnecessary data turned bit-mask to easily remove the data in future processing. Some of the bit-masks were flawed, so a bone bit-mask were made to ensure all bone- and interior voxels were preserved.

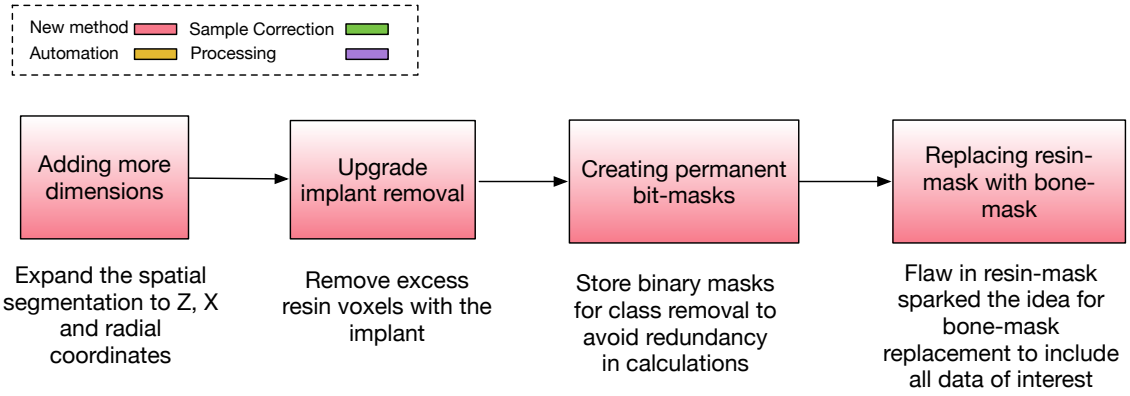

Figure 16: New initiatives added to the analysis

5.3.5 *Streamlining*

The final borders have been drawn and the final probabilistic models are ready to be combined to one unitary signal. Streamlining the process, final automation are added to simplify future analysis. Ensuring full automation were all the steps in Figure 17 carried out. The function for finding parameters for the GGD's, performed sloppy at time, so to upgrade performance were bounds introduced to limit the range the minimizer function would search to best values, effectively improving performance computational and precision wise. The GGD's describes a class each in their respective subset, but to sort all the GGD's into respective classes a function were developed. The function

evaluated all GGD's and sorting them into classes by comparing distribution overlap for each layer to determine if which class they belonged to. Finally, everything developed were combined to create a full automatic probabilistic segmentation model.

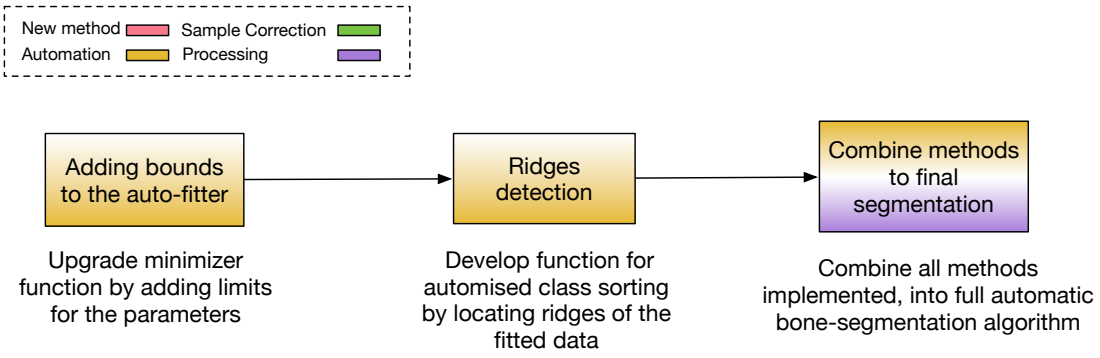

Figure 17: Final components developed to complete the machinery

These subsections wraps up what's in store while diving further into the methodology.

5.4 MULTI-SAMPLING DATA

The samples measured were millimeters in length and scanner had μ resolution, this creates CT's with billions of voxels pr. sample resulting in super large files, which creates a problem for most computers to handle. Producing fast executing code, a numerous amounts of tests are necessary while developing code. So super large files sizes, mean slow testing of code. So to speed up the production of software, were copies of the samples created at lower resolutions to accelerate development.

The detector at ESRF had a resolution of $1.85\mu m$ pr pixel and bone-samples being the millimeter scale the resulted the measured CT's were over 160 Gigabytes(gb) pr sample. More than most computers can hold in memory. A solution is to downscale the data, henceforth decrease the resolution. So copies of the original files have been made in decreased scale sizes of $\frac{1}{2}$, $\frac{1}{4}$, $\frac{1}{8}$ and $\frac{1}{16}$. This down-scaling allows faster testing of software, resulting in more efficient development of code. But when the effective software has been developed, will the high resolution data be processed, since it

carries the most information. How the down sampling was executed will be explained for 2d, then for 3d which is the case for this type of data.

5.4.1 *2D - sampling*

Imagine the simplest image at 2x2 scale, where the first axis will be denoted with i and second with j. Now the method to be performed specifically here is the area down sampling. To illustrate the framework for the down sampled image a new pixel will be placed inside the 2x2 image, the sides of this pixel will be denoted x and y. To estimate the value of the new pixel, sub-areas of each fraction of the pixel subsiding in the four other pixels of the 2x2 image, will be calculated. The lengths of the sub-squares for y and x will denoted accordingly to i and j respectively. When calculations of sub-areas are done, they are multiplied by the residing pixel. This preserves some of the information inside the four pixels and combines them inside a new one xy.

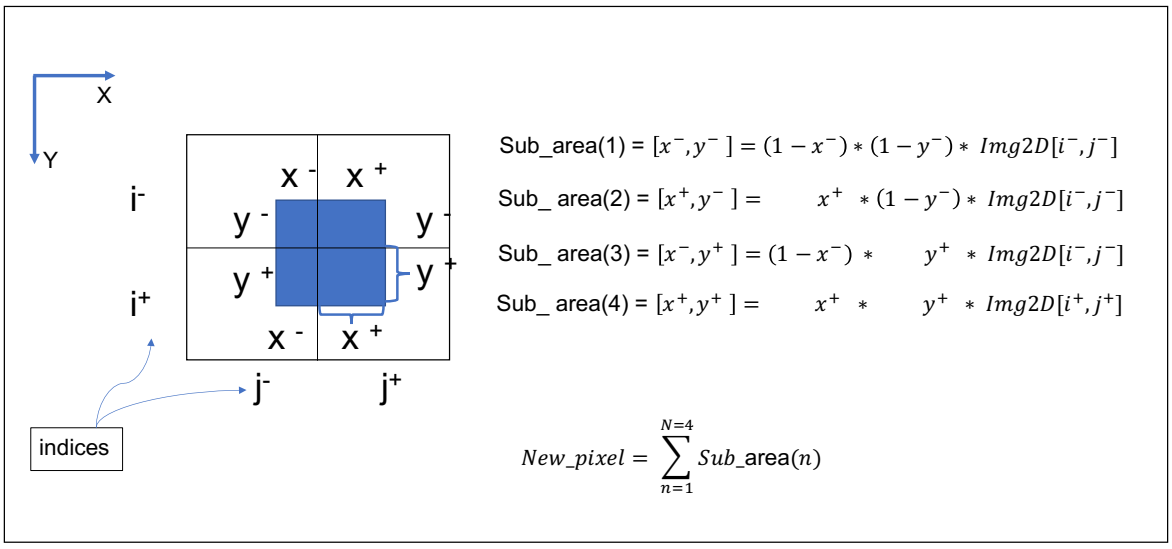

Figure 18: Each blue segment inside a pixel represents the sub_square area. The area of these sub_squares are then multiplied by the value of the overlapping pixels and summed up in the end yielding the value for the down-scaled pixel

5.4.2 *3D - sampling*

Adding another dimension from 2D to 3D, down sampling is rather simple when the basics from 2D sampling are understood. Now illustrating down-sampling with a 2x2x2 image with the three axis being denoted by k, i and j. A box of the dimensions 1x1x1 is placed inside the 2x2x2 image with the lengths z,y and x. Only difference from 2D is instead of calculating 4 sub-areas, 8 sub-volumes are calculated for the sub-volumes inside their respective box in the 2x2x2 image. This illustrated in Figure 19.

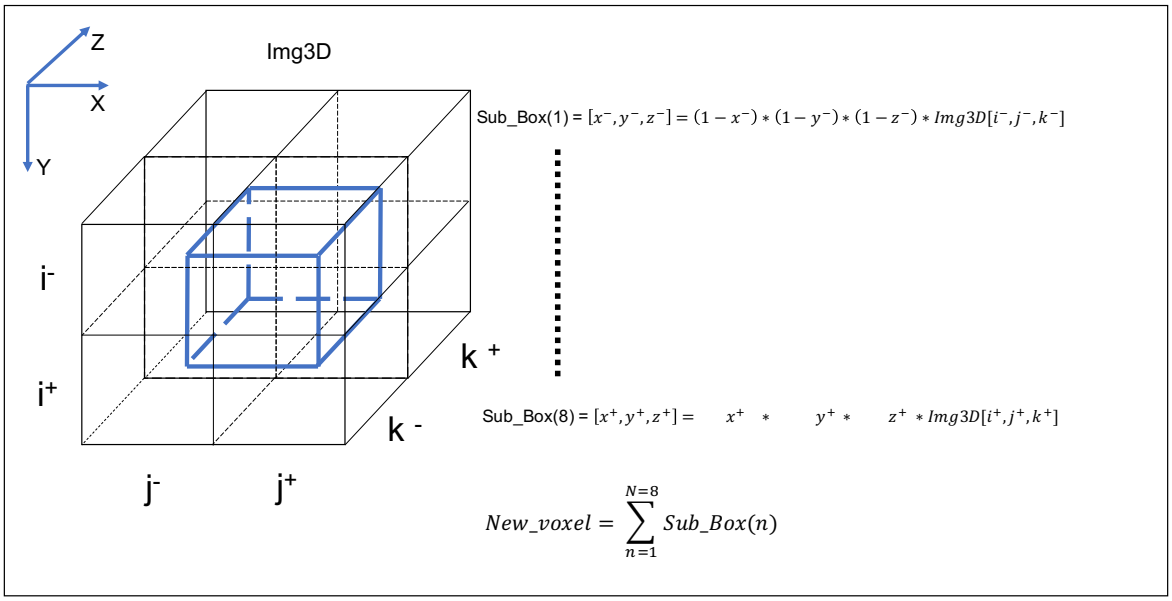

Figure 19: Illustration of how images are down-scaled to more manageable sizes. A sub-volume is calculated for each sub-box and multiplied to the voxel residing in, the summed up for the new voxel value. For each sub volume some information are preserved from the original through the down-scaling

This reduces the information inside 8 voxels to a combined mean of those into a new voxels. This process can be repeated for n number of dimension, strictly depending on the data handled. The relation between the number of cells being reduced to one and the number of dimension scale with a 2^n, as shown in 2D, 4 cells (2^2) are reduced to one and 8 voxels(2^3) to one in 3D and there on

out. With the high resolution data being ~[3200x3400x3400] voxels, the reduced data has the new scaling of ~[1600x1700x1700], ~[800x850x850], ~[400x425x425] for the $\frac{1}{2}$, $\frac{1}{4}$, $\frac{1}{8}$ and $\frac{1}{16}$ down scaled data respectively. The '~ are to account for different samples varying slightly in size. These scalings will be referred as 2x-, 4x-, 8x- and 16x-data from here on out.

Mentioned earlier, the samples in the synchrotron was scanned over multiple rounds, and to avoid losing information between sub-volumes some overlap was measured twice in subsequent measurements. Leaving discontinuities in the combined sample. This has to be straightened out before analysis can begin.

5.5 VOLUME MATCHING

The samples were too big to fit within the detector, so each sample was scanned over 4 subsequent measurements, giving 4 sub-volumes representing one sample. To avoid loss of data each sub-sample was scanned with some overlap between sections, creating areas scanned twice. To segment components of CT's properly, the internal components should be evaluated with respect to (w.r.t) continuity of the 3d structure.

This was fixed by using a custom made script that utilizes the 3d euclidean distances and smart indexing between in a given search region between two sub-volumes to estimate the best overlap. The search region is arbitrarily chosen and states how many layers in each sub-volume will be included in the search for an overlap. The process of smart indexing is the comparison of multiple indices/voxels at once. This process repeats three times to find the best overlap in the three subsequent overlap between the 4 sub-volumes. The result of the volume matching is illustrated in Figure 20.

13 unique samples was fed to the script, but due to broken and missing data, 5 of them were discarded and 8 samples of dimensions ~[3200,3400,3400] remained for further analysis.

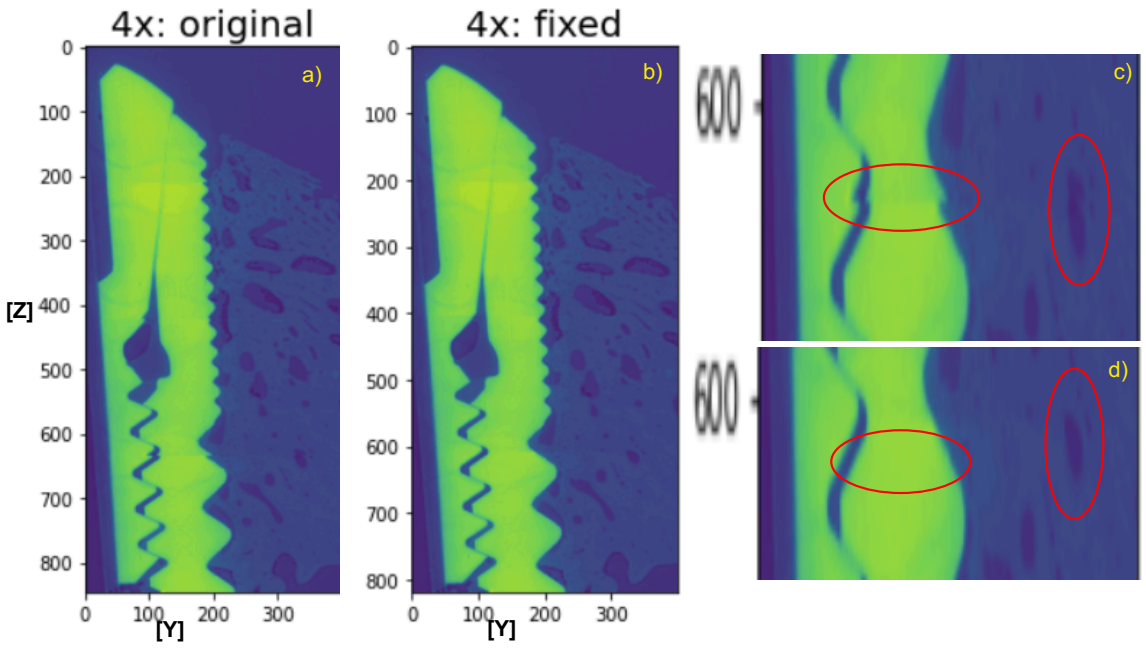

Figure 20: In Figure 20a is the sample without off set correction and Figure 20c shows a zoom in of the region with redundant sections. Figure 20b and d are the offset corrected

Figure 20 showed a slice of a CT, this was a slice of the X-axis, with the x-coordinate fixed and all Z and Y coordinates included. Most results will be illustrated through slices of the CT in Z-, Y- and X-slices.

Closer examination of the Z-slice in Figure 21 reveals redundant voxels outside the scope of the cylinder. These are to be removed to exclude information unrelated to the sample.

5.6 CREATING MASKS

The goal is to analyse the sample without any external noise. This can be removed with a mask. Masks in image analysis are a powerful tool for removing unwanted data from an image, focusing on the areas of interest. Creating a circular mask will encapsulate the the cylinder, and exclude remaining data.

The radius are chosen to be half the size of Y- or X-axis, the choice of this axis doesn't matter due to X and Y being identical in lengths. So radius (R) is chosen to be $X.size/2$. Now an array (arr)

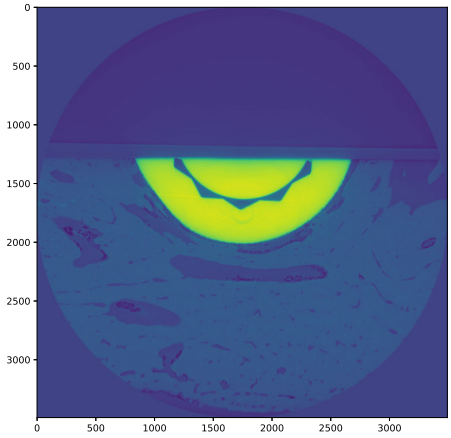

Figure 21: A Z-slice or a cross section of tomography-770

ranging from -R to R are created with step-size being $\frac{1}{X.size}$. The euclidean distance is calculated from the center(also being $X.size/2$) to all values of the square by broadcasting the array as such:

$$rs = \sqrt{arr[:, None]^2 + arr[None, :]^2} \tag{10}$$

Broadcasting is a feature where two arrays of size N and M will automatically try to match the other array's dimensions creating a NxM array. Creating an array of dimensions $[X.size, X.size]$ with values increasing the further away from the center. Now the mask will created with the command:

$$mask = rs \leq R \tag{11}$$

The command returns a Boolean (True or False) array with values being equal or less than R, accepted (returned as True) and all greater than R, rejected (returned False) yielding a mask shown in Figure 22b. The mask is applied to the data as shown in Figure 22, resulting in all voxels outside the cylinder are left empty.

Testing the mask, two histograms created from a small chunk with and without mask are made with numpy.histogram(), yielding two histograms seen in Figure 23.

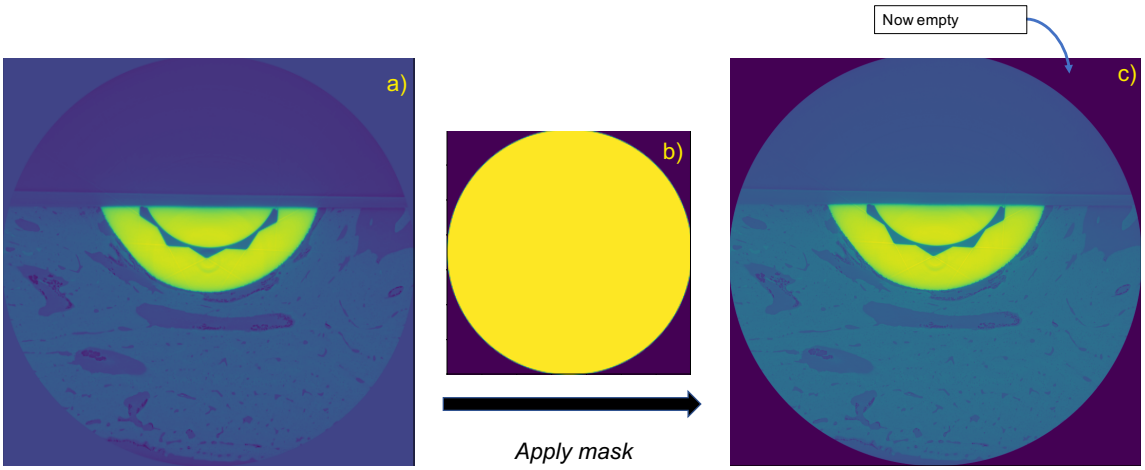

Figure 22: The mask in Figure 22b are applied on a. Returned Figure 22c, removing voxels with no information

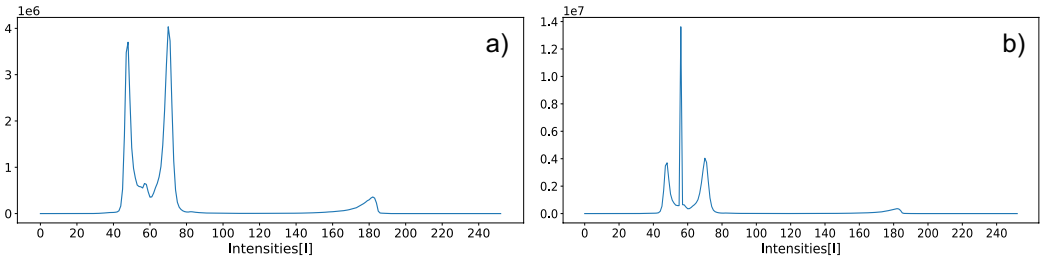

Figure 23: Figure 23a is with mask and Figure b are without mask. Seen very clearly in Fig b a prominent rises above all other. This peak is mostly absent in Fig a, which concludes applying a circular mask was beneficial.

Figure 23 showed that removing the voxels beyond the cylinder was a necessity. First step in the analysis is to convert the tomography into a histogram of voxels intensities. Accessing numerical information about the distribution of tomography intensities.

5.7 FITTING HISTOGRAMS

The aim is to use masked samples as a basis for probability estimation. The scope are to quantitatively estimate a type of tissue based on voxels intensities. Describing measured data with a distribution, issues a probability of an event to occur. A probabilistic approach never assume anything to be certain. High resolution samples contain over $3 * 10^9$ voxels forming solid basis for a statistic modelling. The

aim is to estimate different types of tissue from the voxels intensities. The CT will be converted into a histogram of voxels intensities and for each distinct peak, will a probability distribution be fitted to describe the data, in the giving voxels space. These probability distributions will assign a probability to a voxel of belonging to a certain class. A optimization algorithm will fit distributions to the data and the fitted distribution will add probabilities to voxels estimating the probability belonging to a class. Each distribution will then assign probabilities to the voxels of the CT. This constitutes a basis for classification of the CT's, where voxels always are evaluated with a probability instead of clustering them definitively.

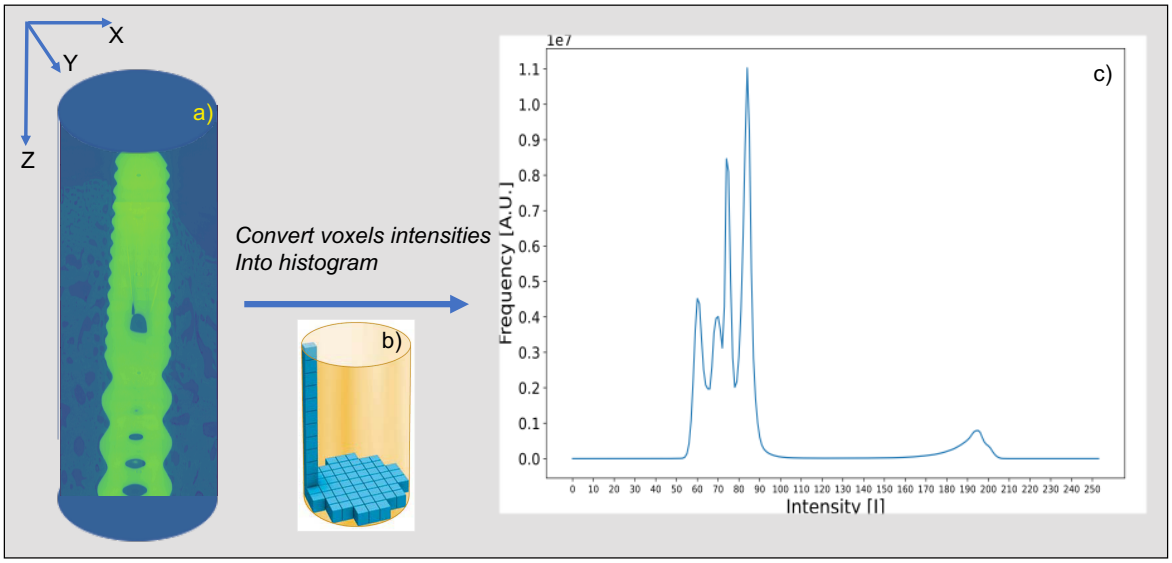

Figure 24: Figure 24a represent the CT's spatial dimension, while 24b illustrates individual voxels being counted. Figure 24c is the resulting histogram of intensities.

Describing the histogram are is Eq. 12 chosen.

$$P(C|I) = \sum_n a_n e^{-b_n(I-c_n)^{d_n}} \tag{12}$$

Eq. 12 is a Generalized Gaussian distribution (GGD). The GGD has similarities to the normal Gaussian distributions. Normal Gausssians' exponent are raised to the power of 2, while GGD exponent, referred to as d, resides between 1 and 2. The main difference are higher peak prominence of the distribution, and the parameter d narrows the initial spread, but has heavier tails, which accounts

better for voxels values, situated further from the center. Introducing a fitting model to describe these histograms with GGD's, a minimization function was chosen. The minimize function from the library Scipy.optimize, was chosen. Scipy.optimize.minimize(minimize) have the following rules for the input:

minimize(func, x0, args)

func(x0, args) $\longrightarrow$ float #must return a float

x0 = (n,) array #a one dimensional array of variables for the optimizer to fit

args = tuple #all extra input, e.g. raw data and constants

To match these condition a function called $"error_func"(ef)$ was developed based on Eq. 12. The final error function had the format shown in Eq. 13.

$$ef(x_0, args = (data, K)) = \sum(data - f_{init}(x_0))^2 + K\sum neg((data - f_{init}(x_0)))^2 \quad (13)$$

With $x_0 = [a_n, b_n, c_n, d_n]$ for the GGD. Parameters a and c were manually chosen as the max value for each peak and the index of the max value(argmax) respectively. b was chosen as the standard deviation for values in peak width. The d parameter was simply set to 2 initially, representing a normal Gauss. The values in x_0 are parameters. The minimizer will adjust the parameters to lower the total summation of ef. f_{init} being Eq. 12 taking x_0 as input. Data is the histogram from the sample. The $K * \sum neg((data - f_init(x_0)))^2$ term in Eq. 13 is a penalty function.

The minimizing function tries mimic the data as well as possible, regardless of the total sum of the distributions are greater than the data. Which is not desired here, the aim is to describe voxels values, nothing more. If the sum of distributions are greater than the data, then the model says there are more voxels than there actually is, which inaccurate. The penalty function here exerts a penalty to the minimizer, when distribution values becomes greater than the data. The constant K scales the penalty enforced. Effectively, ef are based on a least squares approach.

After running multiple iterations, the minimizer returns an estimate on the new parameters x_0. Inputting the new parameter into the f_{opt} yields the plots shown in Figure 25.

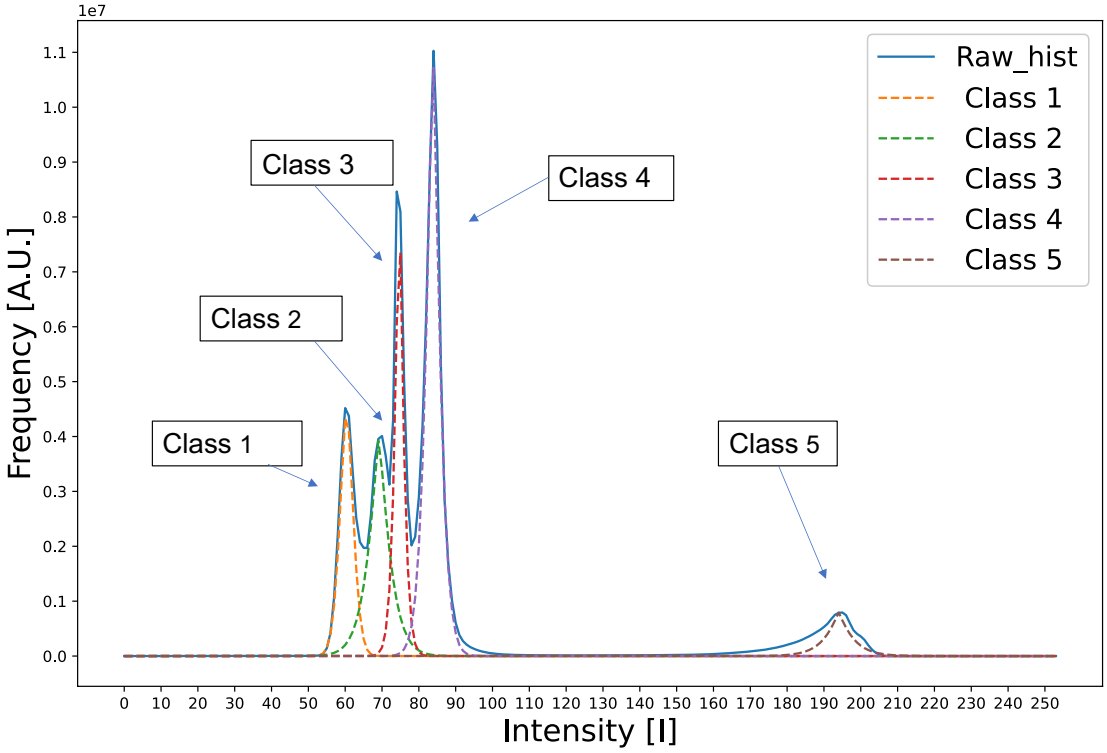

Figure 25: Histogram of voxels intensities and 5 fitted distributions. Each distribution are used to assign probabilities to voxels of the CT.

Each of the distributions represent a class, denoted as $P(I|C_n)$ where C_n are the class, depending on voxels intensities I. These minimized distributions will act as foundation for the segmentation of voxels values in CT's in the following section.

5.8 FIRST SEGMENTATION

The process of segmentation are a step in image analysis that assigns a label to a pixel, grouping it with other pixels of identical label. This way, different components in an image can be separated into different key features. Common image segmentation could be to separate pixels e.g. by their color. Here will the individual voxels be segmented with probability distributions, assigning voxels with

probabilities for the given class. 5 distribution has been fitted to the voxels intensity histogram, these distribution will segment the CT voxels by matching them individually. When the CT is matched, will the voxel values be converted in to probabilities of the distribution being matched. When the probabilities are assigned are the segmentation process is done. The segmentation will yield a CT for each distribution. These assigned probabilities will constitute how probable it is that one voxel belongs to a certain class. This will be the basis for estimating types of tissue in a CT.

Figure 26 illustrates how the process is carried out.

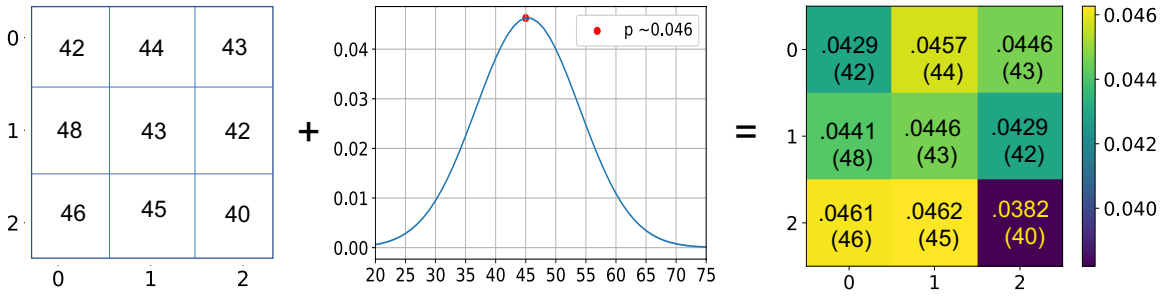

Figure 26: Simplified illustration of assigning probabilities by replacing values with the matching probability of the distribution. The 3x3 gray-scale image to the left are assigned new values by the distribution in the middle. To the right a new image with likelihood values instead of integers, The bracket shows the former value.

Now this process is scaled up, by applying the fitted distributions onto the CT. This returns an image for each distribution with corresponding probabilities. Each class denoted as C_n and their respective probability distribution as $P(C_n|I)$. This is how the segmentation process go. A Z-slice are chosen to illustrate the first segmentation seen in Figure 27.

Assessing the results from Figure 27 Many key features are visible for interpretation. Reflections effect in Figure a, b, c and d above the implant would imply internal scattering close to the implant. All voxels beneath the implant all low probability, while the raw data shows voxels beneath the implant. The results imply the presence of refraction effects around the implant that induces smearing with no distribution able to describe this region properly.

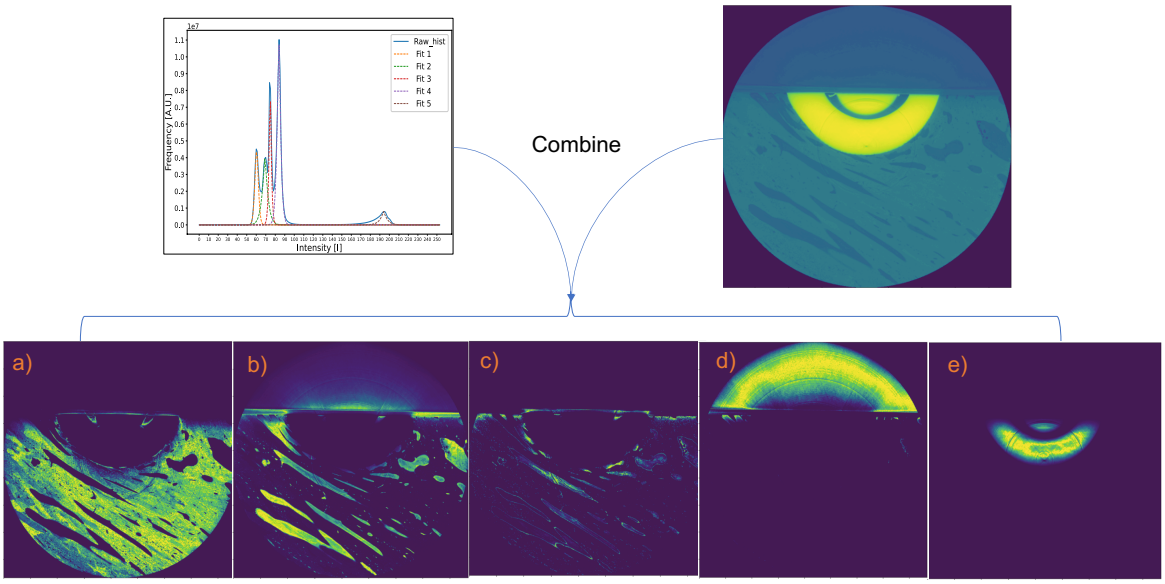

Figure 27: Five different classes(C_n)) assigned by a probability distribution ($P(C_n|I)$) are illuminated in Figure 27a through e. The bright yellow areas are the high probability voxels, while the darker blue are voxels with lower class probability. The example is a Z-slice of the a tomography

These refraction effects create a problematic scenario for classifying voxels close to the implant. To solve this are more information needed to describe these refraction effects. The CT's are three dimensional, so depending the segmentation on spatial parameter could reveal how the refraction affects local sub volumes could further clarify the severity of the refraction induced smear. The new probability distribution are now given by$P(C_n|I,Y)$ instead of $P(I)$.

5.9 SPATIAL DEPENDANT PROBABILITY

The CT's acquired from the bone specimens are made up of a large number of voxels. The individual voxel contain two distinct types of information, intensity and spatial coordinates given in 3 dimensions Z,Y and X. Systematic reflections around the implant caused bleaching/bleeding effects to voxels values in the proximity of the implant. The distributions used for segmentation was based only the intensity of the voxels. Given voxels contain two types of information, why not base the segmentation on a combination of information types? To better asses the spatial effects of reflection, will the

distributions for segmentation be based on a mix of intensity and spatial parameters, yielding a probability distribution denoted as $P(C_n|I,Y)$, with being an arbitrary choice here. Implementation are introduced by converting individual slices of the CT's into histograms. These histograms will be stacked in an array, where each row in the array represents a slice of the CT. Each row will later be used will be fitted to a series of distributions, allowing for a layer-wise segmentation.

All data analysis from here on will be on the 4x data [820,850,850], since multiple layers are to be accessed repeatedly, effectively speeding up computation with lower resolution data. Given the architecture of the tomographies, the Y-axis are chosen as the spatial coordinate to expand the probability model with more than just intensity. Looking at Figure 27, Y-axis are the direction from top to bottom of the image.

The Y-axis of CT's voxel intensities will be converted to histograms, slice-wise, meaning, every slice in the Y-direction is converted into a histogram and stacked on top of each other in an array. Effectively creating an image(2d-histogram) with the Y-axis are the depth of tomography in the Y-direction and X-axis being the voxels-intensity as illustrated in Figure 28.

Comparing the Y-histogram with a Z-slice seen in Figure 27 shows the abrupt change in distinct lines happens at the interface of implant and bone-matrix. Distinct lines following certain intensities along the Y-axis in the 2d histogram(Y-histogram) shows, a clearer separation between these lines of intensities, than the peaks from the collapsed intensity histogram. A new problem emerge with this approach. A single histogram needs values(guesses to be optimized by the minimizer) for x_0, these could be chosen manually. Now 3000+ histograms are generated(for high resolution) and each of them needs initial guesses for x_0. x_0 scales with 4 for each peak(one each for a,b,c,d in Eq. 12). Counting up to 5 distinct peaks pr. layer results in $4x5x3000 = 60000$ parameters to be chosen and minimized afterwards. This process would takes years if values were chosen manually for each parameter. Enabling this approach, a function, which automatically find peak parameters and fits distribution model to data are to be made.

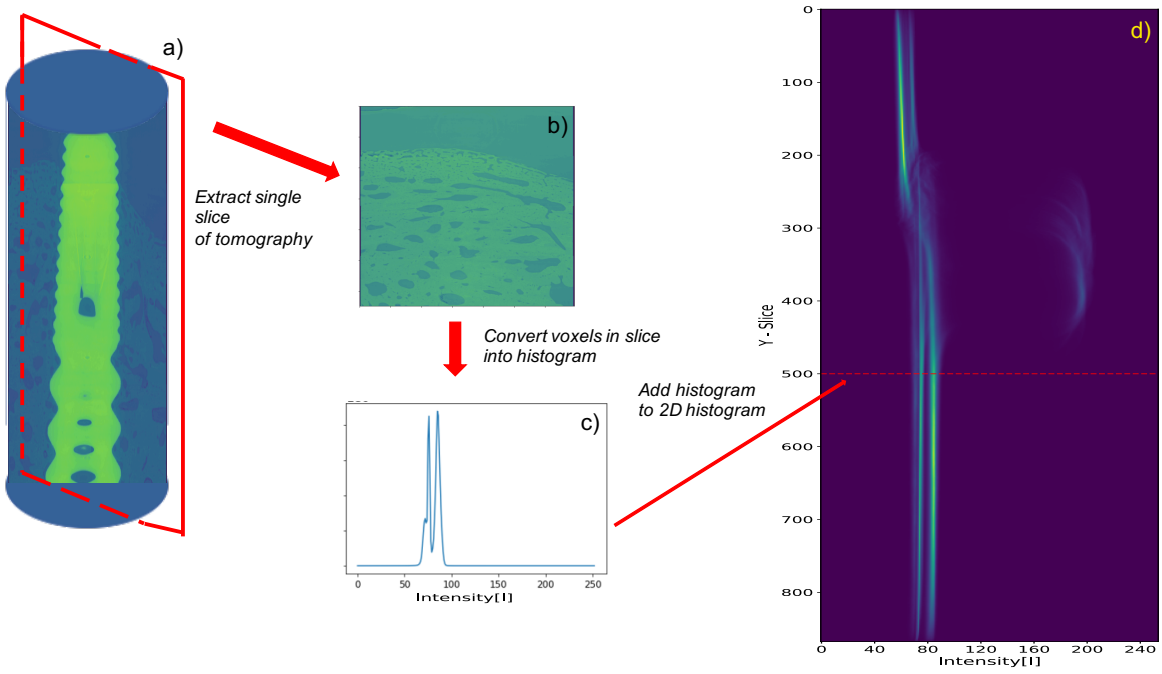

Figure 28: Through Figure 28a to d illustrate the process of generating a 2d-histogram. In a) a Y-slice is extracted. The Y-slice are shown in Fig b. The voxels values are collapsed to a histogram of intensities. The histogram is then place in a 2d-array with each row in the array representing a histogram from each layer/slice in the Y-direction, creating the 2d histogram

5.10 AUTOMATING FITTING PROCESS

Given the enormous amounts of data and the fact that this might act as baseline for fast analysis of bone tomographies, it would be wise to create an automated process for minimizing large numbers of distributions to data. A function will developed to extract values for probability distributions from the shapes of the histograms. The function will iterate through the histograms situated in the rows of the 2d-histogram, generating initial guesses for parameters of each peak in the histogram. These guessed parameters will be minimized to fit the data. This process repeats for each row until all rows/layers of the CT has been minimized to a distribution. The development of a function will be explained in the coming paragraph.

The minimizer works by comparing raw-data with f_{init}, which is based on parameters $[a, b, c, d]$. Starting point would be finding peak positions, since a and c draw their initial values from the peak-positions. The Scipy library scipy.signals include many effective tools for extracting key features from data sets. First the function $find\_peaks$ was tested, but even the smallest local maxima in the data yielded a peak, making the function locating to many peaks. After extensive testing, was the problem solved by excluding insignificant peaks by setting a height requirement for the peaks based on the mean height of the collective peaks. The result of the $find\_peaks$ function with and without height requirement are shown in Figure 29.

A robust solution for finding b proved to be difficult, until the function $peak\_widths$ was discovered. $peak\_widths$ returns the indices(position) of tails per peak. Feeding indices for peaks found via $find\_peaks$ with height-filter into $peak\_widths$ yielded the widths. The standard deviation between tails of the peaks laid foundation for the initial values of b. d remained at 2, so the starting point would be a normal Gaussian distribution. These collective steps adds up to the function called $Initial\_trial$. $Initial\_trial$ takes a histogram as lone input and outputs values for the fitting parameters [a,b,c,d] in an (n,)-array, which is the same format the minimizer accepts. The output are placed in the minimizer

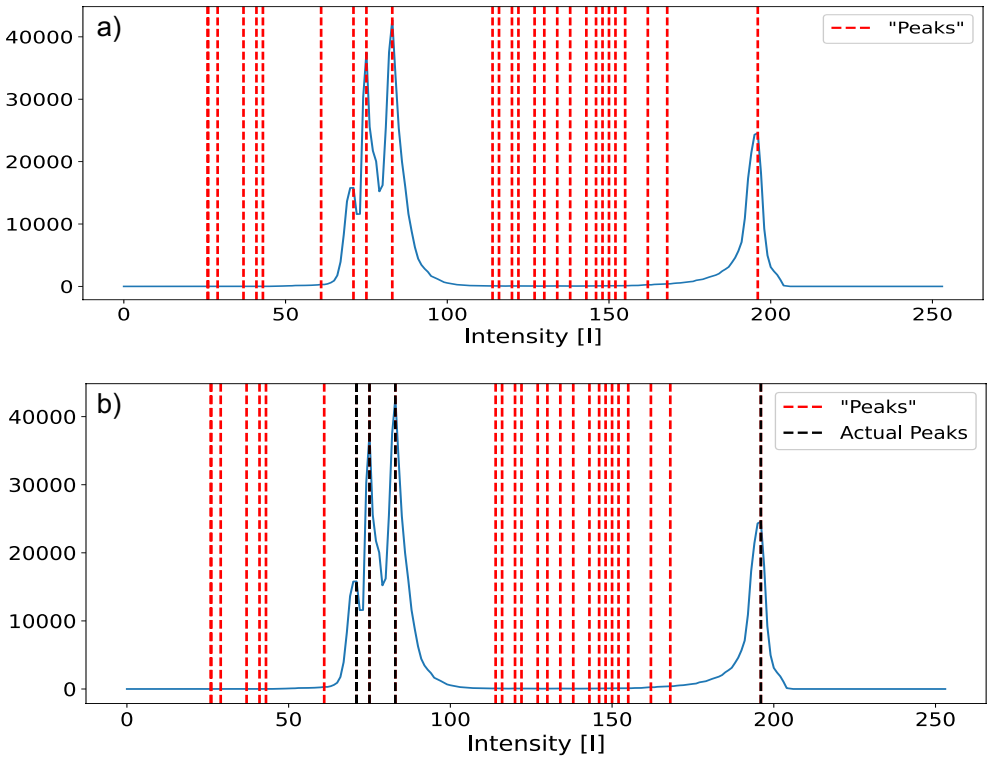

Figure 29: The scipys Find_peaks function. Figure a. shows all signals registered as peaks. A peak height limit was introduced in Figure b. identifying desired peaks.

and it fits the parameters so their respective distributions fits the histograms. This process is repeated for each layer of Y, resulting in a final 2d-fit of the Y-histogram.

Minimizers are rarely perfect, so the next section will access how well the auto-fitter performs on multiple layers and comment on the role the penalty functions plays.

5.11 TESTING AUTO-FITTER

Processing large amounts of data and doing tons of arithmetic operations combined with an optimization function can be erroneous. Depending on the robustness of the function being minimized. Assessing the robustness of the minimization function will be done in this section. Checking if the auto-fitter match distributions to the data well enough to be pursued as an approach or if it should be reevaluated.

Comparing layers, the fitted distributions are much more smooth due to the distributions being continuous, but describes the data well. Two simple examples in Figure 30 illustrate the differences between fitted distributions and raw data histogram.

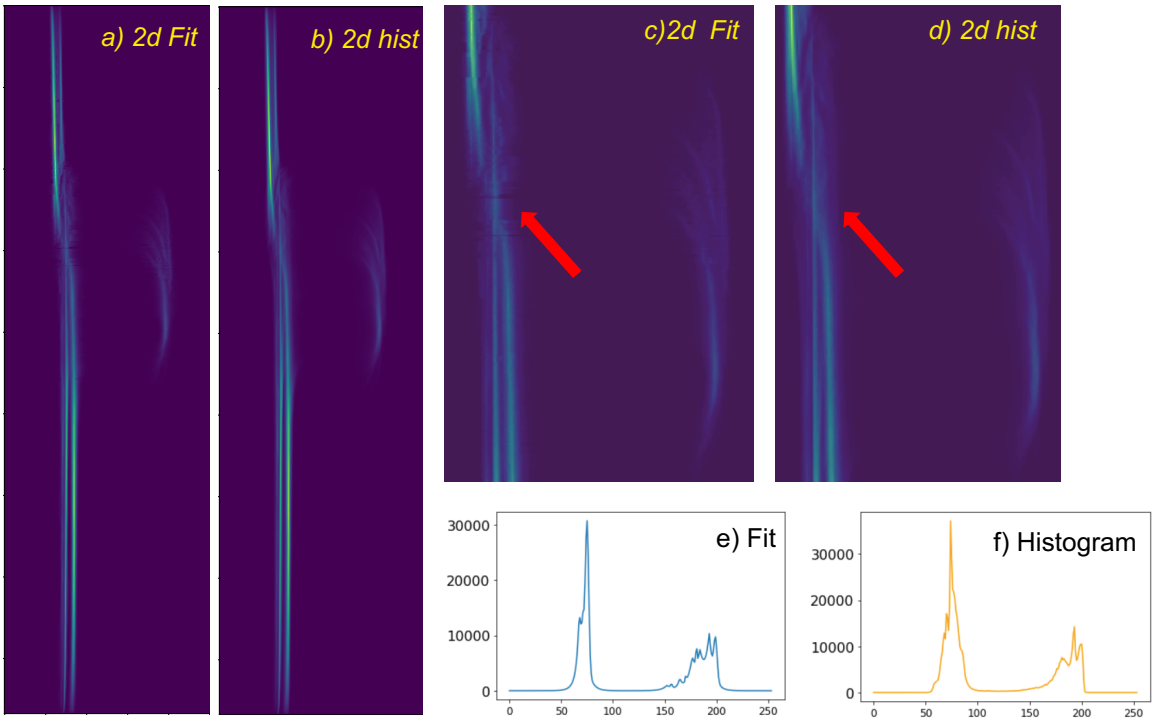

Figure 30: Fig a. and b. shows the fit and histogram respectively. c. and d. are a zoom-in of the worst regions.

Brief comments on the penalty function. It would appear when the auto-fitters penalty constant K is close to 0, the fitted distributions are all over the place, wide distributions, peaks shifted away from origin, nothing favorable being too close to 0. On the other hand, if the constant is set too high, the range of the auto-fitter appeared to be limited. Even the slightest tweak punishes the fitter, not allowing it iterate through the initial local minima. The constant was empirically found to perform best at the range $3 - 5$. This range kept peaks fairly in place and shapes similar to the histograms.

The auto-fitter performs well. Next issue is pairing the individual fitted distributions with their respective Y-slices.

5.12 SPATIAL SEGMENTATION

Reflection effects cause bleaching/ bleeding around the implant, the former segmentation method said nothing about how it affects certain sub areas of the tomography specifically. To better explain these local reflection effect are layers of the CT's evaluated individually with distributions based on intensity and spatial parameter Y given by $P(C_n|I,y)$. An automatc fitting focus has been developed to aid this process. The distributions for $P(C_n|I,y)$ has been fitted with the minimizer. Next step is to match the fitted distributions with respective layers to perform the first spatial segmentation.

Same principle as when extracting slice to make histograms, but now each set of distributions must be applied to their respective layer of the tomography. A fraction of the data(full CT) are loaded (4x data) into memory at once. Chunks are cut in the Z-axis, because in python are rows extracted faster than columns and rows are axis 0 aka Z for these data files. Data loaded with respect to Z are faster. 4x data are sliced in 10 separate chunks, when segmenting, meaning the dimension of each chunk loaded will be [Z.size/10,Y.size, X.size], so [80,850,850] for 4x scaled data. The Y-axis is of interest, each layer of Y in the chunk, will be matched with the same layer in the 2d y-fit. The fitted distributions are applied with the same principle as previous segmentation section by indexing the image(here Y-slice) into the fit as so $fit[n, image(Y-slice)]$. Resulting in a whole chunk being segmented slice wise, until the entire chunk has been segmented. The segmented chunk(an array of size [80,850,850]) is the added to an array of full size [800,850,850]. A new chunk is loaded instead of the previous one, replacing it and therefore not taking up more memory. This process repeats until all chunks of the entire tomography has been segmented. All chunks segmented are saved with the h5py module, which compress and store data to a written file, that is how the entire CT are saved into one file from the segmentation.

When the process of segmentation are done, the new results will be compared with old results from the former method based on $P(I)$, to access how the implant reflection affects the the different class when they are estimated with $P(C|I,y)$.

5.13 COMPARING SEGMENTATION METHODS

High resolution CT contain over 3 billion voxels, and that allows for many permutations data in many different sub sets, so combining voxels into sub-sets of Y-slices may reveal information about the reflection effects around the implant. If any relation between the reflection effect and the spatial components are present, will it allow for a correction of the CT's data which could improve the segmentation significantly.

Below in Figure 31 the results from the initial segmentation - $P(C|I)$ are compared to the new result from the segmentation $P(C|I,y)$.

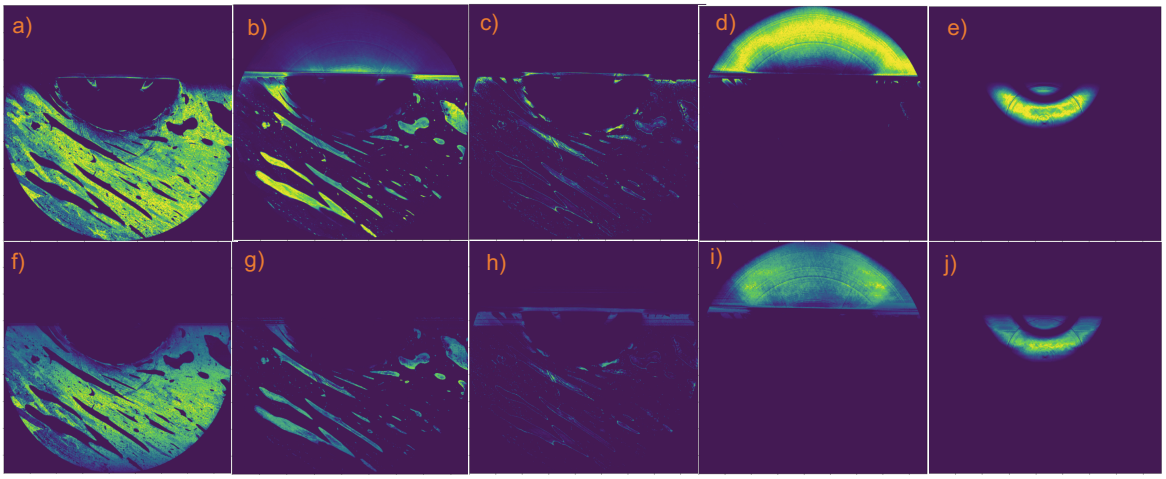

Figure 31: Figure a. through e. are from $P(C_n|I)$ while f through j are from the $P(C_n|I,y)$ segmentation

The interface between implant in Figure 31 a and b have been shifted to Figure 31 h and i, this clear separation of reflection imply the upper reflection effects with respect to Y can be removed entirely avoiding this part of the reflection. The bleaching under implant have to be corrected in some way, with the outer areas of the sample have lower probability.

The implant in it self, adds no important information to the analysis. Accelerating computations are the implant to be removed, this will especially be beneficial for high resolution data.

5.14 REMOVING THE IMPLANT

Segmenting CT's are a computer costly process and takes a lot of time to process. The process works by matching distributions from each class $P(C_n|I,y)$ with all voxels of the CT. The larger n are the longer time it takes to complete. Multiple segmentation have given a clear picture of the different classes, and the implant doesn't contribute with any interesting information. Bone-matrix are the interesting part and the implant intensities are far from the bone intensities. The implant voxels has much higher intensities, compared to other classes. This is due the implant being made of titanium, which have a higher atomic number, substantiating the absorption factor scaling with Z^4.

Implant intensities can be removed with a simple thresh-holding, since there is no overlap between implant histogram and other classes histogram. The removal is illustrated in Figure 32.

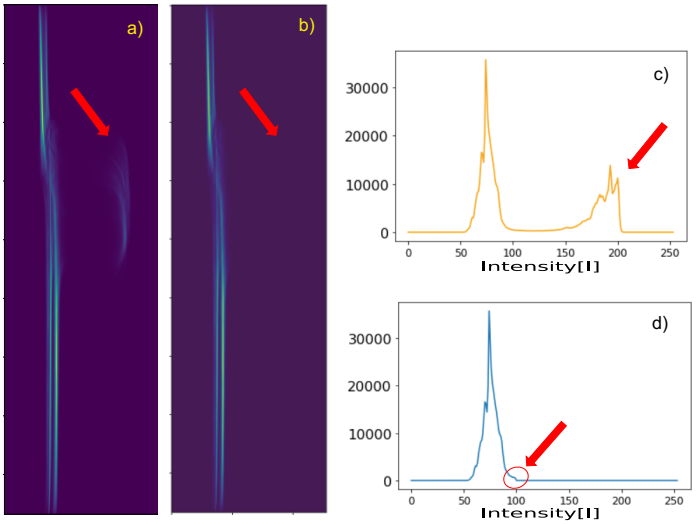

Figure 32: The visible chances when the implant is removed by thresh-holding

The removal of the implant voxels will speed up the calculations and focusing processing power on other classes.

Many areas in the Y-segmentation had lower probabilities than the previous segmentation, implying some voxels are not as well presented in the Y-slices. Other spatial specific coordinates might hide

information in the loss of probability in the outer regions of the CT. These may also reveal how bleaching around the implant surface might be corrected.

5.15 EXPANDING ANALYSIS TO Z, X AND RADIAL DIMENSIONS

CT's have been segmented in the Y-direction, but other dimension have not been explored yet. Expanding the statistical and probabilistic basis by including the Z, X and radial component could enhance the probabilistic effect by triangulating different models to enhance precision. Radial, means circle patterns radiating out from the center, so isotropic distance from the center in discrete steps. The goal is to implement 3 new probability distributions based the other spatial components $P(C_n|I,z)$, $P(C_n|I,x)$ and $P(C_n|I,radial)$. These could provide additional information about different spatial regions in CT's, which could propose possible solutions for reflection induced, bleaching issue.

Creating histograms in Z- and X-direction was done similarly as Y-histogramming. The CT has 3 dimensions Z,Y and X and as an array are denoted as CT[Z,Y,X] i.e. axis 0(Z),axis 1(Y) and axis 2(X). Creating histograms is done by $CT[n,:,:] \longrightarrow Z-histogram[n]$ for Z and $CT[:,:,n] \longrightarrow X-histogram[n]$ for X.

Radial-histogramming was done differently, each histogram will be made of a mixture of X,Y coordinates forming a circle pattern, radiating from the center and outwards the cylinder. To calculate the index values for the circle pattern, was X represented with a cosine-function, while Y was a sine-function giving them the format: $x[n] = r * cos(\theta)$ and $y[n] = r * sin(\theta)$. r is the radius in the n'th layer in the radial transformation, with ranges for r, n and θ being defined as $r = [1, X.size/2]$, $n = [0, X.size/2-1]$ and $\theta = [0, 2\pi]$ with the starting point in $X.size/2$ i.e. the center of the cylinder. r starts at 1, because a circles circumference with radius 0 is 0, so naturally will it start at 1. Python are zero indexing, hence n starting in 0. The θ interval are chosen because 2 radians(π) are a full revolution, necessary to include full circle segments. Figure 33 explains how the radial histogram iterates.

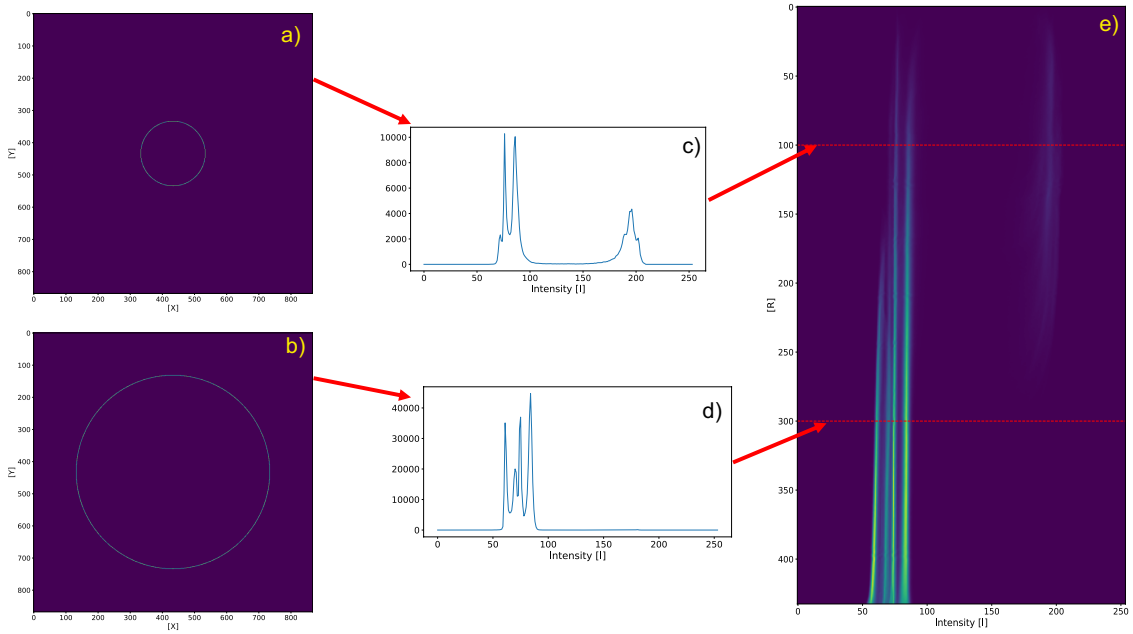

Figure 33: Figure a. and b. represent indices extracted for voxels to histogram conversion. This is a cross section of the mask but in 3d it's a hollow cylinder, traversing through all Z coordinates extracting all voxels indices matching the hollow cylinder. c. and d. are the resulting intensity histograms from a. and b. respectively. Figure e) is the final 2d-histogram and the red-dashed lines indicate the area where c. and d. are located.

After processing all the 2d-histograms for Z, X and rad respectively, they came out as shown in Figure 34, some new features emerged from these new histograms. Z had some lines that abruptly cut off the and bends to one direction. The X histogram appear to be homogeneous through out the whole sample, with small bend in lines in the upper and lower parts of the histogram as intensities decline at the edges of the sample. The radial-histogram show a systematic pattern, with all lines sloping off slowly towards lower intensities. This could be evidence for beam hardening. Rad starts from the center of the sample and moves iso-tropically outwards, so intensities becomes lower the further away from the center and has higher spread. This might be the result of high energy photons only are able to penetrate the thickest part of the sample, yielding a lower spread of intensities in the middle.

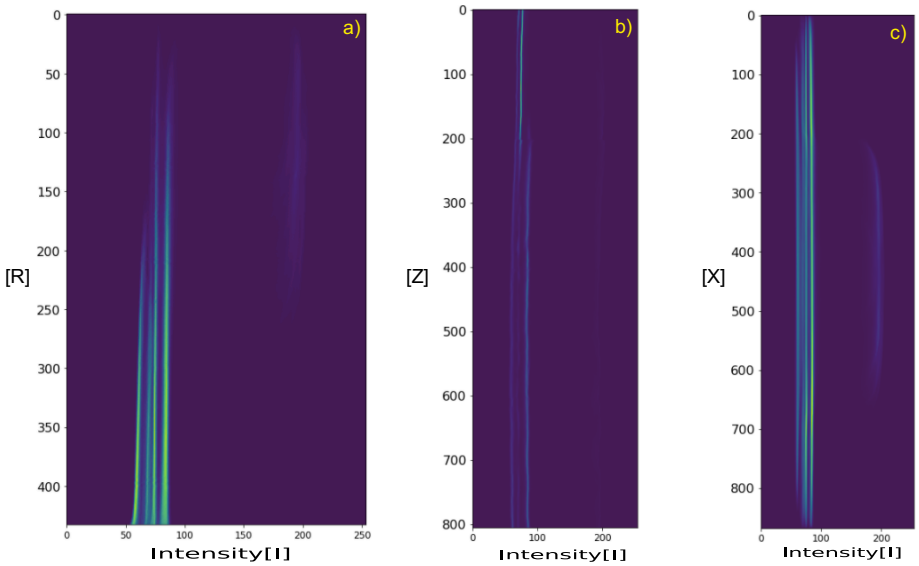

Figure 34: Figure 34 a,b and c are the resulting 2d-histograms of voxels intensities in radiating from the center, Z- and X-axis respectively.

The created histograms, are fitted and segmented to test, if the hypothesis of, distributions depending on other spatial information than Y, might hide more information of the reflection problem along implant interfaces.

Looking at figure 35 can it be seen that reflection around the implant are classified as bone, while the y segmentation in that slice are not as affected. Earlier mentioned the upper layer in the y-direction consisted only of resin and the majority of reflective voxels are on the upper part, again w.r.t. to y. The resin poses no interest in this analysis, it might improve analysis if it was to be removed entirely with the implant.

5.16 UPGRADING THE IMPLANT REMOVAL

Looking at the data makes it clear that an outline of the implant remaing. But it is out in the region of resin. The resin were added to the bone to give the bone a more symmetric shape, when the scanning. Post measuring are the resin of no use. The objective is tom remove the resin above the implant, since it doesn't add to the analysis. Accessing this issue will be done by creating a function that removes

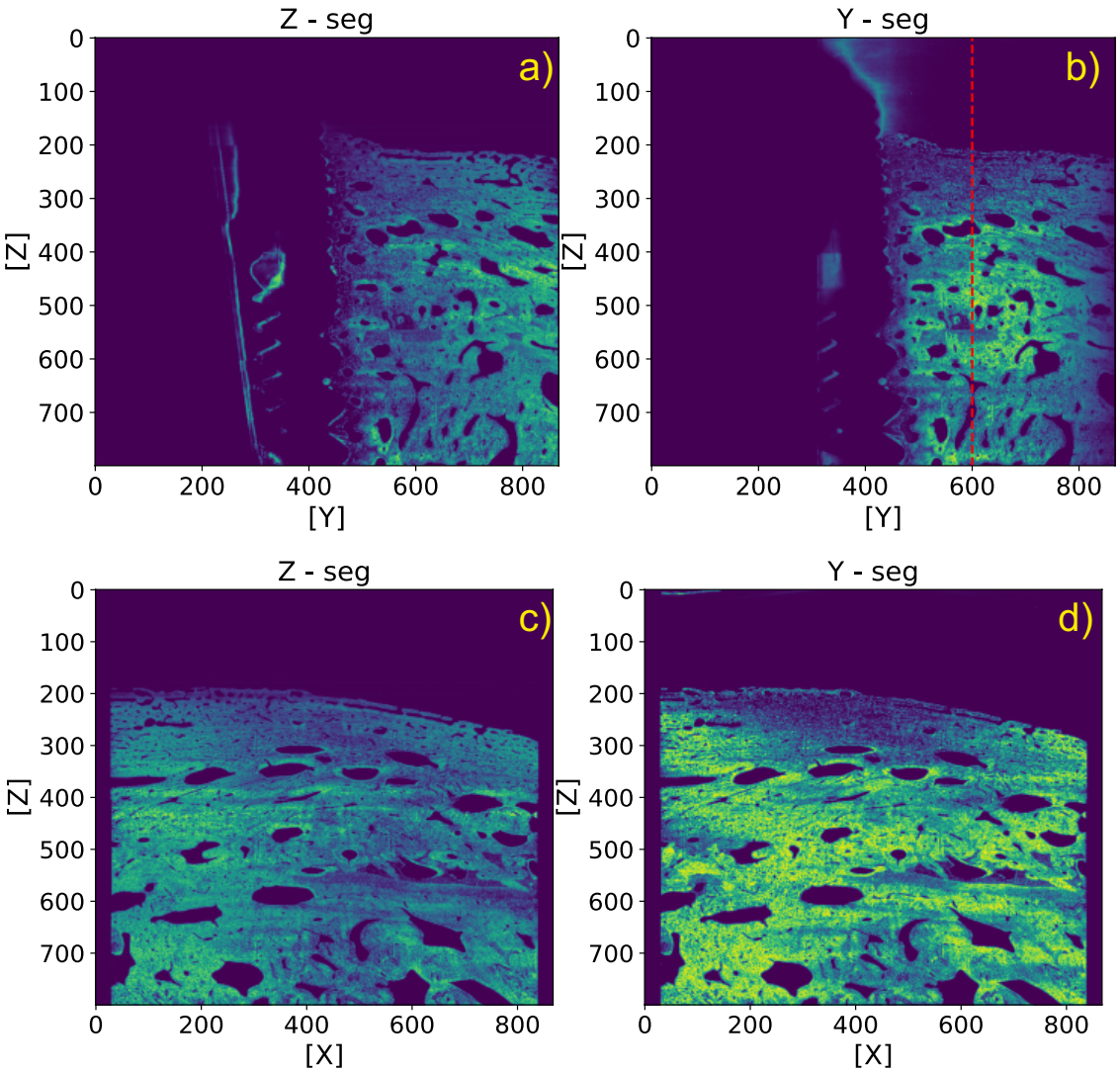

Figure 35: a and b are a X-slice of the segmentation w.r.t. Z and Y respectively. The leftover mirror effects around the void left by the implant are recognized as bone by the model, indicating that reflection can obstruct the signal. The red-dashed line in Figure b outlines an area of high probability within the Y-segmentation. This specific layer(layer 600 in Y) are plotted in fig c and d. The general high probability in d could be the lack of implant in this subset of data, while all layers in Z are affected by the implant since the implant is present in every Z-slice.

the implant and all of the resin in one sweep. The approach are the initially the same as the previous attempt to remove the implant by thresh-holding, instead this time, additional steps are added. The steps will be evaluated in the following paragraph.

Thresh-holding: All voxels values below 100 are removed, 36b. Thereafter are all values above the implant marked, only leaving a small unmasked area around the implant36c. These remaining cavities are closes with Scipys image processing library $NDimage$ using the function $binary\_fill\_holes$,36d. The mask is then inverted, which means all voxels that are True(Yellow), become False(purple), vice versa. Leaving the desired mask for implant and resin removal. A step by step process are illustrated in Figure 36.

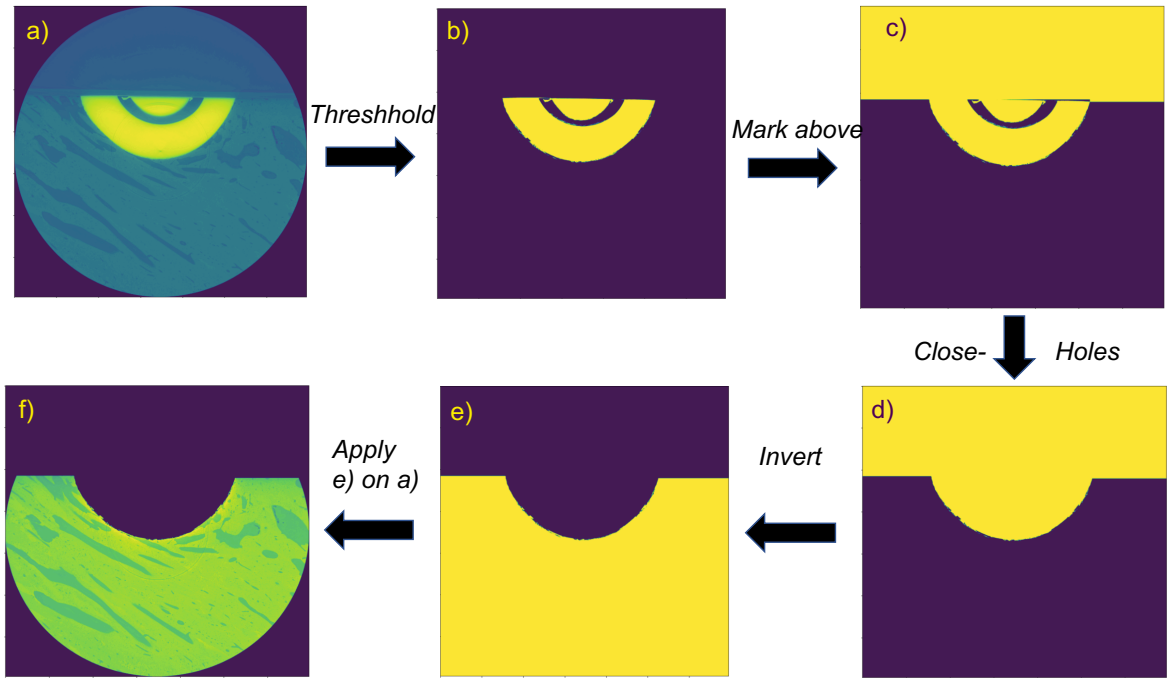

Figure 36: Walk through of the process of removing implant and above resin. a $\longrightarrow$ b: All voxels with values less than 100 are removed. b $\longrightarrow$ c: Area above implant are marked True. c $\longrightarrow$ d: Scipy.binary$_{f}ill_{h}olesareused.d$ $\longrightarrow$ e: The mask is inverted. e $\longrightarrow$ f: The mask is applied on the raw data.

The four spatial 2d histograms are reloaded, fitted to distributions and segmented to access changes induced by the improved implant removal. When ”reloading” is mentioned, it simply means to load histograms from the samples, but now with a new mask applied to CT. The histograms are visible below in Figure 37.

Histograms are much more separated, and signal are more clear. The resin are assumed to have been removed effective, erasing some the reflections from the implant, partially solving the problem.

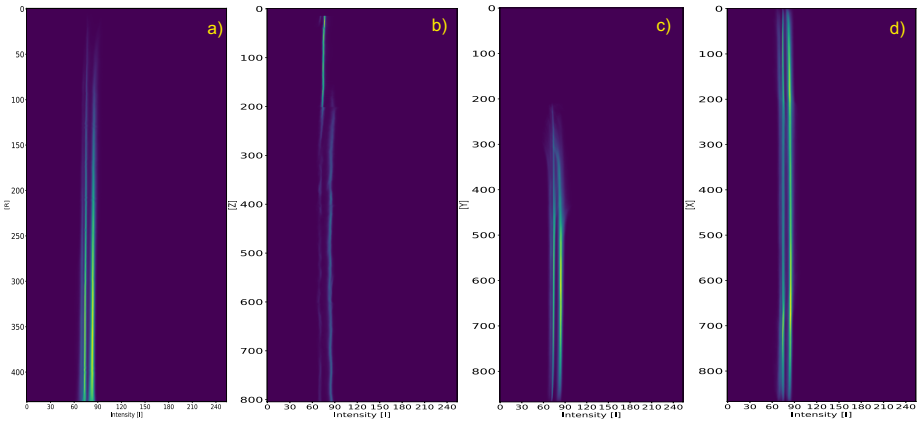

Figure 37: Histograms of Rad, Z, Y and X with the new implant mask respectively.

Looking at X-slices of the new Y-segmentation illustrated in Figure 38 shows some leftover resin are situated on the upper side of bone material. As Figure 37 shows, are the two classes seperated by the resin, by obstructing the cavity signal from within the bone. Additional resin on the upper part are to be removed as well in the following section.

5.17 RESIN MASK

Looking at the new segmentation in Figure 38, did it become apparent that some resin remains. The resin mostly affects the Y-, X- and radial-segmentation since, all layers of Z are included in their respective layers. Hence, the Z-histogram has a clear line(representing a class) that very visible until the bone-matrix line and would then fade. This could indicate this might be the leftover resin. This must be removed before the remaining classes can be segmented. The line was the extracted separately(Figure 39) and a bit-mask was created.

Bit-masks are an array with the exact same dimensions as the CT, but in binary format. They are masks, but saved as a separate file, to avoid repeating unnecessary calculations. The improved implant-mask, was a function, applied every time the CT's were converted to histograms. Permanent bit-masks were also made for the improved implant mask.

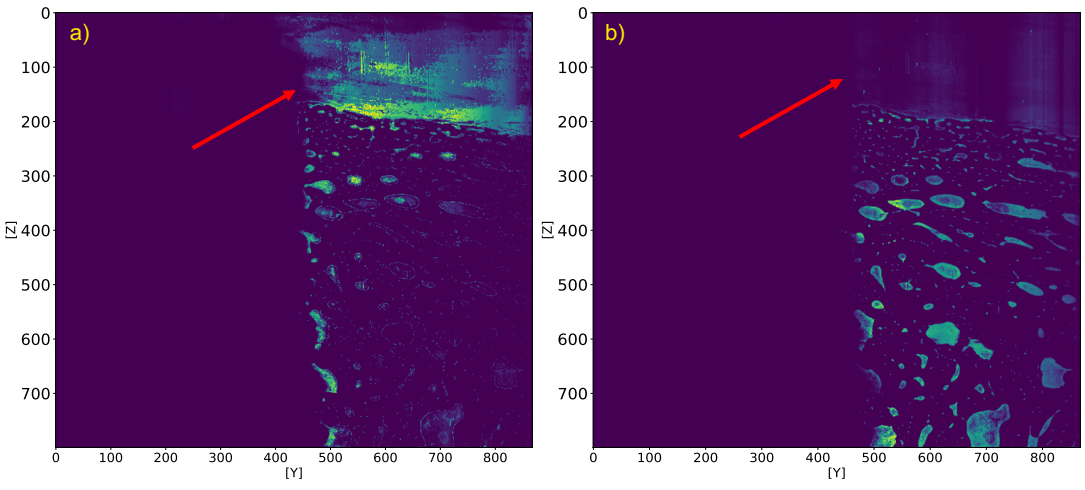

Figure 38: The segmentation represents the two classes with lower intensities than bone, as far left lines in Figure 37a, b, c and d. In a and b are many of the same areas are lighted up to different degree. The top section, pointed by the red arrow, will be removed.

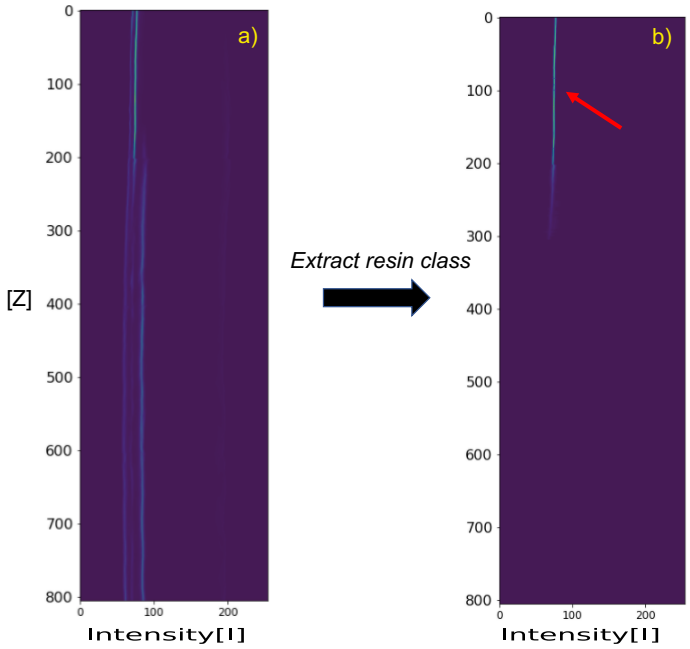

Figure 39: The resin class from Figure 39a, are extracted and stand alone in Figure 39b. This will be used to create a bit-mask

The bit-mask was created and the CT's were reloaded. The histograms looked really good, with only 2 classes remaining. With the bit-mask being introduced, was the final segmentation of high resolution

data almost ready. A few steps remained to be fixed before the segmentation is fully automatic. One of them is the auto-fitter, it had a quirk, needed to be tweaked.

5.18 ADDING BOUNDS TO AUTO-FITTER

The auto-fitter would at time merged peaks into one peak, meaning two different classes, would be identical. Trying to fix the problem, drove the attention back to the documentation of the scipy.optimize.minimize function. The documentation stated that bounds could be included into the minimize function. Effectively giving each parameter a limited range, so they wouldn't exceed or go below a given value. A new function was made, to limit the parameters space automatically. The limits were chosen to confine shapes of the distributions, given the knowledge of the shapes. For a, b, c and d from way back in Eq. 12 will all have bounds added, limiting the minimizers option. Choosing bounds for a variable, an upper and lower bounds must be provided to give the interval, that the minimizer are allowed to work in. Bounds for a was chosen to be $a = [0.8 * a_{init}, a_{init}]$. a is the amplitude of the GGD and this range was chosen, to avoid peaks becoming taller than the data, but nor too low, so other peaks with higher spread, would compensate for the height. Eq. 12 is a sum of distributions, so smaller peaks can become taller, if neighbouring peaks has high spread. b was set to $b = [0.2, 5]$, an arbitrary choice simply making sure distributions become to wide nor too narrow. c dictates the position of the distribution and if its moved to much, it might overlap with other peaks or completely merge. c was set to $c = [c_{init} - FWHM/2, c_{init} + FWHM/2]$ this forces c to stay inside it's own width. FWHM are Full width at half maximum, which is the the width of the distributions half way up. d the bounds was set to $d = [1, 2]$. For a GGD to remain a GGD the range had to be between 1 and 2. Most fitting distributions had $d \approx 1.66$, meaning it's close to a normal Gauss, but not quite.

These upgrades ultimately sped up the calculations and improved the fitted distributions. Not a major upgrade in precision, but alas it was better and more robust than before. With the last fix of the

auto-fitter function, only one more process was left to be automated. Before the entire segmentation could run in one go. The lines of the fitted-distributions were manually sorted into classes by designing a new triple for loop for each new histogram, then dividing into different classes. This took time to design every and was tenuous and ineffective. So as an final act of ingenuity, a ridge-detection function needed to be made, for detecting ridges in 2d-histograms, referred as lines up until now.

5.19 RIDGE-DETECTION - AUTOMATIC LABELING

Up until now, were the fitted distributions and their respective parameters stored in python lists. When the time for segmentation was right, the specific distributions for each class was extracted from the list manually. This was done by designing a quick for loop dividing classes, by matching distributions with a mean for all layers, separating them roughly into respective classes. The sorting was never perfect so in end, the classes was sorted slightly incorrect and had to moved in between classes once more. The objective is to separate the lines in the 2d-fitted distributions into individual arrays containing only one class each. Multiple image analysis tools offered for python was tested on the fitted distributions, but with little success.

In the end, a ridges detection function that separated classes effectively was made. The function progresses as such: An empty array of same dimensions as was created. At the positions of the c-parameters i.e. the mean intensity of each distribution, was a 1 was added to the array, creating a binary array of peak positions shown in Figure 40a. This binary array was then treated with first one iteration of erosion with a 3x3 kernel with ones only in the second column. The same kernel was used for dilation a few iteration afterwards. The library used was $open\_cv$. This first removed several smaller peaks with no consistent connection to other peaks, there after the dilation reconnected the severed connection between the connections with more continuity. These final conjugated segments are assumed to be classes due to similar peak positions throughout the layers, meaning approximately the same centering distributions. The steps of the process are illustrated in 40.

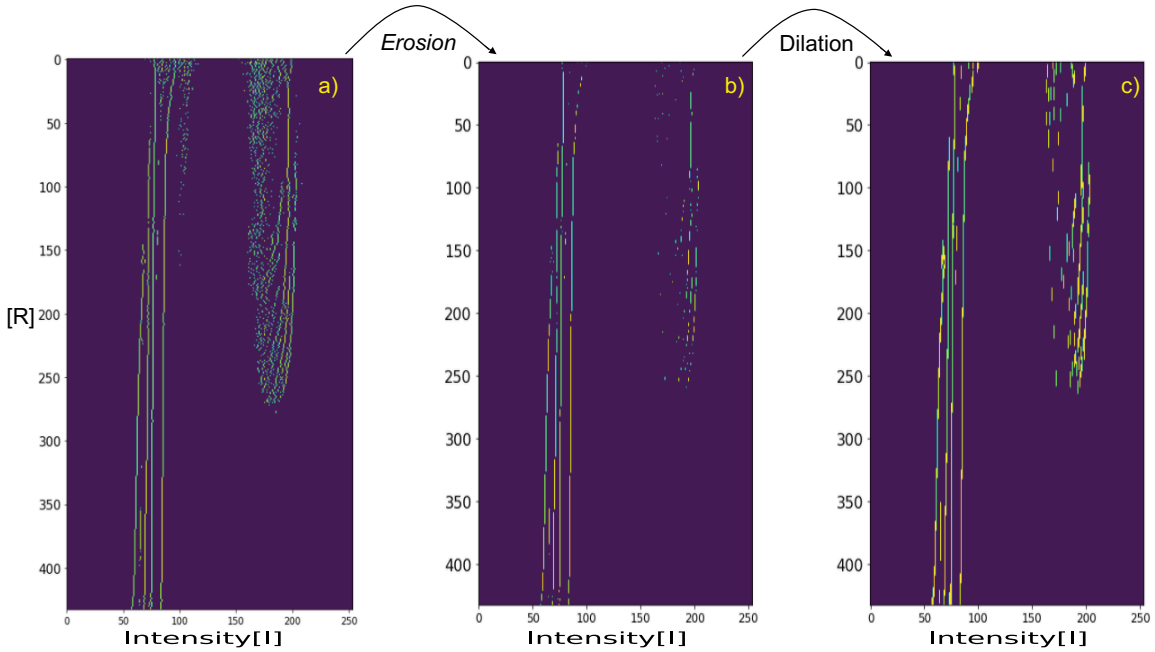

Figure 40: Figure a is the binary array where every ”dot” is a peak/mean for all distributions. Figure b is the array where peaks with no vertical neighbors are removed through erosion and in c are all the severed ties are reconnected with dilation forming connected clusters.

A labeling function from the library NDImage, called *label* was the applied on the array in Figure 40c. This takes connected clusters within the array labels each pixel in the same cluster with matching integer values. There after were clusters below a size threshold removed, leaving with the final labels in Figure 41.

As shown in Figure 41a, are 5 labels left, these labels represent the reference-frame for each class, so the labels are a class. The last step is separating distributions. All distributions in the python lists are compared layer-wise from top to bottom with the labels. So the distributions in the python list, are compared with the labeled array. Each label represents a class and distributions are assigned to the label that matches the mean of the distributions most. Finally all distributions are assigned to their respective labels and the result is shown in Figure 42.

The implant is long gone from the data processing, but for illustrative purposes was it included to show it works for all classes.

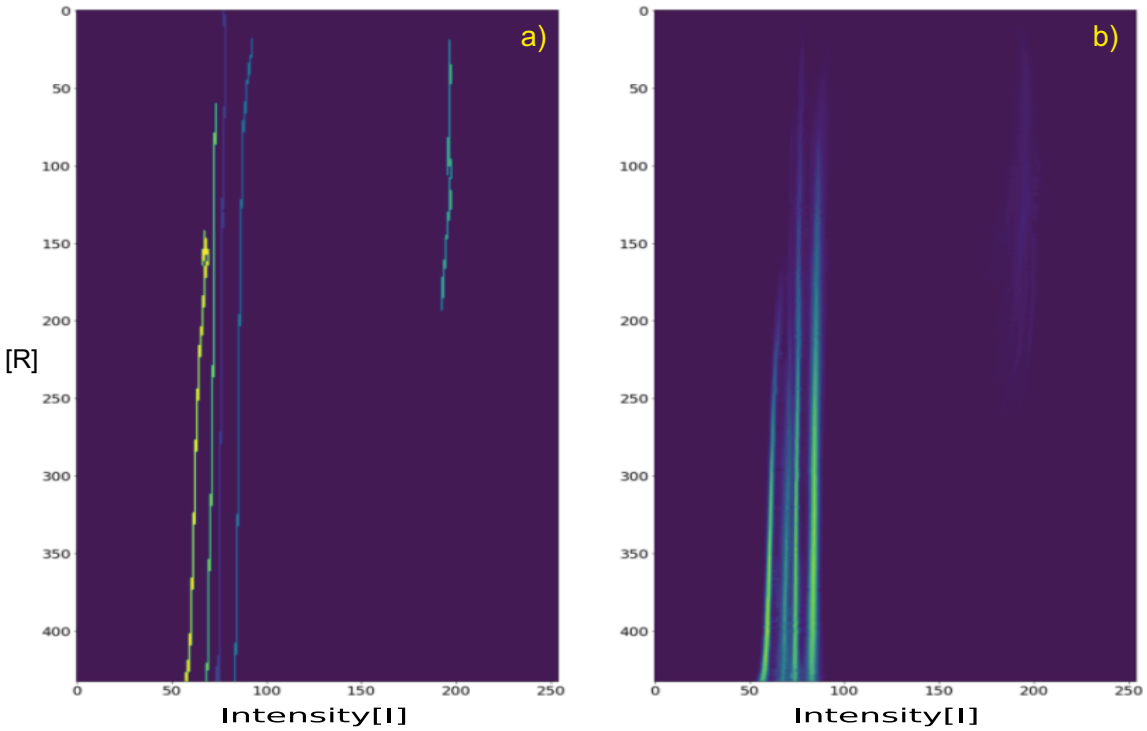

Figure 41: Figure a are the labels extracted from Figure 40c and to the right in Figure b are the fitted 2d-distributions to compare the two and visually see similarities.

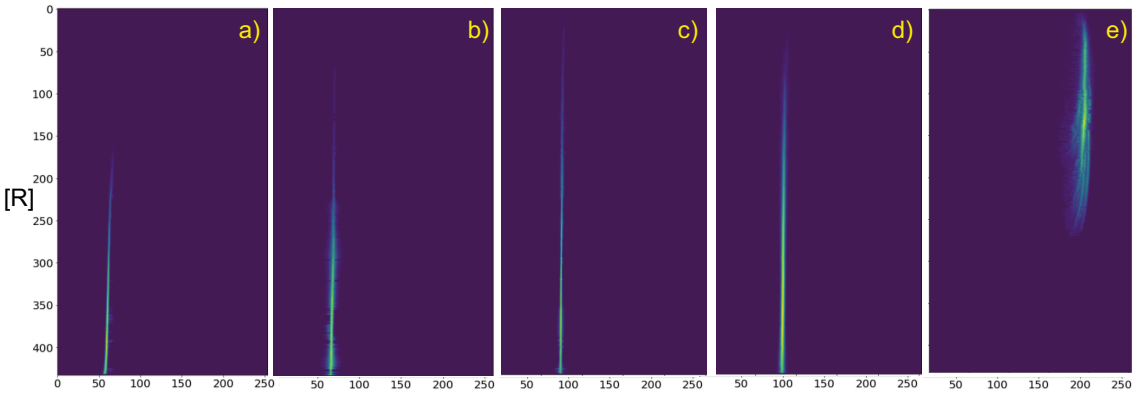

Figure 42: Figures a through e are all the distribution matched with the shown labels in Figure 41a. So a is the left most class and e is the right most distributed from Figure 41b.

At this point was everything in place to initiate the final segmentation. But before commencing, were all functions and pre-calculated masks and fitted distributions checked. Then a flaw emerged in the resin bit-mask.

5.20 REPLACING THE RESIN-MASK WITH BONE-MASK

Initially on the 2d-histograms, the resin mask seemed to be a great addition. When the masks were plotted to check the visuals, was something absurdly off. All of the top resin was segmented correctly, but the bit-mask would also classify almost all of the upper cavities inside the bone-matrix. Resulting in the cavity voxels were removed by the bit-mask. Which is undesirable since the cornerstone of this segmentation is to map the network of the internal components of the bone-matrix. Which becomes problematic if a relative big chunk of that is removed. The flawed bit-mask are shown in Figure 43 next to the unmasked sample.

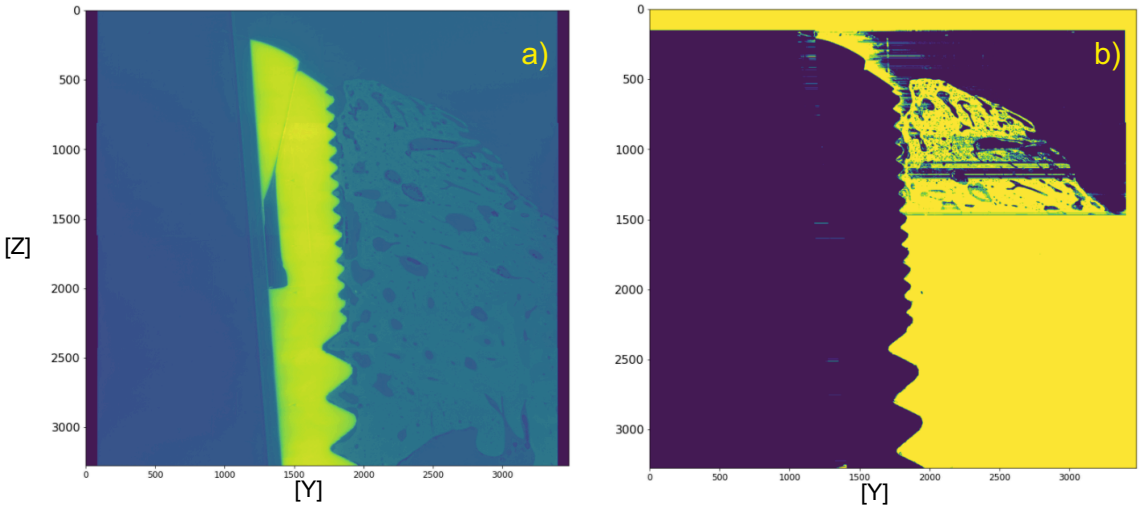

Figure 43: In Figure A, an unmasked X-slice of the sample and Figure B is the resin-mask, initially created to remove remaining futile data, as Fig b shows that it removes a bit chunk of cavity and void inside the bone, which is highly desired to remain and not be removed entirely

The final step for an effective segmentation was to create bone bit-mask. Until now had the focus been to remove everything around the bone, but why not just segment the bone separately and closed it like a sealed container. So everything outside the bone was excluded, while everything inside remained.

A bone segmentation was initiated in the Z-direction and for each layer segmented was a *convex_hull_image* function used from the NDImage library. It creates a custom polygon enveloping all information

within the image. An X-slice of both *convex_hull_image* and the segmented bone are illustrated Figure 44.

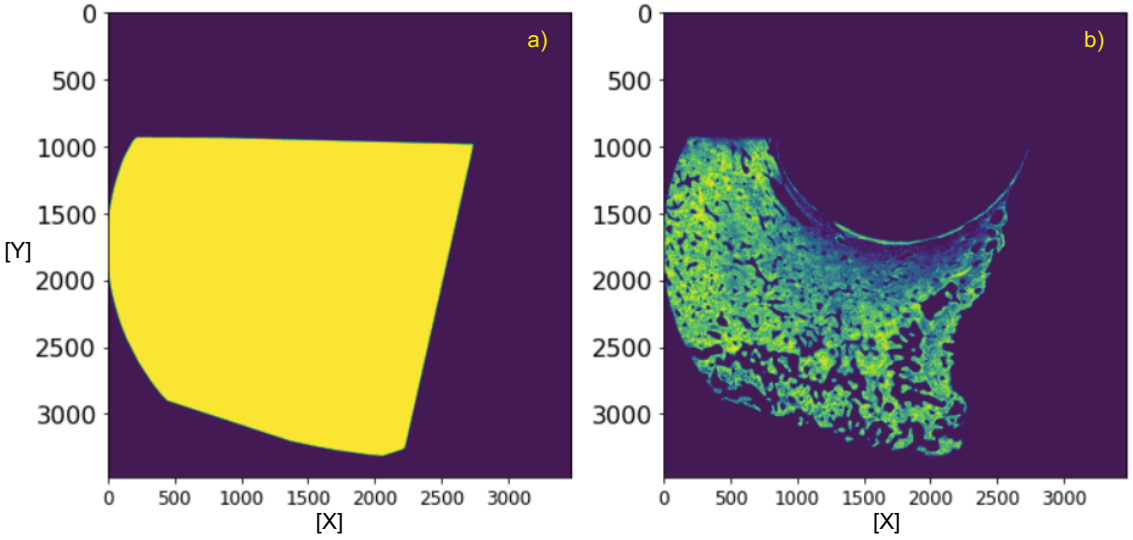

Figure 44: Fig a shows the result of the *Convex_Hull* algorithm applied on the segmented bone on the right in Fig b

Applying the convex hull to all layers of the bone segmentation, created a full size bone bit-mask. This new mask was combined with the improved implant bit-mask, resulting in the final bit-mask shown in Figure 45.

Now the final segmentation process are ready, to commence the processing of high resolution data i.e. the 1x data to find osteocytes. Four models(Radial, Z, Y and X) have been applied on the tomographies, yielding a segmentation with their respective strengths and weaknesses. The final move before the product is finished, is to combine the four different probabilistic models.

5.21 COMBINE THE FOUR MODELS INTO ONE

After a lot of filtering, fitting, segmentation and redesigning, did four different probability models stand concluded. Two classes remained from the initial five, illustrated in Figure 46.

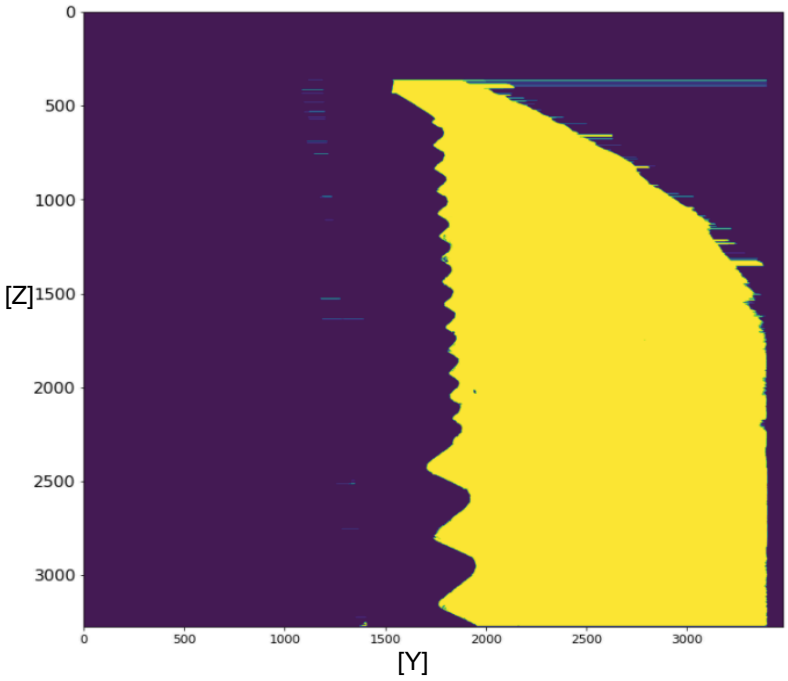

Figure 45: The final mask obtained by combining the upgrade implant mask from 36 and newly made bone mask

Each model yields two different tomographies. A tomography with high cavity probability voxels and another high bone-matrix probability voxels, the two classes left.

Bayesian inference were used to find the relative probabilities for all voxels in all methods (Rad,Z,Y,X), yielding the final expression for the probability for a voxel to belonging to a certain class be Eq. 14.

$$P(C=1|I(rad,z,y,x)) = \frac{\sum_i f_i(I(i)|C=1)}{\sum_i [f_i(I(i)|C=1) + f_i(I|C=0)]} \tag{14}$$

Eq. 14 shows the probability for a voxel being class 1 i.e. bone in this case.

Each model(f_i) is inputted to the function for a final result of the bone-model as shown in Figure 47 and the final cavity model in Figure 48 seen below.

With this combined model of the form $P(C|I,rad,Z,Y,X)$ is the final product, the methodology section arrives at the final stop.

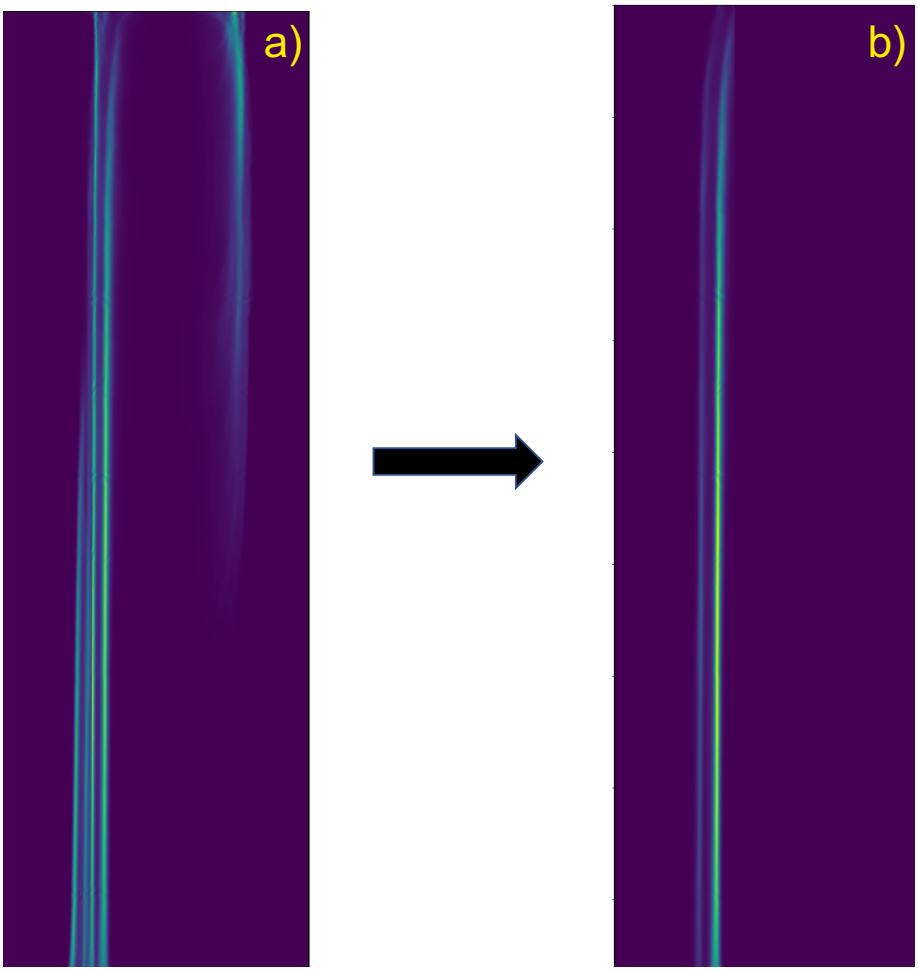

Figure 46: The transition from figure a to b are the testament to the multiple steps through categorizing the components of the CT's and carefully sorting out irrelevant information, leaving only bone and it's internal cavities

5.22 OVERVIEW OF THE FINAL MODEL

This section simply holds a flow chart, illustrating the processing of raw data in the to final result.

With the methodology finally being wrapped up, the interpretation of the final segmentation will unfold in the results and discussion section.

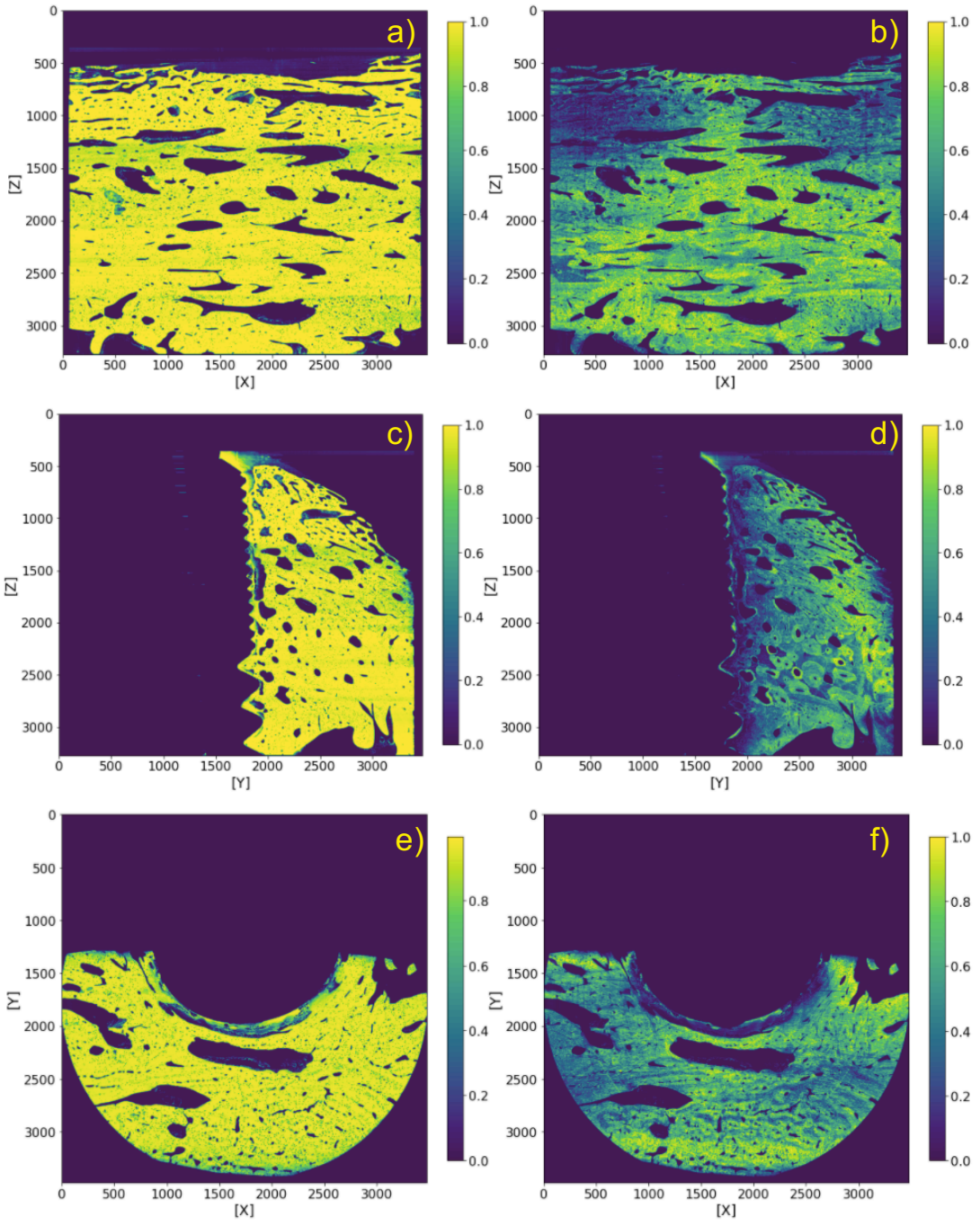

Figure 47: Results of the final bone segmentation. In the right column are the segmentation results of the Z-segmentation before using Bayesian inference(BI). While the column to the left are the results of using BI of the 4 methods. Each row represent a slice in each of the three dimensions Y, X and Z respectively

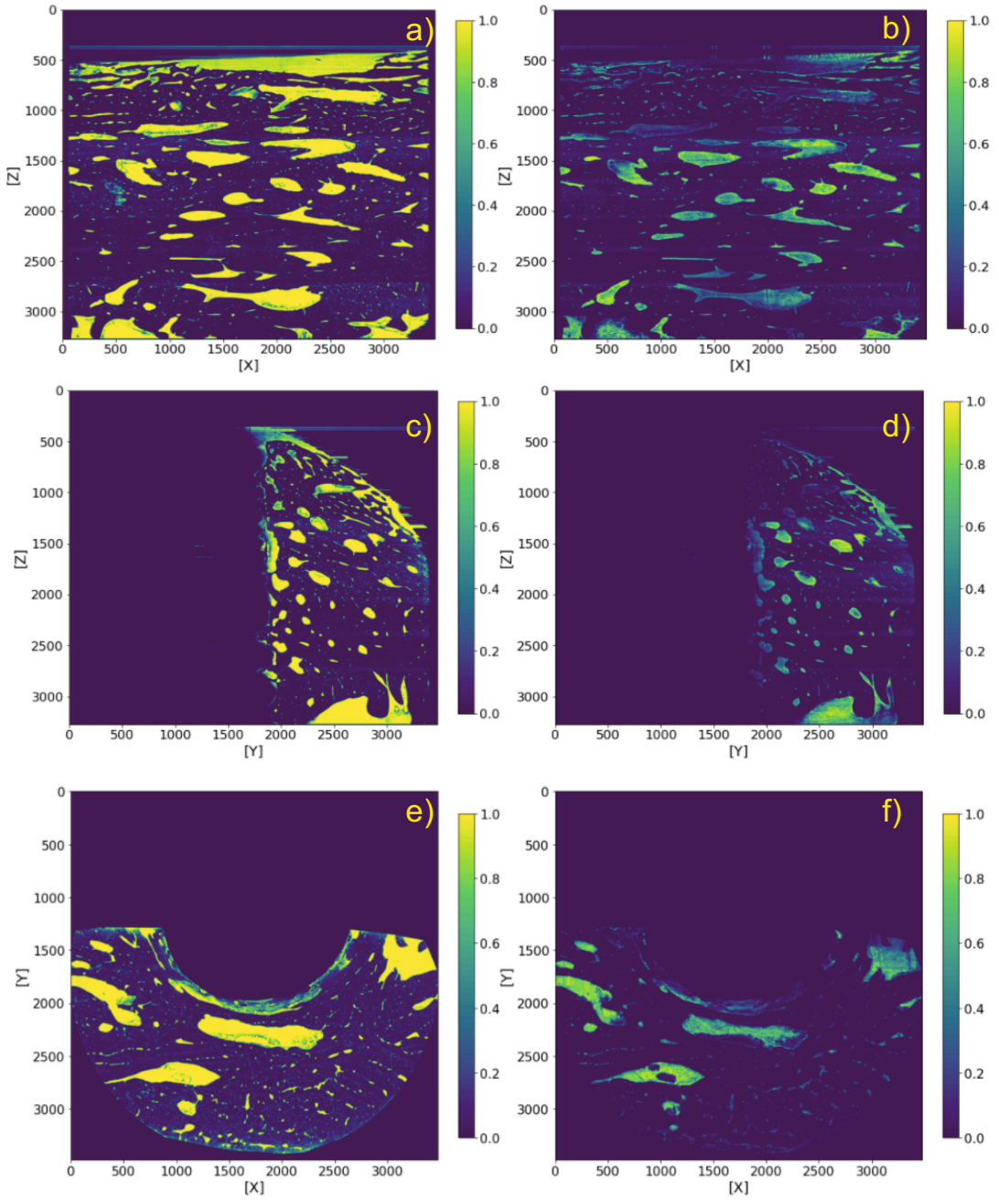

Figure 48: Exactly the same setup as in Figure 47 above, but for the second class, cavity

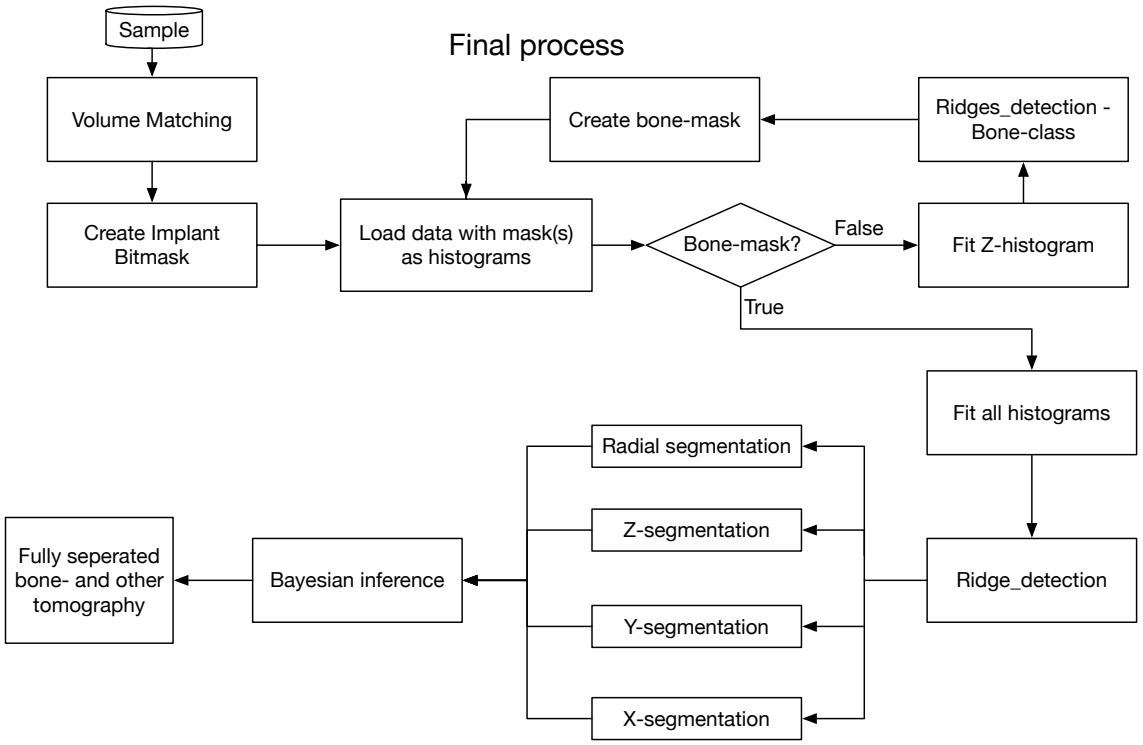

Figure 49: A flowchart of the final product of how the bone tomographies are processed from start to end, iterating through all the tools developed through this section.

Part IV

RESULTS

6

RESULTS AND DISCUSSION

The segmentation have build a framework for high precision estimation, even between interfaces of high contrast areas for the bone matrix on a microscopic level as well as the inner component and their dynamics. Due to scarcity in the time budget are the results limited. The temporary results in the methodology section will be further elaborated, reemphasizing the effects and phenomena encountered. The main idea will be to deduce the effect of beam hardening and how morphology affects cavity classification. Also how specific transitions in materials affect voxels intensities and how it might produce reflection and refraction along interfaces. The initial scope of the samples was to determine vertical growth of new bone-tissue along a support. 3d Illustration will test if the segmentation method favors a continues nature of the inner components blood vessels and perhaps osteocytic cells.

6.1 BEAM HARDENING EFFECTS

2d histogram have been converted into a simple scatter-plot making it easier to follow the progress. As expected from the radial 2d histogram, the intensities starts off very high, following the rapid decline until sloping off. The intensities continues to decrease while moving closer to the cylinders periphery. The bone class spans in the ranges $[\,100, 80]$ while cavity are $[90, 72]$. The reason could be, the closer

to the center thus closer to the thickest part of the the sample. Taking the attenuation of X-rays into account does it fall off exponentially w.r.t. to depth and material density, meaning only high energy photons within the spectre transmits all the way through the sample. Speaking strictly about how the detector measures intensities, are voxel intensities are inversely proportional to the number of photons registered by the sensor, the areas of high intensity are the areas with least transmission. Which could relate to higher voxels intensities for bone and cavity closer to the center.

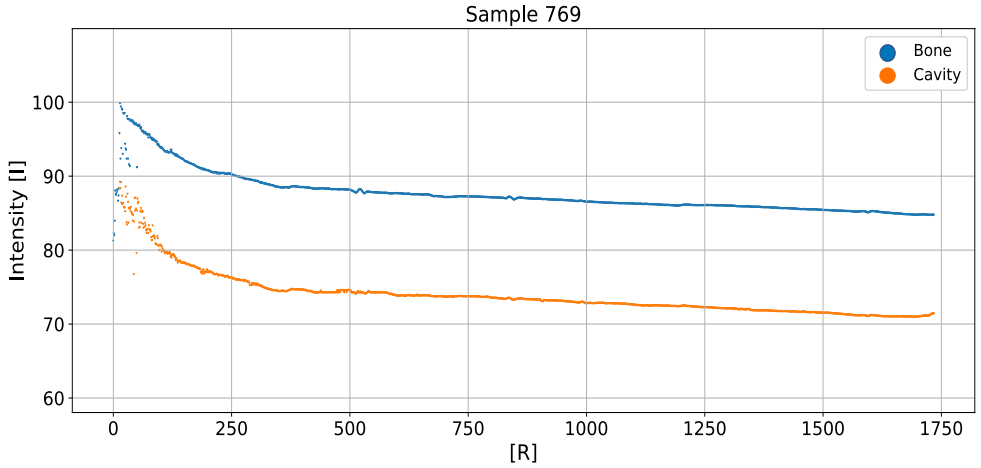

Figure 50: Beam hardening effect for sample 769. R is the distance to the center of the sample. The steady decrease implying an inverse relationship between sample thickness and intensity

Another effect could be the implant reflecting x-rays interacting with the surface causing bleaching of voxels in the nearest proximity as shown in Figure 51. The implant are a screw with very fine threading regions and course threading regions(as shown is Figure 43a), which could allow for more x-rays hitting the surface with inducing total external reflection in other directions. A mixture effect could be the cause for this leap in intensity.

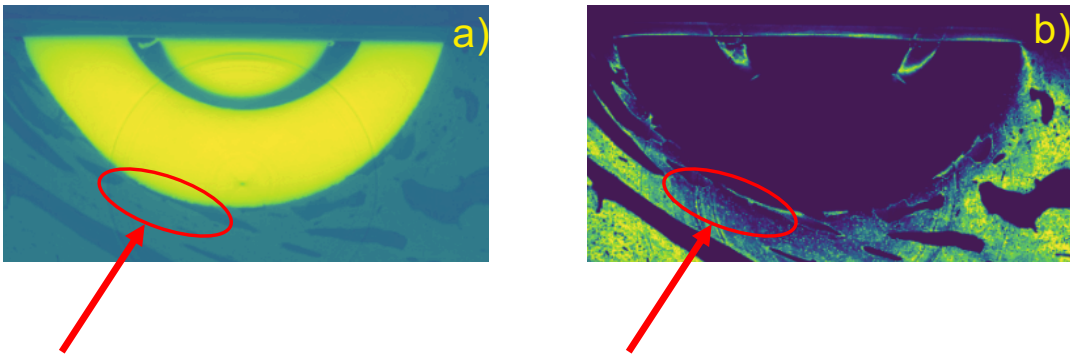

Figure 51: Figure 51a show bone close to the implant, while in Figure 51b are the bone almost completely gone.

Considering the radial histogram of the sample 770 it appears the only the bone voxels are affected by increased intensity. Further analysis reveal that some trace amount resin above the implant was removed improperly. This could tip the scale of the affected cavity voxels to a more constant intensity. These evidence point towards the implant causing the bleaching effects.

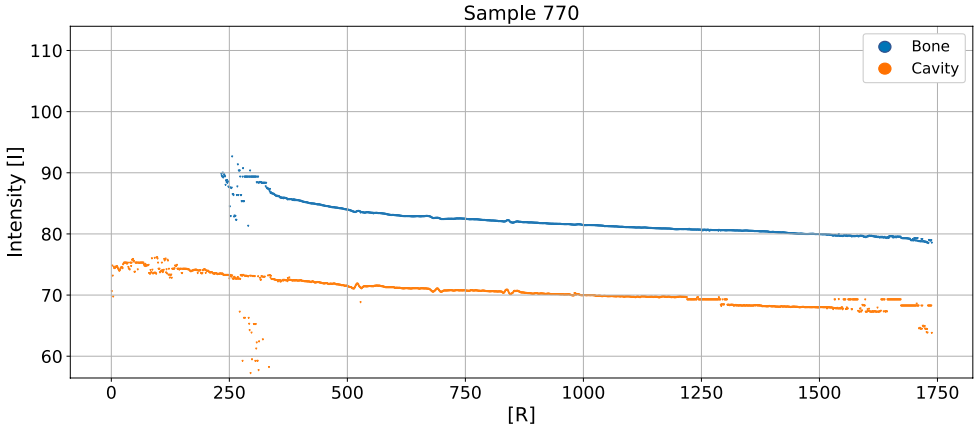

Figure 52: The cavity intensities are more discontinues compared to bone intensities. An affect that may originate from specific cavity geometries.

Across multiple plots of rad intensities does the cavity appear to oscillate slightly up and down in intensity. An effect, that could cause this is either the geometry of cavities, that imposes refraction. Causing the intensity fluctuate slightly. Or the bone-matrix are denser/thicker in that certain layer of the sample.

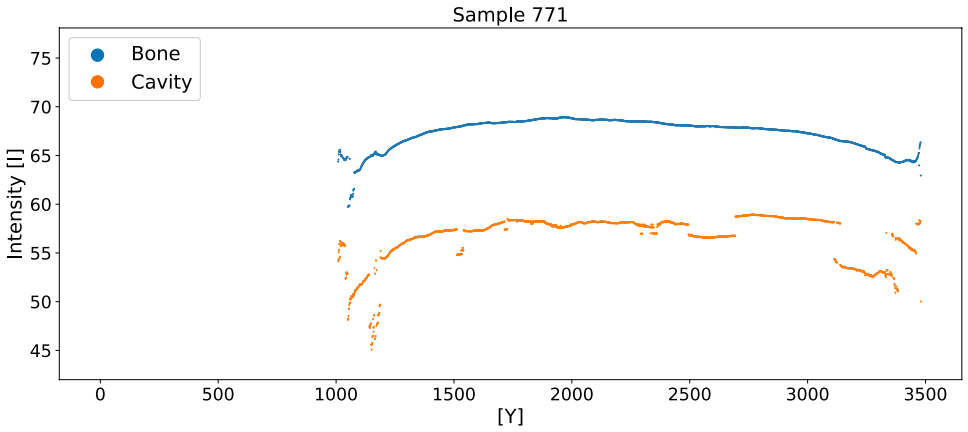

Figure 53: In Y-histogram of sample 771, can it be seen that the final values of matches that of Figure 52

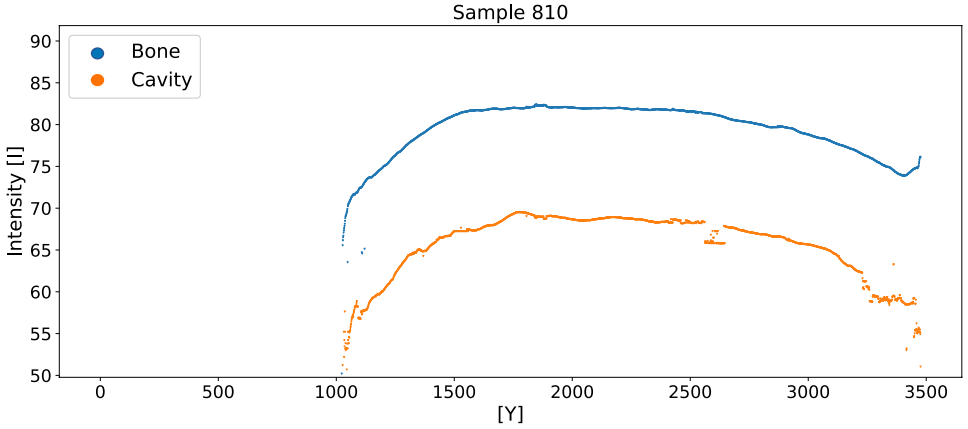

Figure 54: Initial large dip in intensity for Y-histogram. The reason for low intensity is that the bone-matrix in initial layers are situated on each end of the implant only leaving bone-matrix close to the periphery.

Features of the y-histograms are the very low intensities at the space where y overlaps with the implant. This could in turn be explained by few voxels in the y-plane are tuck up the implant compare the other data. So the low intensities in y are caused by only the outermost part of bone and cavity are included in these layers. Agreeing well with the radial close to the periphery. The y-histograms then rises and falls off again following an arc, once more we see matching radial intensities approaching sample edges.

Another feature is the spread of bone class expands wider and more regularly than cavity as shown in Figure 55. This can be argued as respective layers of bone may be calcified to different degrees,

greater varying density and material composition of local sub volumes, while the density air pocket are not sufficient to spread the signal. Spread in cavity class can be interpreted refraction effect of individual cavity curvature.

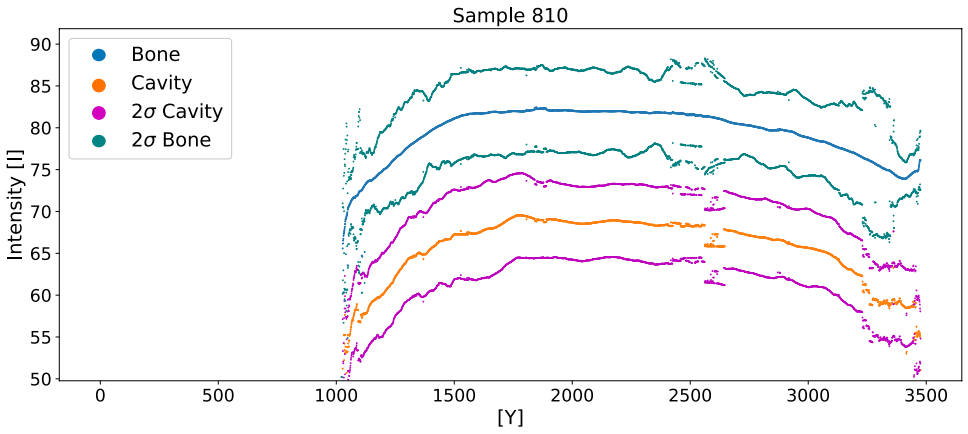

Figure 55: This figure illustrates how the width of bone distributions vary, while cavity spread appear more stable

The X and Z histograms were excluded due to the lack of significant change/leap in intensities. This finding reemphasizes the spatial information hidden in each dimension or lack there of. Incorporating the radial information, could correct the caused beam hardening.

6.2 BONE MASS DENSITY

Samples were initially made to track the vertical growth of bone-tissue around a bio-compatible implant. A common indicator of healthy bone are the relative bone mass density(BMD), which is measurement of the ratio of bone-matrix to remaining tissue. With the segmentation done, a layer-wise analysis can estimate the BMD ascending along the implant. An implant that has two sections. A coursed thread section, marking the old bone matrix and finer threading, indicating the mark where the implant was exposed when it was introduced into the bone.

Sample 770 in Figure 56 illustrates clearly how BMD has a steady decline the further up the implant. The X axis are the relative height difference from the base of the old bone matrix / thread transition of implant. Many samples showed similar features. Comparing the transition from old to newly grown bone, do most samples have similar BMD or even slightly higher. Up to 1mm vertical growth, following by decline.

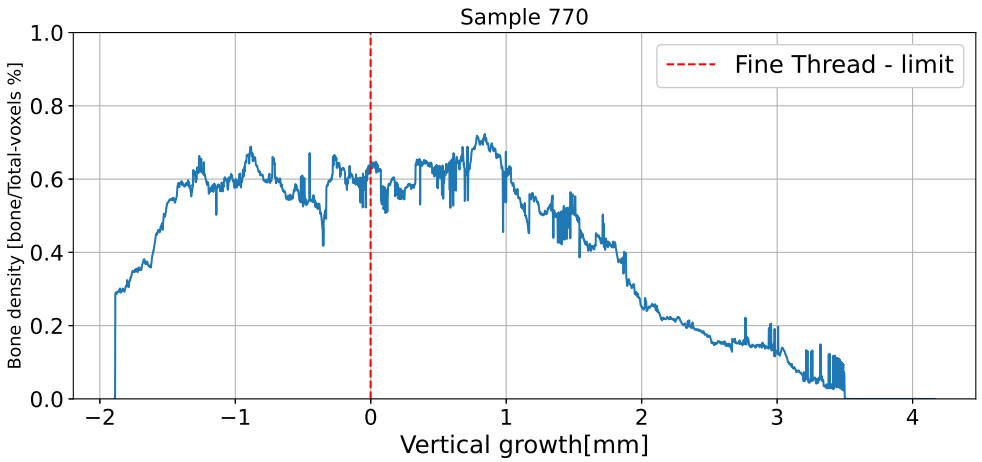

Figure 56: Thread line are the segment of the implant where the thread change from course to fine, i.e. the transition from old the new bone.

Same tendencies are visible for sample 810 in Figure 57, thus with more rapid fluctuations in density for separate layers.

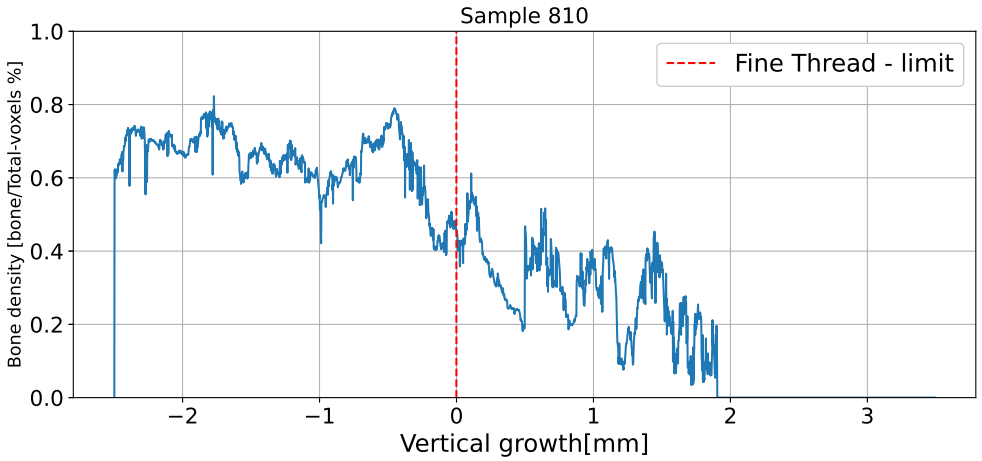

Figure 57: Bone Mass density fluctuates more rapidly above the thread limit compared to sample 770

All samples grew between 1.3 - 4.3mm with an average growth of 2.78mm pr. bone specimen. These growth spurs materialized over a 20 day period, which gives a daily growth pattern of $0.14mm$.

With a very fixed number of voxels assigned to different classes it becomes very simple to draw results by taking ratios. This only explains bone growth in a single direction. Estimating total growth pattern multiple directions are needed for a quality analysis.

6.3 3D VISUALIZATION

The ongoing segmentation was meant to build foundation for estimating the spatial components of the tomographies. Illustrating these spatial parameter is essential to uncover the true nature of tomography and if the segmentation was a success. A tomography of the 8x resolution data was passed through the segmentation separating the internal components from the bone. The lower resolution has been chosen because the entirety of tomography can be viewed and high resolution are not necessary, because the vessel are big enough to be traced in 8x data. Looking through the bottom of Figure58 gives a perspective of the depth and complex network of connected canals percolating through the sample.

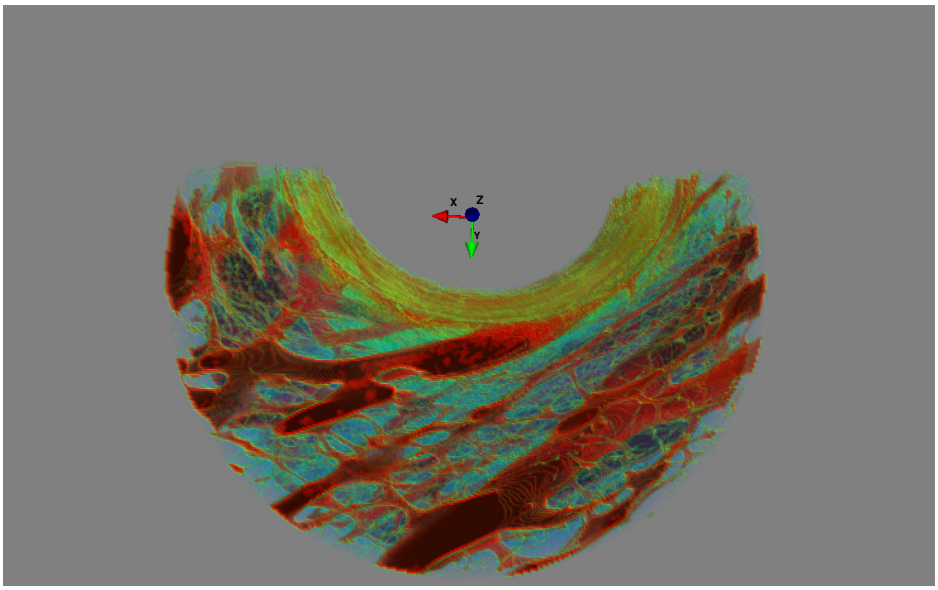

Figure 58: A view through the bottom of the a sample in the Z-direction

Projecting the same sample to view it from the side, it can be seen deeper in that thinner tubular shaped network. Given shaped and branching these are assumed to be capillaries. In the middle and the lower are dense in elongated capillaries, while in the far top are much more branching and shorter distances between vessels. This could be that the upper part are newer bone where newly formed vessels initially connects over short distance before the bone is fully mineralized and integrated.

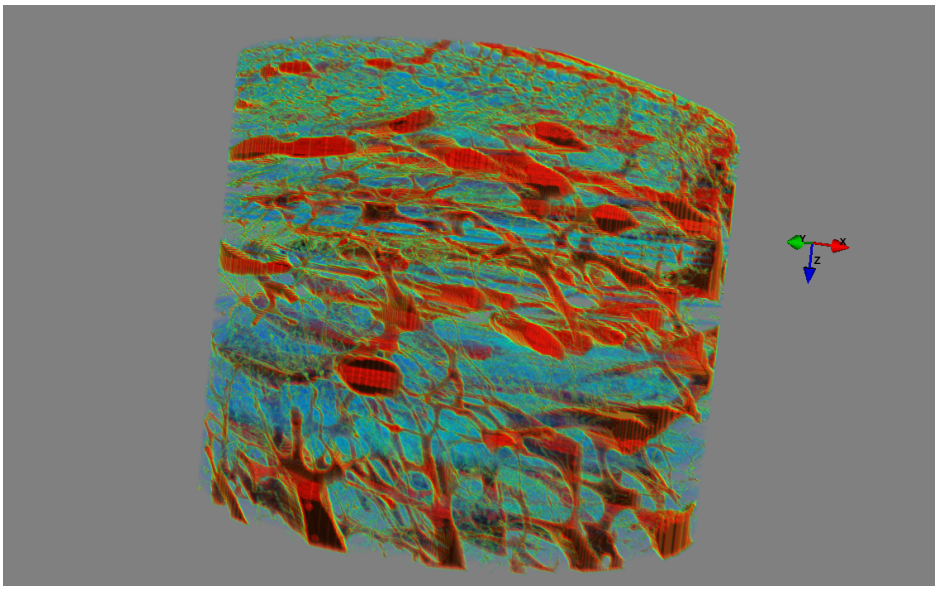

Figure 59: 3D visualization of the intricate inner network of the bone-matrix

The intricate network of interconnected vessel flow could provide a template for mathematically explain the creation of vessel flow through modelling in the smallest blood system within mammalian organisms.

6.4 OSTEOCYTES

A 100x200x200[Z,Y,X] voxel chunk from the high resolution segmentation was extracted from a segmented CT. The chunk was filtered by locating all clusters via labeling, then all clusters of 50-100 voxels in size were intensified too bring them in focus. The voxels resolution are $1.85\mu m$ which gives a voxels volume of $6.33\mu m^3$, scaling with 50-100 voxels gives size of $300 - 600\mu m^3$ and the common lacuna have an average size of $500\mu m^3$ and the tend to be clustered around vessels.

Applying the conditions to the chunk yield the illustration seen in Figure 60 and the red dots are the clusters which matched the condition hence the higher contrast. Given the concentric alignment with the tubular structures and size conditions are they osteocytes interconnecting to each other and the capillaries via their canaliculi, which too small to be seen here.

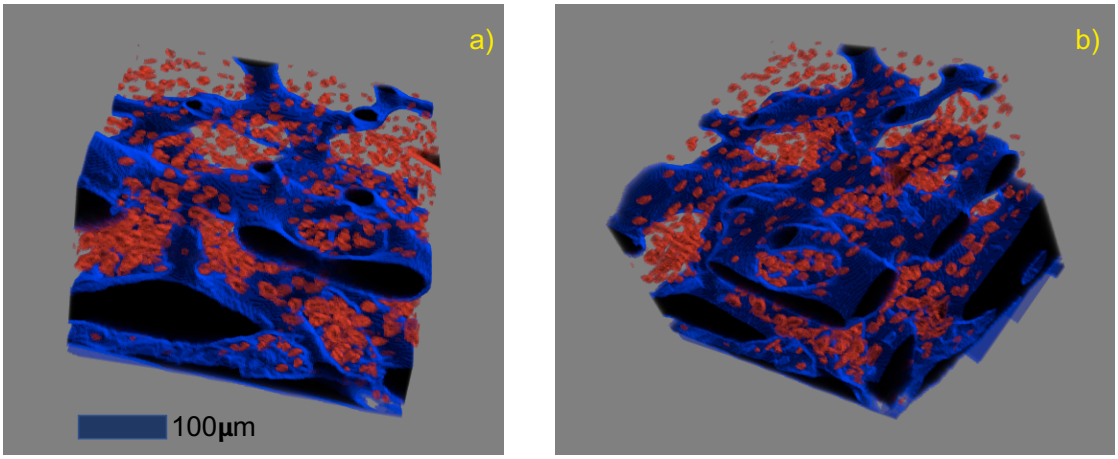

Figure 60: The dark blue areas resemble the capillary system. Red labeled lacunae situated around capillaries. Figure 60 a and b are two different angles of the same chunk, illustrating the depth of the segmented chunk

Scaling up to bigger chunks might unveil if the spatial nature and density of osteocytes may affect the dynamical system of bones. This could unveil what roles osteocytes might play in the growth of new bone tissue. But are left for future works

Part V

CONCLUSION AND FUTURE WORK

7

CONCLUSION

An automatic segmentation model was implemented with the use of matrix operations and spatially adapted probability distributions for separation of superficial- to useful data, enhancing individual components with high certainty. This removes all the issue with fixing data or preparing and allows to directly peer into the highly contrasted tomography.

These findings emphasize that $\mu - CT$ add key contributions for in depth analysis of bone derived system and could provide key information about the osteocytes involvement in growing completely new, rather than just remodeling it. May provide basis for a new paradigm for estimating bone quality with a ratio of bone-matrix/blood-tissue/osteocytes, rather just using the density of bone.

Radial segmentation could possible be integrated for beam hardening auto correction, focusing the signal allowing for a more unambiguous analysis of tomography intensities. By knowing the degree of beam hardening through the sample, could a mean value be chosen and then the remaining hardened voxels could be normalised w.r.t. that mean.

Micro-scale bone mass density estimation can register the slightest changes in bone modelling, which can be transitioned to an effective, high precision bone growth models. This could create a premise for tracking the bone growth with high precision and further developing into prediction the rate of bone growth given some factors.

Segmented high resolution $\mu - CT$ tomography unveil spatial and continues components of the internal bone structure, unlocking a perplexing world and could possibly expand the current knowledge

about the nature of bone-cells. Making is possible to survey the connectivity of the intricate network and assess if the degree of branching might bolster the healthy of bones.

8

FUTURE WORK

More questions remains, than asked. Following up the the segmented data it could be useful develop a mathematical model that could describing diffusive flow of the capillaries inside cortical structure of bone. A possible method could be to describe the flow of capillaries with a heat equation or a percolation matching the branching and diffusive flow through the bone-matrix.

As a supplement for the capillary flow, respective concentric cluster of osteocytes could be incorporated to correlate the creation of osteocytes and capillaries for bone modelling. Osteocyte shapes could be approximated as ellipsoids the check the orientation of osteocyte w.r.t. to the capillaries. A distance transform from the capillaries could provide the ratio of osteocytes concentric positioning around the capillaries

A more in quality based bone mass density estimation via a radiating distance transform from the implant base, creating a measure of bone mass density with respect to distance from implant. This could b e combined with the vertical growth to create 2d growth model.

A function for auto correcting voxels intensities with respect to beam hardening and uneven bone intensity via radial and Z-segmentation. Beam hardening could be corrected by choosing a point of the labeled class in the radial histogram and then normalise all other values with respect to the chosen value. The same could be done for the z axis.

Estimating the healthy bone tissue with a ratio of blood/Bone/osteocyte ratio. This could be done by gathering information of the approximated ratio and match the ratio to different areas in with in the

bone. Then combine all to get an overall estimation

At last optimizing the final segmentation further to improve fast computations with additional vectorizing of multiple integration functions. This could speed up the segmentation process by multiple magnitudes.

A broad range of different possibilities in assessing information about the microscopical world inside bones. In the long run could these combined efforts lay a foundation for a new revolution within medicinal imaging.

Part VI

APPENDICES

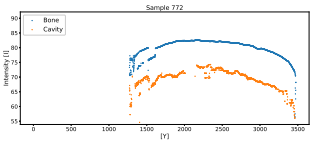

Figure 61: Appendix: Beam hard y - 772

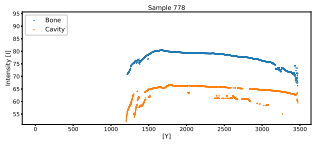

Figure 62: Appendix: Beam hard y - 778

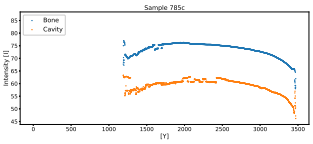

Figure 63: Appendix: Beam hard y - 772

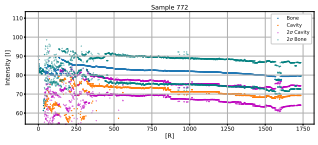

Figure 64: Appendix Beam hard

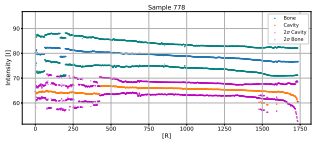

Figure 65: Appendix Beam hard

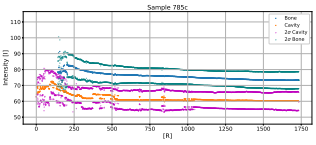

Figure 66: Appendix Beam hard

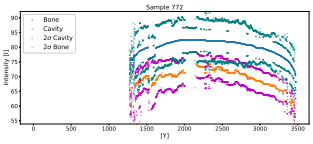

Figure 67: Appendix:Beam hard y sig 772

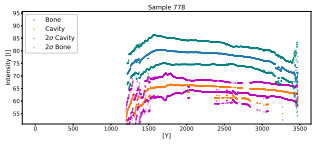

Figure 68: Appendix:Beam hard y sig 778

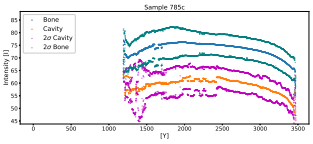

Figure 69: Appendix:Beam hard y sig 785c

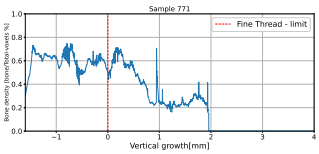

Figure 70: Appendix:BMD 771

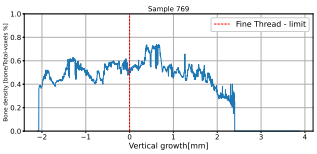

Figure 71: Appendix:BMD 769

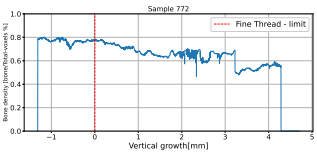

Figure 72: Appendix:BMD 772

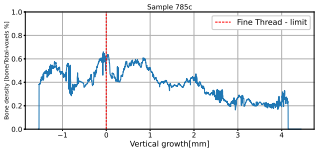

Figure 73: Appendix:BMD 785c

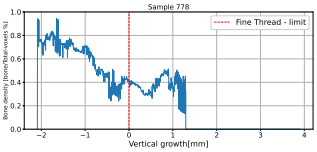

Figure 74: Appendix:BMD 778

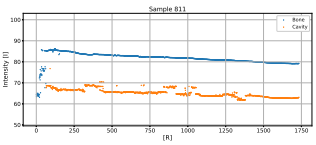

Figure 75: Appendix:BMD 811

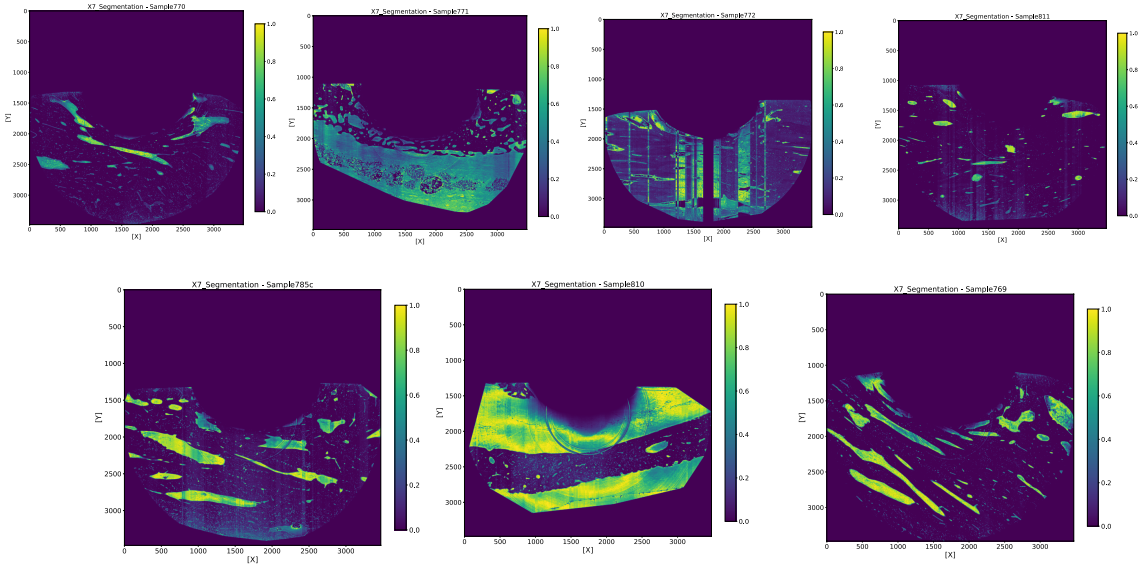

Figure 76: Appendix: Segmentation

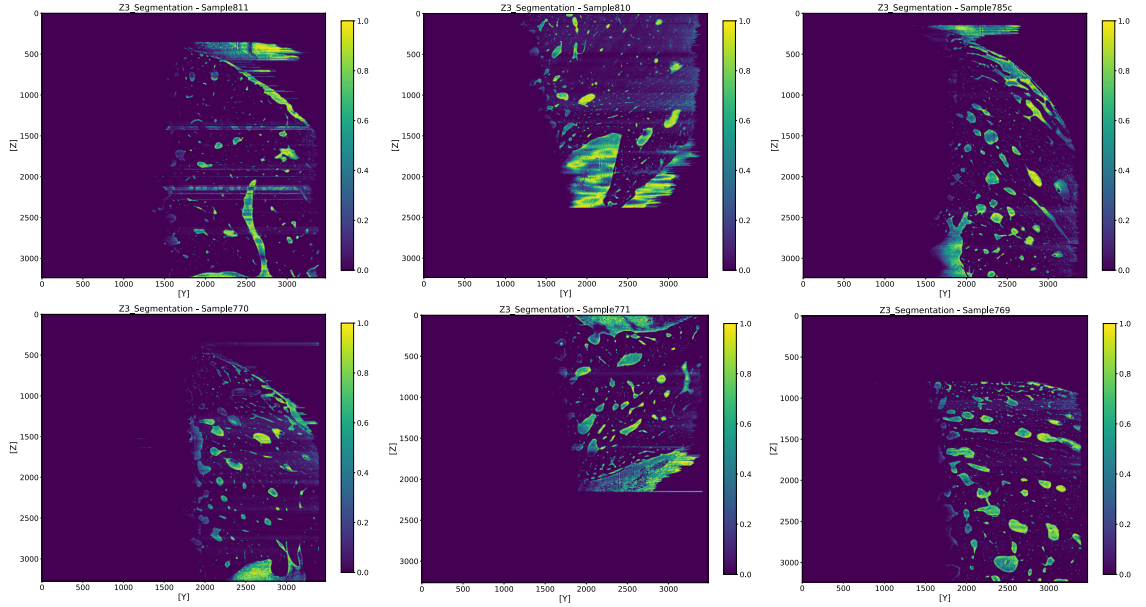

Figure 77: Appendix: Segmentation

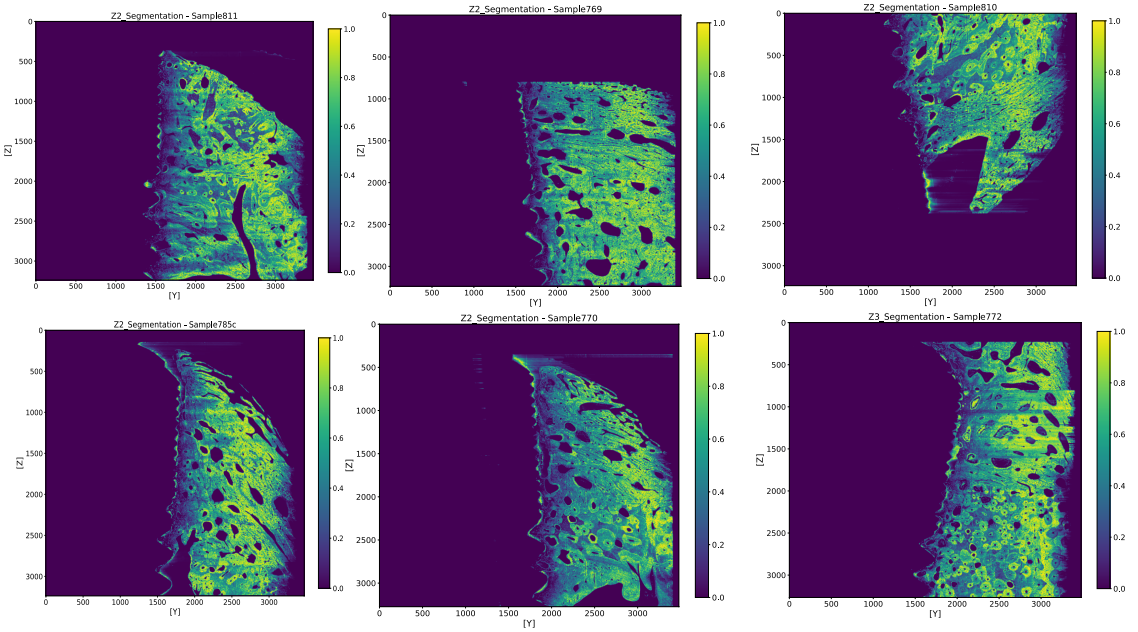

Figure 78: Appendix: Segmentation

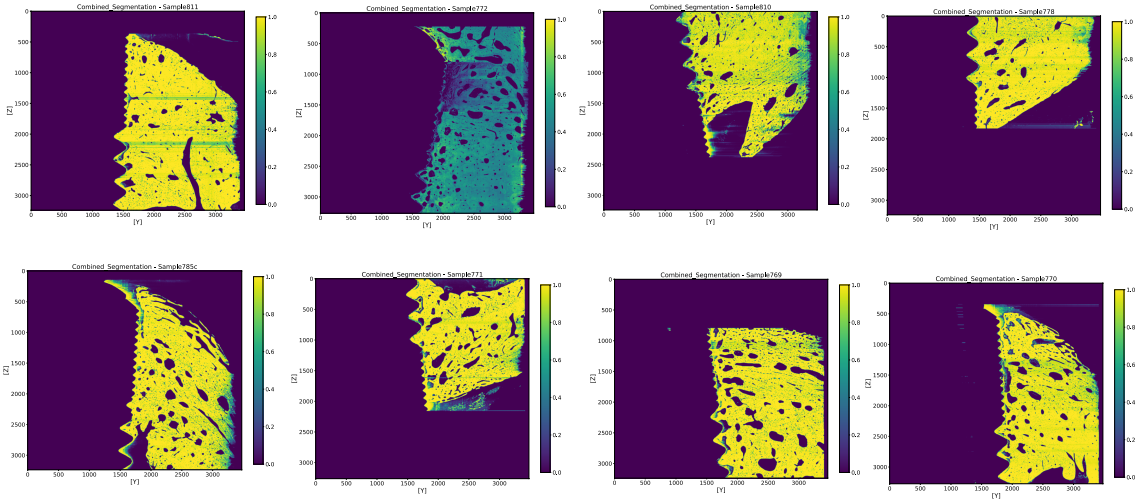

Figure 79: Appendix: Segmentation

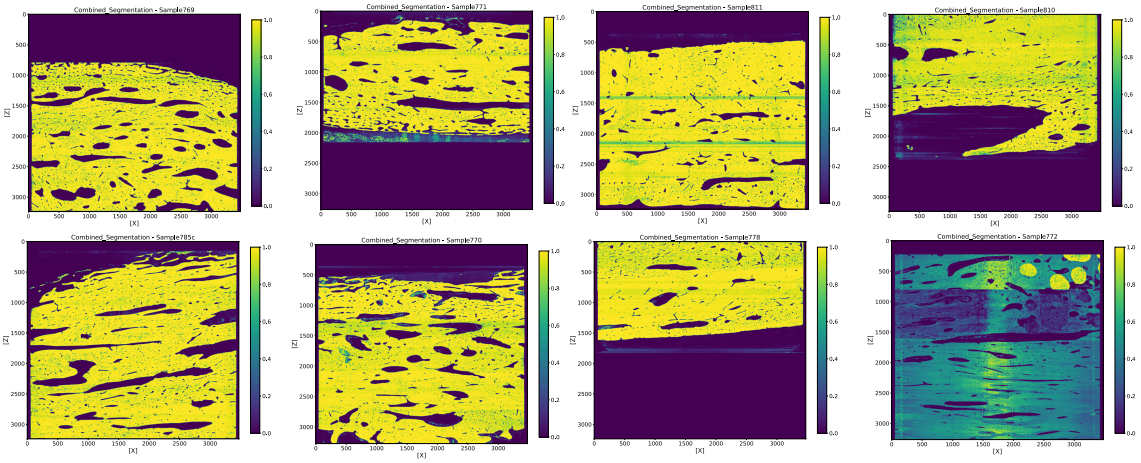

Figure 80: Appendix: Segmentation

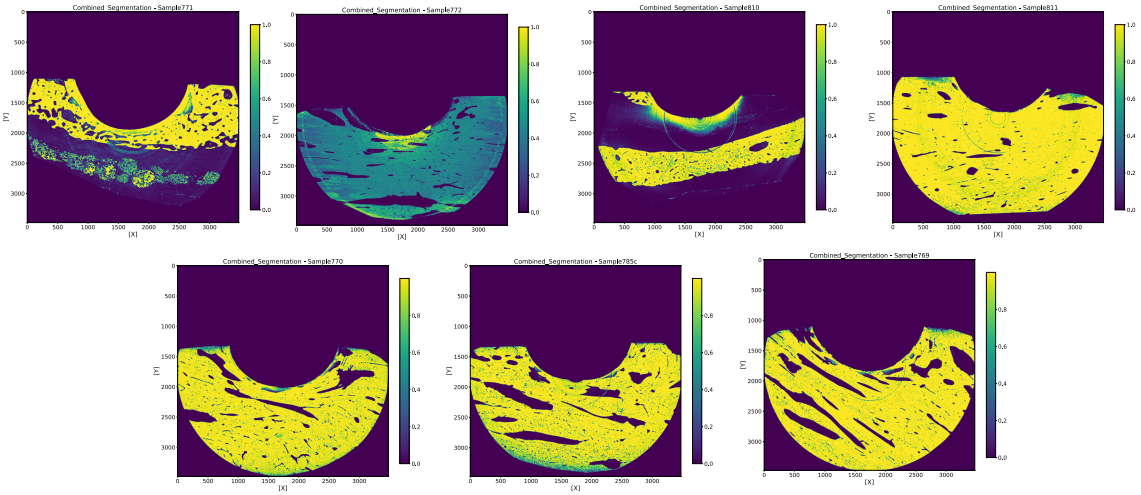

Figure 81: Appendix: Segmentation

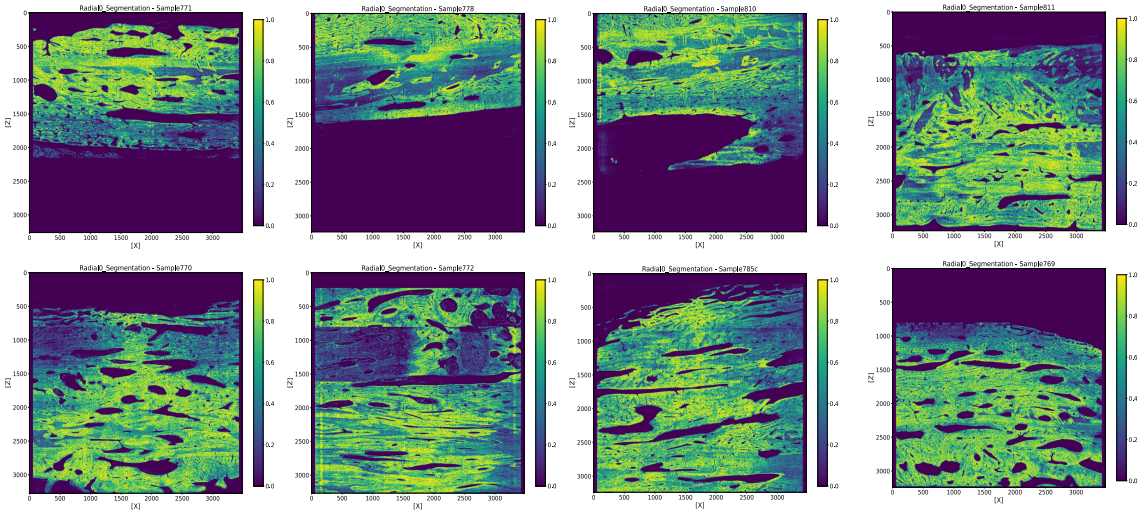

Figure 82: Appendix: Segmentation

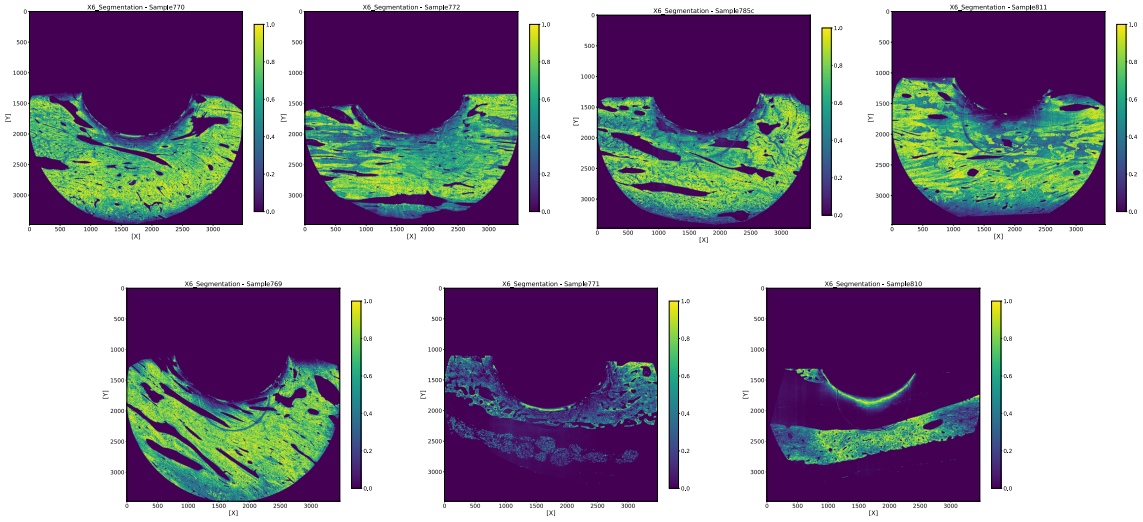

Figure 83: Appendix: Segmentation

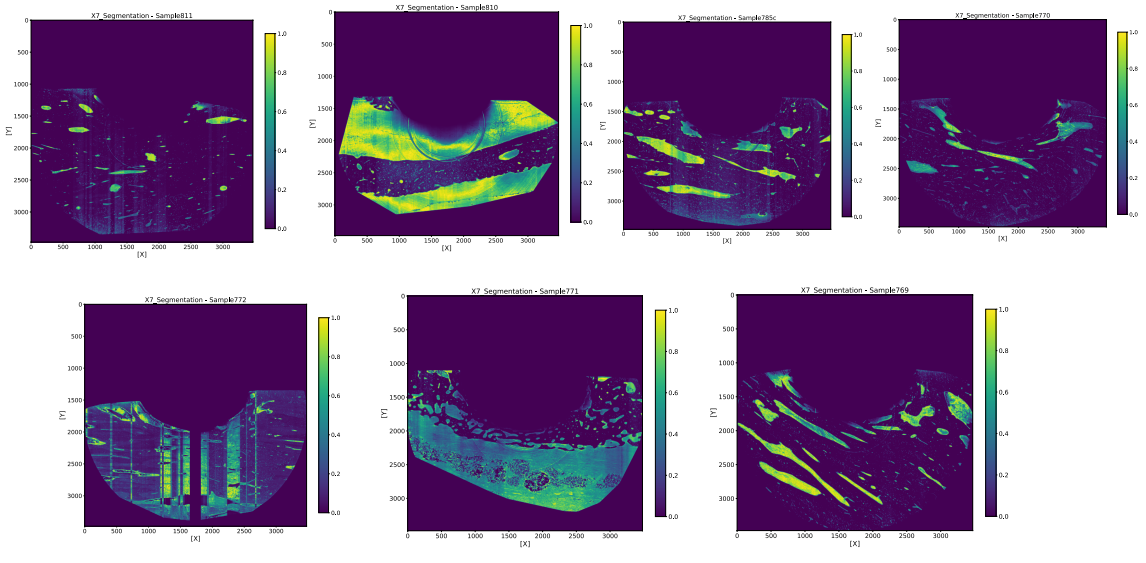

Figure 84: Appendix: Segmentation

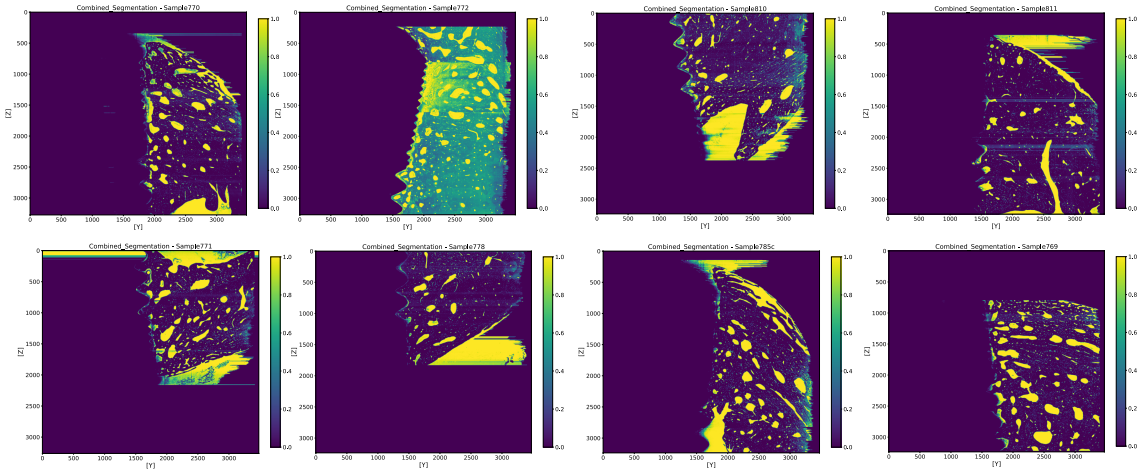

Figure 85: Appendix: Segmentation

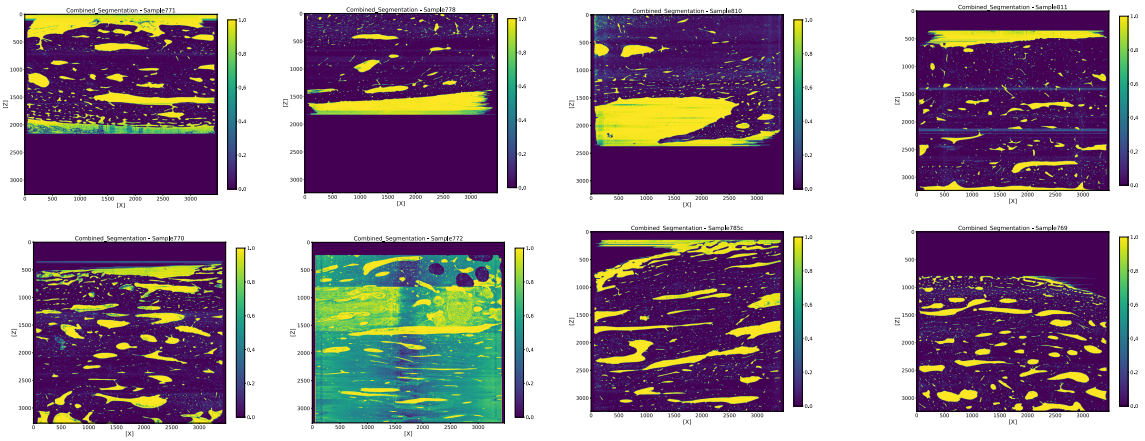

Figure 86: Appendix: Segmentation

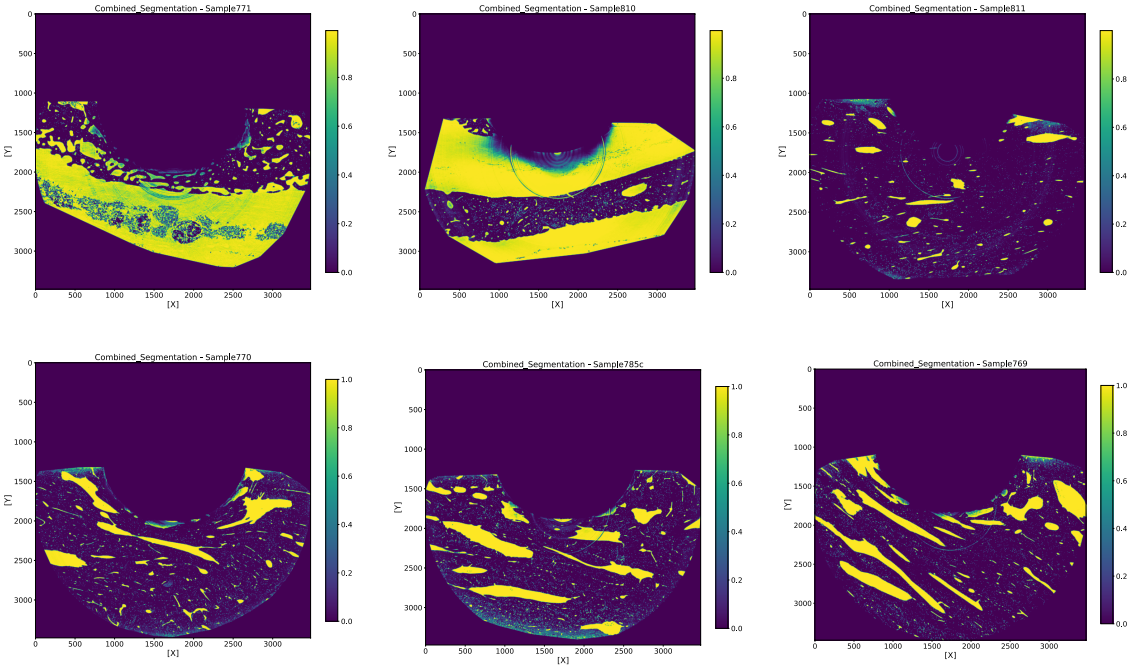

Figure 87: Appendix: Segmentation

BIBLIOGRAPHY

[1] Rafiou Agoro, Pu Ni, Megan L. Noonan, and Kenneth E. White. Osteocytic FGF23 and Its Kidney Function. *Frontiers in Endocrinology*, 11, aug 2020.

[2] Jens Als-Nielsen and Des McMorrow. *Elements of Modern X-ray Physics*. Wiley, mar 2011.

[3] Lengeler B. Coherence in X-ray physics. *Naturwissenschaften*, 88(6):249–260, jun 2001.

[4] Roger J Barlow. *Statistics: a guide to the use of statistical methods in the physical sciences*, volume 29. John Wiley & Sons, 1993.

[5] Olivier Bernard, Basma Touil, Jan D'hooge, and Denis Friboulet. Statistical Modeling of the Radio-Frequency Signal for Partially- and Fully-Developed Speckle Based on a Generalized Gaussian Model with Application to Echocardiography. *IEEE Transactions on Ultrasonics, Ferroelectrics, and Frequency Control*, 54(10):2189–2194, oct 2007.

[6] Lynda F Bonewald. Mechanosensation and transduction in osteocytes. *BoneKEy-Osteovision*, 3(10):7–15, oct 2006.

[7] Lynda F. Bonewald. The amazing osteocyte. *Journal of Bone and Mineral Research*, 2011.

[8] Britannica. white blood cell - https://www.britannica.com/science/white-blood-cell.

[9] Annemarie Brüel, Finn Christensen Erik Ilsøand Geneser, Klaus Qvortrup, and Jørgen Tranum-Jensen. *Genesers histologi*. Munksgaard, 2012.

[10] D. Chappard, M. F. Baslé, E. Legrand, and M. Audran. New laboratory tools in the assessment of bone quality. *Osteoporosis International*, 22(8):2225–2240, 2011.

[11] Daniel Chappard, Nadine Retailleau-Gaborit, Erick Legrand, Michel Félix Baslé, and Maurice Audran. Comparison Insight Bone Measurements by Histomorphometry and μCT. *Journal of Bone and Mineral Research*, 20(7):1177–1184, feb 2005.

[12] Sarah L. Dallas, Matthew Prideaux, and Lynda F. Bonewald. The osteocyte: An endocrine cell . . . and more, 2013.

[13] DoITPoMS. Structure of bone and implant materials https://www.doitpoms.ac.uk/tlplib/bones/formation.php.

[14] Alex Dytso, Ronit Bustin, H Vincent Poor, and Shlomo Shamai. Analytical properties of generalized Gaussian distributions. *Journal of Statistical Distributions and Applications*, 5(1):6, dec 2018.

[15] ESRF. What is synchrotron light? https://www.esrf.eu/cms/live/live/en/sites/www/home/education/what-is-the-esrf/what-is-synchrotron-light.html.

[16] GISAXS. Refractive index - http://gisaxs.com/index.php/Refractive_index.

[17] Health Encyclopedia. https://www.urmc.rochester.edu/encyclopedia/content.aspx?ContentID=34&ContentTypeID=
2015.

[18] Basicmedical Key. Structure and Function of the Musculoskeletal System — Basicmedical Key.

[19] J. Klein-Nulend and L. F. Bonewald. The osteocyte. In *Principles of Bone Biology*. 2019.

[20] J. Klein-Nulend and L. F. Bonewald. *The osteocyte*. Elsevier Inc., 2019.

[21] Wen Li, Joseph D. Gardinier, Christopher Price, and Liyun Wang. Does blood pressure enhance solute transport in the bone lacunar-canalicular system? *Bone*, 47(2):353–359, aug 2010.

[22] Barbara R. McCreadie, Scott J. Hollister, Mitchell B. Schaffler, and Steven A. Goldstein. Osteocyte lacuna size and shape in women with and without osteoporotic fracture. *Journal of Biomechanics*, 37(4):563–572, apr 2004.

[23] Peter W. Milonni and Joseph H. Eberly. *Laser Physics*. John Wiley & Sons, Inc., Hoboken, NJ, USA, mar 2010.

[24] Camilla Albeck Neldam, Jon Sporring, Alexander Rack, Torsten Lauridsen, Ellen Margrethe Hauge, Henrik L. Jørgensen, Niklas Rye Jørgensen, Robert Feidenhansl, and Else Marie Pinholt. Synchrotron radiation μCT and histology evaluation of bone-to-implant contact. *Journal of Cranio-Maxillofacial Surgery*, 45(9):1448–1457, 2017.

[25] OrthopaedicsOne. Describe the process of bone remodeling - https://www.orthopaedicsone.com/display/Clerkship/Describe+the+process+of+bone+remodeling.

[26] Susan M. Ott. Cortical or Trabecular Bone: What's the Difference? *American Journal of Nephrology*, 47(6):373–375, jul 2018.

[27] Hai Qing, Laleh Ardeshirpour, Paola Divieti Pajevic, Vladimir Dusevich, Katharina Jähn, Shigeaki Kato, John Wysolmerski, and Lynda F. Bonewald. Demonstration of osteocytic perilacunar/canalicular remodeling in mice during lactation. *Journal of Bone and Mineral Research*, 27(5):1018–1029, may 2012.

[28] Mara Riminucci, Michael T. Collins, Neal S. Fedarko, Natasha Cherman, Alessandro Corsi, Kenneth E. White, Steven Waguespack, Anurag Gupta, Tamara Hannon, Michael J. Econs, Paolo Bianco, and Pamela Gehron Robey. FGF-23 in fibrous dysplasia of bone and its relationship to renal phosphate wasting. *Journal of Clinical Investigation*, 112(5):683–692, sep 2003.

[29] W. C. RONTGEN. ON A NEW KIND OF RAYS. *Science*, 3(59):227–231, feb 1896.

[30] F Welkenhuyzen, K Kiekens, M Pierlet, and W Dewulf. Industrial computer tomography for dimensional metrology : Overview of influence factors and improvement strategies. *Optical Measurement Techniques for Structures & Systems*, (May 2014):401–410, 2010.